Engineering the Electrode-Electrolyte Interface:

From Electrode Architecture to Zn Redox in Ionic Liquid Electrolytes

by

Erika Engstrom

A Dissertation Presented in Partial Fulfillment
of the Requirements for the Degree
Doctor of Philosophy

Approved October 2011 by the
Graduate Supervisory Committee:

Cody Friesen, Chair
Daniel Buttry
Karl Sieradzki

ARIZONA STATE UNIVERSITY

December 2011

ABSTRACT

The electrode-electrolyte interface in electrochemical environments involves the understanding of complex processes relevant for all electrochemical applications. Some of these processes include electronic structure, charge storage, charge transfer, solvent dynamics and structure and surface adsorption. In order to engineer electrochemical systems, no matter the function, requires fundamental intuition of all the processes at the interface. The following work presents different systems in which the electrode-electrolyte interface is highly important. The first is a charge storage electrode utilizing percolation theory to develop an electrode architecture producing high capacities. This is followed by Zn deposition in an ionic liquid in which the deposition morphology is highly dependant on the charge transfer and surface adsorption at the interface.

Electrode Architecture: A three-dimensional manganese oxide supercapacitor electrode architecture is synthesized by leveraging percolation theory to develop a hierarchically designed tri-continuous percolated network. The three percolated phases include a faradaically-active material, electrically conductive material and pore-former templated void space. The micropores create pathways for ionic conductivity, while the nanoscale electrically conducting phase provides both bulk conductivity and local electron transfer with the electrochemically active phase.

Zn Electrodeposition: Zn redox in air and water stable N-ethyl-N-methylmorpholinium bis(trifluoromethanesulfonyl)imide, $[C_2nmm][NTf_2]$ is presented. Under various conditions, characterization of overpotential, kinetics and diffusion of Zn species and morphological evolution as a function of overpotential and Zn concentration are analyzed. The surface stress evolution during Zn deposition is examined where grain size and texturing play significant rolls in compressive stress generation. Morphological repeatability in the ILs led to a novel study of purity in ionic liquids where it is found that surface adsorption of residual amine and chloride from the organic synthesis affect growth characteristics.

The drivers of this work are to understand the processes occurring at the electrode-electrolyte interface and with that knowledge, engineer systems yielding optimal performance. With this in mind, the design of a bulk supercapacitor electrode architecture with excellent composite specific capacitances, as well as develop conditions producing ideal Zn deposition morphologies was completed.

DEDICATION

To Andy, Mom, Dad, Allison and Melanie for their comedy, love and support.

ACKNOWLEDGMENT

First I must thank Dr. Cody Friesen, my Ph.D advisor. An anecdote of our interaction portrays how positively his influence on my growth as a student and researcher has been. Students are required to take a qualifying exam consisting of an oral test of your knowledge of your field, however, if the student received a 3.5 GPA or higher, they could opt out of the exam. I was relieved that with a GPA above 3.5 I did not have to go through the daunting task of taking this exam. Dr. Friesen saw it another way and to my dismay, he was adamant that all of his students take this exam. So I took a month to study, practice speaking in front of hostile crowds and prepare for the worst, and at the end of the grueling process, I passed with flying colors. I actually enjoyed the 2 hour exam. Dr. Friesen's guidance on studying and the gamesmanship of the exam was spot on. I gained so much from this experience that I still use the valuable lessons learned on a consistent basis. Thank you, Dr. Friesen, for consistently pushing me out of my comfort zone where all the real learning and growing happens.

Thank you to my coadvisors Dr. Daniel Buttry and Dr. Karl Sieradzki. I have thoroughly enjoyed extensive conversations and advice on the path of my research. Their willingness to make time for me is greatly appreciated.

Thank you to all of those who contributed data and scientific conversations without which this story could not have been told with such interest. Allison Engstrom provided data, and editing for the manganese oxide work. Derek Wolfe was an invaluable resource for the purity work, generously volunteering a significant amount of time and effort towards both results

interpretation and manuscript editing. Also, Dan Mahlman provided NMR results and Elise Switzer contributed electrochemical data. I must also thank all of the people who took the time and effort to read and edit this manuscript.

It has been a true pleasure to have worked with Susan Baldi, our fabulous administrative assistant. We have all been so lucky to have her helping us and always being a bright light around the offices.

David Wright has been a consistent source of scientific support throughout my tenure at ASU. His experimental wealth of knowledge is unsurpassed. I enjoyed bringing an idea to him, and brainstorming how to make it work. He was always willing to bend over backwards to help me, and I hope I did enough to return the favor.

Thank you to Yolanda Murphy, our graduate advisor, for her cheery sensibility and willingness to do anything for her graduate students. She was amazing at shielding us from the red tape and bureaucracy that is the PhD program.

My collegues, friends and lab partners, especially Jordan Kennedy, Larry Mickelson, Thomas Heaton, Allison Engstrom and Christina Koeritz, for their constant support. They are amazing springboards for ideas, comfortable shoulders to cry on when experiments were going wrong and just amazing people to be around. I am lucky to have had the opportunity to work with you for so long, and hope to maintain lifelong friendships. Also to all of the friends that I have had the fortune to know throughout this process; I have adored all the fun we've had together.

My family has supported me so much through this process, and I honesty don't know what I would have done without them. I was fortunate to have worked with my sister Allison when she was here as an undergrad at ASU. I loved working with her. When she decided to go to Berkely for grad school, I was very excited, but also sad that I would be losing my awesome lab partner. It has great to be going through grad school at the same time and to be able to pass down lessons learned to her, and for her to teach me new things as well. I hope that some day our careers align and we can work together again. If I was ever feeling worn out from work, I would always look to my sister Melanie for inspiration. Her passion and drive for her work, whether it is conservation or teaching in her classroom, is incessant. I love being around her because her laugh is so infectious that you can't help but have a great time. I have to thank my parents for their unwavering support of my education. My mom is a rock. She is always the kick in the pants I need when I start to feel sorry for myself, and I credit her influence on the strength it took to keep up with grad school. My dad is the consummate optimist. His ability to put a positive spin on any situation is extraordinary, and I constantly try to emulate that. I love you guys.

Lastly, I want to express my love and gratitude to my boyfriend Andy. He has ridden the rollercoaster that is the Ph.D. program with me and supported me so fervently through the years. I am so lucky to be able to be spending my life with someone whose joie de vivre is a constant reminder to live in the moment. I am a better person for knowing him, and I will never be able to convey how truly grateful I am for that. Thank you and I love you.

TABLE OF CONTENTS

Page

CHAPTER Page

APPENDIX Page

LIST OF TABLES

LIST OF FIGURES

Figure Page

Figure Page

Figure Page

Figure Page

Figure Page

Figure Page

CHAPTER 1 INTRODUCTION

1.1 Background

In addition to the focus of this thesis, I have had the opportunity to work on a variety of different projects during my tenure, though not all were studied to completion appropriate enough for the dissertation. Therefore, I feel it prudent to list and very briefly discuss them:

1. Thin Film Combinatorial approach to hydrogen storage materials with direct real-time compositional monitoring. I vacuum deposited air sensitive thin films of Li, Na and B onto Au quart crystals where their behavior upon hydriding was analyzed via mass changes detected by quartz crystal microbalance, QCM. The samples were reacted in a small vacuum chamber that I designed which included a turbo pump (capable of 10^{-8} Torr base pressure), a hydrogen leak valve, an ion vacuum gauge, a thermocouple vacuum gauge, a QCM, a custom designed resistive heating unit and temperature controller.
2. Observations in the H-Pd{111} System via Stress and EQCM Measurements. A joint project with Thomas Heaton where we independently measured the effects of the adsorption and desorption of H in Pd via mass balance and surface stress techniques (Appendix B).
3. An unconventional method of ammonia production. This was an ambitious project where I was first introduced to non-aqueous electrochemistry.

4. Tri-Continuous Manganese Oxide Electrodes Demonstrating Ultra-High Capacity (Chapters 2-4).
5. An extension of the manganese oxide electrode architecture work, wherein percolation theory in the subpercolated regime was studied. The purpose was to design an insulating anode containing a homogeneously dispersed subpercolated amount of metal that would act as a dendrite suppressor when metal was plated through it. I developed a new technique to synthesize 0.5 -1 μm sized salt crystals (pore former) via a spray freeze / freeze drying method.
6. Electrochemistry in ionic liquids including Electrodeposition of Zn in ionic liquids with direct application to Zn-Air, and a study of IL purity (Chapters 5-10).

With such a variety of research projects, I have gained expertise in a variety of areas, which I feel has thoroughly prepared me to complete the following dissertation, and ultimately the Ph.D. process.

1.2 Chapter Layout

Chapter 2 outlines manganese oxide supercapacitors and provides motivation for the development of a percolated tri-continuous bulk electrode to achieve high capacities.

Chapter 3 provides details on the supercapacitor electrode processing and characterization by voltammetry, XRD and SEM.

Chapter 4 outlines the optimization parameters of the supercapacitor electrode, including cycling potential and the concentrations of electroactive Mn, conducting Ni and pore former are detailed with parallels to continuum percolation theory.

Chapter 5 gives a background, advantages and challenges of electrodeposition in ionic liquids (ILs), as well as an introduction to Zn deposition in aqueous-alkaline and IL systems with direct application to Zn-Air batteries. The IL used in the majority of the study is also introduced.

Chapter 6 details the origins of overpotential by analysis of the Zn redox in $[C_2nmm][NTf_2]$ where nucleation, diffusion and charge transfer overpotentials all play mixed rolls under various conditions. Experimentally determined values for exchange current density and diffusivity are also shown.

Chapter 7 introduces the morphology evolution as a function of overpotential and $Zn(NTf_2)_2$ concentration.

Chapter 8 examines the morphological effects of water addition under various conditions, and correlates the results with the kinetics and diffusion characteristics found in Chapter 6.

Chapter 9 provides analysis of Zn growth in high Zn / high water solutions by in-situ electrochemical surface stress experiments.

Chapter 10 provides an in-depth analysis of IL purity, including EA, NMR, chromatography and electrochemical methods, and correlates the findings to alkylation–anion exchange synthesis techniques.

Chapter 11 is a summary of the thesis work and a proposal of future work in $[C_4mpy][NTf_2]$.

CHAPTER 2 SUPERCAPACITORS AND PERCOLATION THEORY

2.01 Introduction

The following chapter gives background into electrochemical capacitors, specifically manganese oxide supercapacitors. The motivation for the following work is introduced, which is to design an easily processed tri-continuous bulk electrode utilizing percolation theory to achieve high capacities. Thorough background on the general principles of percolation theory is given, defining the percolation threshold, p_c. With that knowledge, continuum percolation theory is outlined, where a new parameter, $\phi_{c,}$ gives insight into the design of the electrode itself.

2.1 Manganese Oxide Supercapacitors

The ever increasing demand for higher performing electrical energy storage has generated the need for novel storage technologies. Electrochemical capacitors have gathered more attention over conventional energy-storage devices due to their increased power density over batteries and improved energy density as compared to traditional capacitors [1,2]. There are two types of electrochemical capacitors: electrical double layer capacitors and pseudocapacitors. The electrical double layer capacitor stores charge within the double layer at the electrode/electrolyte interface. This requires high surface area materials and electrodes in order to achieve relevant capacitances. In contrast to double layer capacitors, pseudocapacitors utilize faradaic redox reactions and ion intercalation,

in addition to the capacity provided by the double layer, which in total provides for significantly significantly larger capacities.

One particular material that has shown optimal pseudocapacitive performance up to 760 F/g and excellent reversibility is RuO_2 [3,4]; however, this material along with other metal oxides are either cost prohibitive or have toxic properties that prevent commercially viability. Other materials of interest are conductive polymers, however the highest attainable capacities are much smaller [4]. Consequently, the most economical and most attractive material due to its high pseudocapacitance and relative lack of toxicity is manganese oxide. The mechanism for pseudocapacitance in manganese oxide is not fully understood; however, the most accepted theory is that ion intercalation and deintercalation accompanies the surface faradaic redox reactions. Proton and/or cations such as Li^+ and Na^+ are incorporated into the MnO_2 birnessite structure [5-8]. Proton or cation intercalation occurs during discharge, or reduction of MnO_2 to Mn_2O_3, Mn_3O_4 and $Mn(OH)_2$, and conversely deintercalation of the positive charged ions occurs upon charging, or oxidation. The discharge reactions of MnO_2 to $Mn(OH)_2$ with proton or cation intercalation [9,10] are shown in Equations 2.1 and 2.1.

$$MnO_2 + XH^+ + Xe^- \rightarrow MnO_{2-X}(OH)_X \quad (2.1)$$

$$(MnO_2)_{surface} + M^+ + e^- \rightarrow (MnOO^-M^+)_{surface} \quad (2.2)$$

The theoretical specific capacitance for MnO_2 is 1370 F/g [7], though the highest values currently achieved range between 450 to 930 F/g in thin film systems [3,4]. Due to the poor conductivity of manganese oxides (10^{-5}-10^{-6} S/cm) [7], testing is primarily done on thin films to minimize the solid-state transport-related losses associated with proton insertion and electrical transport. Various thin film synthesis techniques produced well performing manganese oxide materials exhibiting reasonable manganese specific capacities such as electrochemical deposition ranging from 240-504 F/g [11-15], sol-gel synthesis ranging from 317-720 F/g [8,16,17] and electrochemical oxidation ranging from 225 to 700 F/g [18,19]. Although thin films exhibit the highest experimentally measured capacity, scaling up to a bulk supercapacitor system with thin film electrodes is not trivial. In recent work, some have tried to incorporate conductive materials into the electrode synthesis process such as carbon [20,21] or nickel foam [22,23] to introduce an electrically conductive pathway within the bulk of the material. A successful bulk composite was produced by embedding manganese oxide particles in a carbon framework producing 600 F/g normalized to the mass of the manganese oxide, and 200 F/g with respect to the mass of the composite [24].

The following investigation introduces an innovative technique for designing a bulk composite manganese oxide structure with excellent pseudocapacitive performance. Percolation theory is used to guide the composition and processing of an electrode architecture with a hierarchically designed tri-continuous percolated network. The three phases include the electroactive pseudocapacitive

MnO_2, electrically conductive Ni and a templated pore network. Careful electrode preparation, combined with guidance from percolation theory yielded a bulk porous system on both the micro- and nano-scale with fully percolated networks of the active, conducting, and pore components. The micropores create pathways for ionic conduction of the electrolyte, whereas the nanoscopic ligaments allow for ease of electron transfer and increased surface area for redox reactions to occur during operation. The following section will outline percolation theory concepts and its application to electrode design.

2.2 Percolation Theory

Percolation theory studies "the effects of varying, in a random system, the richness of interconnects present." –R. Zallen [25]. Percolation itself is a random process. A simple illustration is the case of 1-dimensional percolation (Figure 2.1), where an infinite linear chain with lattice sites at fixed distances is defined. Each site is randomly occupied with probability, p. As more sites become occupied, clusters of varying sizes are formed. A cluster denotes filled sites (shaded circles) that are bounded by unfilled sites (empty circles). The number of s-clusters per lattice site, n_s, is derived as $n_s=p^s(1-p)^2$. For values of $p<1$, the cluster number goes exponentially to zero if s goes to infinity, and there will be holes in the chain. When $p=1$, all of the sites in the chain are occupied, and one single cluster is formed. The chain is now continuous and has formed a percolating cluster, defined as the percolation threshold, p_c. For $p<p_c$, an infinite cluster spanning from one end of the system to the other does not exist, whereas

for $p>p_c$ (which is not possible for the 1D case since $p_c=1$) the infinite cluster exists and grows as p moves further from p_c [26].

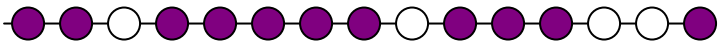

Figure 2.1: Schematic of clusters in a 1D lattice (site percolation). The shaded circles are the filled sites making up clusters of varying sizes, and the unshaded circles are empty sites (adapted from Stauffer [26]).

There are two types of percolation: site percolation and bond percolation. The aforementioned 1D percolation example is a site percolation process, where each bond is connected and it is the lattice sites that control the connectivity of the network. Bond percolation, on the other hand, takes each site to be occupied, and the bonds connecting the sites contribute to the percolation. A cluster in bond percolation is defined as a group of sites bounded by open bonds. The lattice coordination relates to bond percolation in that as coordination, z, decreases, the threshold for bond percolation, p_c^{bond}, increases. When the lattice sites are connected by fewer bonds, more bonds need to be added to gain connectivity. In the same way, the filling factor, v, is connected to the threshold for site percolation, p_c^{site}; as v decreases, p_c^{site} increases.

Table 2.1: Values for bond and site percolation on various lattice up to 3 dimensions. (RCP, random close packed) Table reproduced from data in Zallen pg. 170 [25].

Dimens-ionality	Lattice	p_c^{bond}	p_c^{site}	Coordi-nation, z	Filling Factor, ν	z p_c^{bond}	νp_c^{bond}
1	Chain	1	1	2	1	2	1
2	Triangular	0.347	0.5	6	0.907	2.08	0.45
2	Square	0.5	0.593	4	0.785	2.00	0.47
2	Honeycomb	0.45	0.698	4	0.680	1.80	0.44
3	FCC	0.119	0.198	12	0.7405	1.43	0.147
3	BCC	0.179	0.245	8	0.6802	1.43	0.167
3	SC	0.247	0.311	6	0.5236	1.45	0.163
3	Diamond	0.388	0.428	4	0.3401	1.55	1.146
3	RCP		[0.25][a]		0.637 [0.63][a]		[0.16][a]

For networks in more than one dimension, $p_c < 1$ and solving for n_s and other functions such as the percolation probability and average cluster size is dealt with generally with the use of scaling functions governed by critical exponents unique to each function. These exponents do not depend on the details of lattice geometry and are the same for the same dimensionality. They are also only truly valid near the percolation threshold, but provide at least some insight away from the threshold. This is not a trivial exercise and for all but the simplest systems,

requires numerical simulation to get precise functional dependencies on p, however the functions can be described in approximation as seen in Figure 2.2.

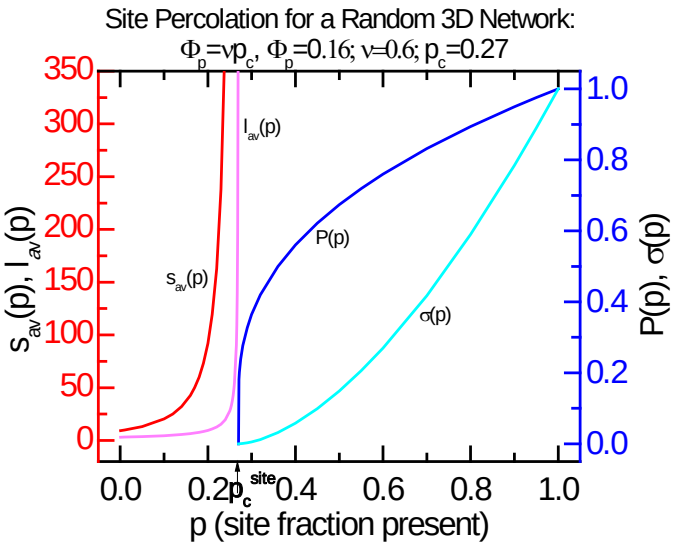

Figure 2.2: Modeled curves from the generalized functions for s_{av}, l_{av}, $P(p)$ and $\sigma(p)$ as a function of filled sites for site percolation on a 3-D continuum percolation model.

When $p<p_c$, s_{av}, the mean cluster size, and l_{av}, the mean spanning length, are functions that foreshadow the approaching percolation threshold. At $p=0$, $s_{av}=1$ and as p increases, s_{av} gets very large up to when $p=p_c$ at which point s_{av} becomes the infinite cluster and goes to infinity. While s_{av} denotes the volume of the cluster, l_{av} measures the cluster's linear behavior and gives insight into the cluster shape near the threshold. It can give a measure of the graininess of the system; far away from p_c it is very fine, and as p_c is approached it coarsens. This work, however, does not focus on what is happening below p_c. The main focus is

placed above the threshold, when all three of the phases would be continuous networks and would be fully percolated. When $p>p_c$, two functions, *P(p)*, the percolation probability, and *σ(p)*, the conductance, start at p_c and reach a maximum when *p* reaches *p=1*. *P(p)* is defined as the probability that *p*, the fraction of connected sites, is connected to the infinite cluster. Essentially, *P(p)* is a measure of volume growth of the extended connected network. Table 2.2 outlines the functions of interest and their exponents and Figure 2.2 illustrates these functions graphically. *P(p)* is zero when $p<p_c$, then rises very steeply close to p_c. When *P(p)* reaches a value of 1, it signals the consumption of all the finite

Table 2.2: Calculated values for the critical exponents in 2 and 3 dimensions for s_{av}, l_{av}, *P(p)* and *σ(p)*. Table partially reproduced from Zallen pg. 157 [25].

Function close to $p=p_c$	Exponent	Value of Exponent in	
		d=2	d=3
$P(p)\sim(p-p_c)^{\beta}$	β	0.14	0.4
$\sigma(p)\sim(p-p_c)^{t}$	t	1.1	1.65
$s_{av}(p)\sim(p_c-p)^{-\gamma}$	γ	2.4	1.7
$l_{av}(p)\sim(p_c-p)^{-\nu}$	ν	1.35	0.85

clusters into the single infinite cluster. The behavior of conductance near the threshold is very different than that of *P(p)*. Whereas *P(p)* sharply increases and has infinite slope, *σ(p)* has zero slope near p_c and has a slow rise. Near p_c, a finite cluster joining the already infinite cluster increases *P(p)*, but does not contribute to a new parallel path for conductance, and therefore does not cause large

increases in conductance. When the system is fully percolated ($p=1$) the value of conductance is at a maximum.

2.3 Continuum Percolation

Percolation in 1D,2D and 3D has been generally addressed in the previous sections for networks with well defined lattice structures. However, percolation in a random structure, which has direct application to the following work, without a defined lattice must be addressed separately. All the relevant information needed to discuss continuum percolation was addressed in the previous sections. Continuum percolation allows determination of p_c when the lattice is not well defined by the use of the critical volume fraction for site percolation, ϕ_c. Zallen presented a simple and convenient description of a random network, in order to relate ϕ and p^{site} [25]. Metal and glass spheres of equal size are placed into a vessel and evenly dispersed. Electrical connection via a metal sheet is placed below and above the spheres in order to create a circuit. We would like to predict the concentration of metal spheres where the system becomes electrically conductive by the formation of a spanning cluster from the bottom to top of the vessel. Or conversely, how many glass spheres are necessary to remove all conductivity from the system. Applying the appropriate terminology for continuum percolation, p^{site} defines the fraction of conducting metal spheres within a matrix of insulating glass spheres, and ϕ is the fraction of space taken up by the metal spheres. The relationship between the two is simply $\phi=vp^{site}$, where v is the filling factor for the random network, or the fraction of space occupied by the whole

system. The critical volume fraction is then, $\phi_c = v p_C^{site}$. For defined 2D and 3D lattices, p_c^{site} and p_c^{bond} vary from lattice to lattice [25]. ϕ_c, however, is independent of lattice structure and has been calculated to approximately 0.45 for all 2D lattices and 0.16 for all 3D lattices (Table 2.1). A system with random packing (RCP) has a filling factor close to 0.63, and using the $\phi_c = 0.16$ for 3 dimensions, p_c^{site} is calculated as 0.25. Therefore, percolation of a component occurs whenever the fraction of that material component exceeds 0.25. In the example described above, when the fraction of metal spheres is below 0.2, electricity will not flow through the insulating matrix; however, above 0.25 the structure is percolated thus completing the circuit and allowing electricity to flow [25]. Through the use of this tremendously powerful relationship it is predicted that if $p > 0.25$ for any given material, then it will be percolated. This simple formalism allows us to begin to hierarchically design the electrode structure and to allow us to hone in on the optimal concentrations of Mn, Ni and pore former particles. The manganese oxide active material is the insulating component (glass spheres) whereas the Ni is analogous to the conductive metal spheres [25].

It must be noted, that this continuum percolation model applies only to systems containing spheres of uniform size and shape [25,26]. Therefore, the formalism outlined above is not accurate in predicting the critical percolation threshold for the pore former which is two orders of magnitude larger than the Mn and Ni nanopowders. Others have addressed particles of different shapes [27,28] and size distributions [29] in percolation theory along with some experimental results

showing size dependence [30]. For example, a random system containing elliptically shaped particles having a well defined aspect is considered. The concentration of elliptical particles needed to reach the percolation threshold decreases with an increase in aspect ratio [28]. In other words, the more "needle-like" or the longer and thinner the elliptical particles are, the smaller the volumetric concentration required to reach a continuous spanning cluster. An example more applicable to the system tested in this study is that of varying size distribution. Take two separate systems, one with particles of size *R* and the other with particles of size *r*, where $R > r$, that are randomly mixed. The percolation threshold for the system containing *R* particles is higher than the system containing *r* particles. This is due to less disordering within the system, and consequently less branching of the particles hindering production of a continuous spanning cluster [29]. With this information, the percolation threshold of the larger pore former particles is greater than for the smaller particle Mn and Ni components, $p_{c,pore\ former}^{site} > p_{c,Mn,Ni}^{site}$.

CHAPTER 3 ELECTRODE DESIGN

3.01 Introduction

The following chapter provides a full description of electrode processing. Manganese and nickel nanopowders, and a variety of micron sized polystyrene powders were mixed, sintered and electrochemically oxidized forming the bulk supercapacitor electrode. Physical characterization by SEM showed the intimate contact between the Mn and Ni and the continuous pore network before and after electrochemical oxidation. XRD spectra revealed the highly defected structure of the oxidized manganese and cyclic voltammetry at varied scan rates showed the expected capacitive response.

3.1 Experimental

3.1.1 Composite Powder Preparation

The composite electrodes were synthesized via a powder processing method. The powders used were 20-50 nm Mn, 5-20 nm Ni (QuantumSphere), polystyrene microspheres of various sizes (Duke/Thermo Scientific), and polyethelene glycol used as a binder. Using various volume ratios, the powders were mixed in isopropanol via a 500 W, 20 kHz high power ultrasonic wand in order to achieve a homogeneous distribution. The ultrasonication was pulsed 10 s on, 10 s off for a total of 5 minutes. Immediately after ultrasonication, the mixture was dried in a drying oven 60 °C, then ground with a mortar and pestal to break up the dried power. It must be noted that while the composite powder synthesis process seems simple, it is also the most sensitive. The process must be carefully controlled in

order to remove any possibility of particle agglomeration that compromise consistency with a randomly packed network. Clustering of the nanopowders can cause deleterious effects on the achieved capacity by reducing contact between the three phases. The mixture was then weighed and pressed into a 0.25 in. diameter dye. The pellet was then heated at a ramp rate of 150 °C/hr in 5% H_2/Ar balance to a maximum temperature of 450 °C for an hour, then set to cool to room temperature at no defined rate. The hydrogen provides a reducing environment that removes the polystyrene spheres through pyrolysis leaving micron-sized spherical voids in the composite, which is seen clearly in upcoming figures. In order to clarify the optimization of the three constituents as it relates to percolation theory, the Ni and Mn concentration are reported as volume fractions with respect to the total powder volume. These fractions do not include the void space left behind by the pore-former or the space between the particles. The polystyrene or void concentration is reported as the volume fraction with respect to the total volume occupied by the powders as well as the pore-former.

3.1.2 Manganese Oxide Electrochemical Oxidation

All electrochemical experiments were completed with a Gamry G750 potentiostat. Electrochemical oxidation of the Mn metal to the electroactive MnO_2 (recognizing that the electrochemical redox facility in the material likely arises from the high ionic defect density in the electrochemically formed MnO_2) was completed using a potentiostatic method and is described below. Contrary to common technique, the oxidation occurs after the composite structure is

synthesized and while in direct contact with the current collecting medium (Ni powder). Electrical contact was made by fixing two fine mesh stainless steel screens on either face of the electrode with a Ni wire wrapped for support. A high surface area Pt/Ir coiled counter electrode and a Hg/HgO (+98 mV vs. SHE) reference electrode (Koslow Scientific) were used in a three electrode cell. Oxidation took place in 1 M LiOH electrolyte at a pH=14 prepared with 18 MΩ deionized water. According to the Mn Pourbaix diagram, at a pH of 14, Mn has four stable oxides ($Mn(OH)_2$, Mn_3O_4, Mn_2O_3, MnO_2). In order to oxidize the electrode into the MnO_2 region, the potential was held at 0.15 V vs. Hg/HgO for at least 24 hours until the oxidation reached a limiting current less than 10 μA.

3.1.3 Electrode Characterization

The pseudocapacitive performance of the electrode was electrochemically characterized by cyclic voltammetry at varying scan rates and by chronoamperometric charging and discharging cycles. The potentiostatic charge/discharge cycling was the primary technique for calculating the composite and Mn specific capacitance and the capacitive behavior was analyzed from the cyclic voltammetry curves. The electrodes were further characterized by x-ray-diffraction (XRD) using a Philips X'pert MPD diffractometer with a Cu K_α radiation source. The working voltage and filament current was 45 kV and 40 mA, respectively. The phase identification was based upon the Joint Committee for Powder Diffraction Standard (JCPDS) database. Imaging was completed with a

Hitachi s-4700 II Field Emission Scanning Electron Microscope at 15 kV accelerating voltage and 10 μA emission current.

3.2 Initial Characterization

3.2.1 MnO_2 Structure

The FESEM images in Figure 3.1a,b are of the interior of the electrode after the polystyrene pore former has been pyrolized via heat treatment in a reducing atmosphere, and before it has been oxidized.

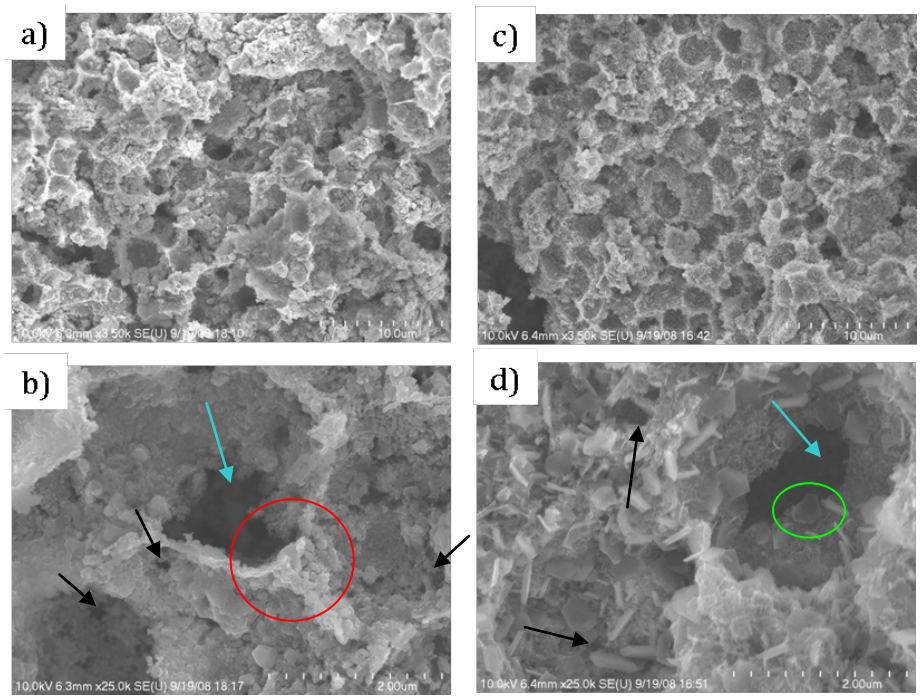

Figure 3.1: FESEM images of the internal structure of the electrode. a,b) Pre-electrochemical oxidation, post-sinter. Clearly visible are three continuous phases with spherical voids. c,d) Oxidized with MnO_2 active material. (Sample content: 0.45/0.55 Ni/Mn, 3 micron voids).

Intimate contact between the Mn and Ni nanoparticles are shown in Figure 3.1b where there is no clear separation between particles. Nano-scale pores denoted by black arrows on the figure, or voids between the nanoparticles, are also visible which is inherent to the powder compaction process due to the packing factor of a random network (0.63). The spherical void space is created by the polystyrene pore former. Figure 3.1b shows a triple point marked by a red circle, where the polystyrene spheres were in contact during compaction. Because the polystyrene is not rigid like the Mn and Ni, some of the spheres deform into a polyhedron shape due to the pressure of the compact forming such triple points and other slightly irregular shapes. A large void, pointed out by the blue arrow, is also seen connecting void space of another polystyrene sphere, further increasing access of the electrolyte to the metal nanoparticles. Figure 3.1c,d shows the electrode after electrochemical oxidation to the MnO_2 electroactive phase. The images display a change in structure of the Mn to MnO_2/Mn_2O_3 along with an increase in surface area of the active material after oxidation (green circle). The now oxidized Mn remains in intimate contact with the conductive Ni phase. The micro (blue arrow) and nanoscale (black arrows) porosity of the electrode is still seen, showing that the access of electrolyte is maintained after oxidation. X-ray powder diffraction was run on unoxidized and oxidized samples held at -0.25V and 0.3V driving toward the Mn_2O_3 and MnO_2 phases respectively. Figure 3.2a shows the θ-2θ diffraction patterns for the unoxidized sample.

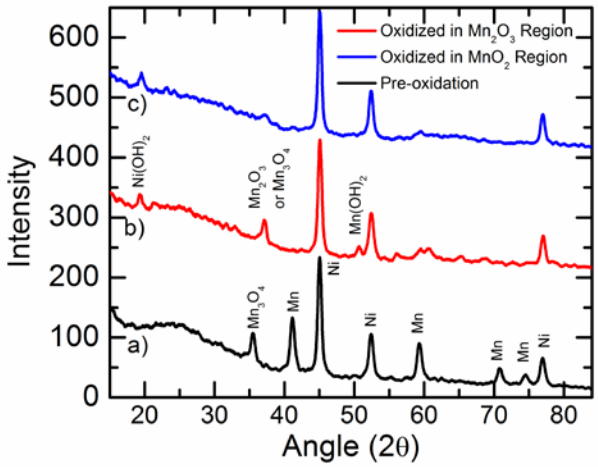

Figure 3.2: XRD of a) unoxidized sample, b) oxidized to active material at lower potentials in the Mn_2O_3 region, c) oxidized to active material in the MnO_2 region.

Peaks at a 2θ of 45.1, 52.5, and 76.9 are signals from the Ni present in the electrode and are seen in all samples. Mn peaks are located at 41.1, 59.3, 70.9 and 74.6 with a Mn_3O_4 peak at 35.4. The Mn_3O_4 is from the native oxide shell that is formed during the powder synthesis process in the as received Mn powder. The heat treatment of the electrode does not reach a high enough temperature to remove this oxide layer. Figure 3.2b is a spectrum of an electrode that was oxidized for 24 hours at -0.25 V vs. Hg/HgO in the Mn_2O_3 region of the Pourbaix diagram. It is apparent that all of the Mn metal peaks are gone, with new peaks associated with Mn_2O_3 or Mn_3O_4 at 37.2 as well as an $Mn(OH)_2$ peak at 50.7. The poor crystallinity of the peak at 37.2, as displayed by the low intensity and peak broadening, makes it difficult to identify in the XRD databases. There is a small signal from $Ni(OH)_2$ at 19.5 due to the oxidation of Ni at these potentials

and pH. Figure 3.2c is the spectrum of an electrode oxidized at 0.3 V vs. Hg/HgO, well into the MnO_2 region. The $Mn(OH)_2$ peak has disappeared and the Mn_2O_3/Mn_3O_4 peak at 37.2 is smaller and more diffuseI, implying the system is becoming even less crystalline. All of the manganes oxide peaks have also shifted to higher values of 2θ, indicating a decrease in the lattice parameter, which should occur when oxidizing to MnO_2 due to the removal of protons from the structure [9].

Cyclic voltammetry was used to characterize the initial performance of the electrodes. Figure 3.3 shows the shape of the curves at varying scan rates. All scan rates show a good capacitive response with the capacitance directly related to half of the area within the curve and inversely related to the scan rate.

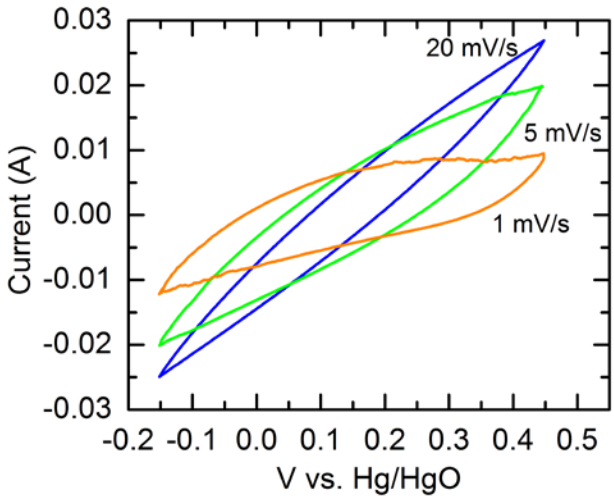

Figure 3.3: Cyclic Voltammerty of an electrode first oxidized in the MnO_2 region at 1mV/s, 5mV/s and 20mV/s from -0.15 V to 0.45 V. (Sample content: 0.45/0.55 Ni/Mn, 1-50 µm voids). Data collected by Allison Engstrom.

From these relationships, the cyclic voltammogram illustrates a higher capacitance with slower scan rates. Slower scan rates provide a longer time for the proton insertion process; therefore, a larger pseudocapacitance is often exhibited. Only once the scan rate was at or below 1mV/s was an oxidation wave observed. At higher scan rates the curves are rather featureless. This type of response is seen for bulk type manganese oxide electrodes, whereas features develop at even slower scan rates or with thin film electrodes where each oxidation phase is easily identifiable. Chronoamperometric holds are a better way to analyze the electrodes as they are more relevant to standard charge/discharge applications.

3.3 Conclusion

The electrode processing was described, where powders of nano-Mn, nano-Ni and micron sized pore former were mixed and formed into the electrode. Sintering in a reducing environment removed the polystyrene pore former and provided a non-oxidizing atmosphere for the Mn and Ni. The electrode was then electrochemically oxidized in 1 M LiOH to form the electroactive manganese oxide. The electrochemical and physical characterization of the electrodes by CV, XRD and SEM were displayed as well.

CHAPTER 4 ELECTRODE OPTIMIZATION

4.01 Introduction

Optimization of the supercapacitor electrode cycling potential and the concentrations of the three components, Mn, Ni and pore former are detailed with reference to percolation theory. Cycling at -0.5 V vs. the open circuit potential (OCP) was found to result in the highest capacities. Mn/Ni concentrations of 55/45 vol% manganese achieved the highest bulk capacities before losses were introduced due to excess mass from the non-electroactive Ni. A uniform pore size of 3µm at 40 vol% yielded the highest capacities.

4.1 Cycling Potential

Holding the electrodes at constant potential was done to study the pseudocapacitive performance. During chronoamperometric cycling, samples were held at incremental potentials from the post-oxidation open circuit potential (OCP) between -0.1 V to -0.8 V versus the OCP for 5000 s. charge/discharge cycles. The integrated oxidative current for each holding potential was used to calculate the specific capacitance in Farads/gram (using the mass of the Mn only) The total specific capacitance is labeled as the composite capacitance which takes into account the mass of the entire electrode. The specific capacitance of only the oxidized manganese is calculated with the mass of just the manganese, which is the standard practice by many in the field. Figure 4.1 is a plot of specific capacitance of both the composite and the Mn vs. the potential held negative of the OCP.

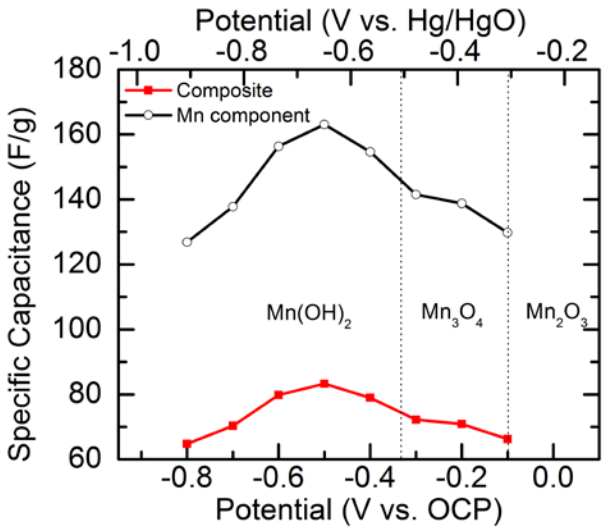

Figure 4.1: Variation of discharge potential. A maximum in capacitance is found at -0.5 V vs. the OCP in the $Mn(OH)_2$ stability region. (Sample content: 0.45/0.55 Ni/Mn, 33% 1-50μm voids). Data collected by Allison Engstrom.

The maximum capacitive performance occurred at -0.5 V versus the OCP which (according to the Pourbaix diagram) corresponds to just below the Mn_3O_4 spinel phase in the electrically conductive $Mn(OH)_2$ phase. It is interesting to note that decreasing the potential even lower into the $Mn(OH)_2$ region does not produce an increase in capacitance. Others have shown that a high concentration of protons, via insertion during the reduction of MnO_2 to other oxide phases, causes irreversibility of cycling of the electrode [9].

4.2 Ni Content

Considering the delicate balance between the three phases present in the electrode, the ratio between the Ni and Mn is optimized first. The volumetric ratios were varied from 0.05 to 0.50 volume fraction Ni to determine the ideal Ni content to achieve the highest composite capacitance. As mentioned before, this fraction only relates the combined volume of Mn and Ni nanoparticles; it does not include the void space volume. Samples were held chronoamperometrically at -0.5V versus the OCP for 5000 sec., then oxidized for the same amount of time at the initial OCP. Figure 4.2 is a plot of specific capacitance of the Mn and composite vs. Ni content.

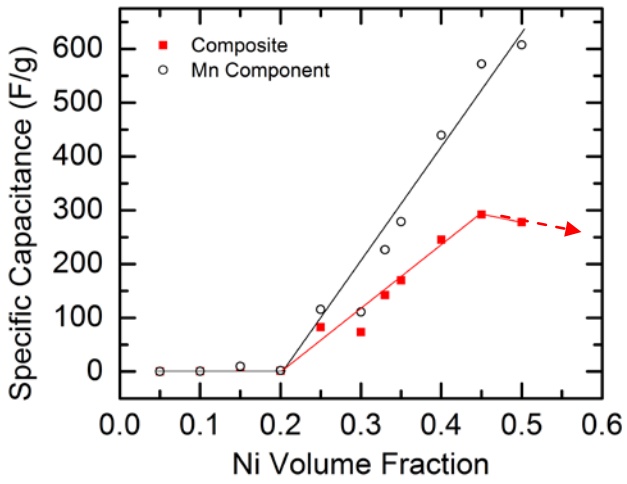

Figure 4.2: : Capacitance in F/g of the active Mn component and the total composite as a function of the Ni content. (Samples content: varied Ni/Mn, 33% 1-50μm void space). Data collected by Allison Engstrom.

From continuum percolation theory, a percolation threshold near 0.25 Ni is expected; Figure 4.2 verifies this prediction. At 0.20 Ni volume fraction the electroactive material has not yet reached the critical percolation threshold, and the capacity is near zero because the bulk of the sample is not electrically accessed. A nonzero capacity is seen at 0.25 Ni signifying the percolation threshold. Above the threshold, the composite capacitance gradually increases to a maximum at 0.45 Ni, and then begins to decrease. The gradual increase in capacity is expected near the percolation threshold and its behavior is described in terms of conductance detailed above (Figure 2.2). At and just past the threshold, the conductance is near zero and slowly rises as more sites are occupied by the Ni. At this point, a finite cluster joining the already infinite cluster increases the probability of percolation but does not contribute to a new parallel path for conductance. Therefore, the newly Ni-occupied sites just past the threshold do not cause large increases in conductance, or similarly capacitance. When the system is fully percolated the value of conductance is at a maximum. The manganese oxide capacitance increases similarly to the composite capacitance with increasing Ni content due to increasing contact with the Ni conducting phase. However, a transition occurs above 0.45 Ni where increasing composite mass by adding more of the higher density nickel has outweighed the increasing capacitance with respect to the manganese oxide component causing a lower total composite capacitance. Therefore, the manganese oxide active component and Ni have reached the ideal concentrations for the composite structure at 45 volume percent nickel, 55 volume percent manganese.

4.3 Pore Former Size and Content

The void size and fractional content was studied at a constant Ni and Mn content of 0.45 and 0.55 respectively. The reported pore-former volume fraction takes into account the total Mn, Ni and pore-former volumes. In contrast to the Ni/Mn percolation threshold, the critical volume fraction of void space is difficult to accurately predict from the above described continuum percolation model. However, the expected the percolation threshold is above the predicted value for the smaller particles, $p_c^{site} = 0.25$, because the size of the pore-former is much larger than that of the Mn and Ni powders [29]. Also, the effect of the pore-former volume fraction on the electrode capacitance is slightly more complicated than that of the Ni and Mn powders because there is concern only with the void volume left behind. These voids not only increase the ionic conductivity throughout the bulk of the electrode, they also increase the surface area of the active materials. The diameter and surface area of the produced voids will affect the capacitance; a trend of increased performance with increasing electrolyte access would be expected with increasing void space. However, the predicted 0.25 percolation threshold may not directly apply here. Uniform void sizes of 3 μm and 11 μm were tested within a range of 10-80 volume fractions. Figure 4.3 is a plot of the specific capacitance of both the composite and the manganese oxide versus volume fraction voids for both void sizes.

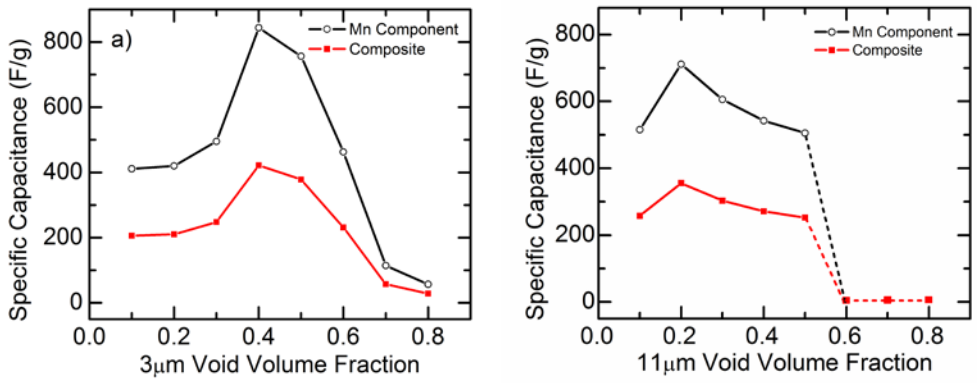

Figure 4.3: Capacitance of the active and composite components for varying void contents and void sizes. a) Void size of 3 μm reaches a maximum of 840 F/g in Mn capacitance at 40 vol% void content and b) with a void size of 11 μm a maximum of 720 F/g is reached of Mn at 20 vol% voids.

The 3 μm voids (Figure 4.3a) show almost constant capacitance below 0.2 volume fraction with a small increase at 0.3 then a sharp increase at 0.4. The behavior of increasing the void content is somewhat analogous to the behavior of conductance in Figure 2.. Just as for conductance, there is only a small increase just above the percolation threshold, but far enough away from p_c there is a substantial increase. The percolation threshold in this case is between 0.2 and 0.3 void content, and with only a small increase seen at 0.3, it is likely p_c is closer to 0.3. This is higher than what is predicted with the general form of the percolation model, which is in agreement with the theory that larger spheres have higher percolation thresholds than smaller spheres [29]. At 0.3 volume fraction, there are not enough pathways for ionic conduction to contact all the manganese oxide present in the electrode for both oxidation and cycling producing lower capacitances. Increasing the

volume fraction to 0.4 provides a substantial increase in capacitance to a maximum value, signaling that all of the manganese oxide in the electrode has access to the electrolyte. Above this void content, if the structure was behaving exactly according to percolation theory, the capacitance for the manganese oxide would continue to increase, and the bulk capacitance would decrease at some value just as what was seen for Mn/Ni concentration in Figure 4.2. This, however, is not the case because the structure begins to lose mechanical stability and consequently electrical connectivity to active surface area causing the capacitance to decrease. This is clearly seen at the 70-80% void content where the capacitance drops to below 100F/g for both the composite and manganese oxide component.

The p_c for the 11 μm void case (Figure 4.3b) appears much lower than that of the 3 μm void electrode contradicting previous work showing that increasing the size of the particles increases the percolation threshold [29]. This model for continuum percolation of systems of different size particles shows that the threshold of the 11 μm voids is greater than, but still near the same as that for the 3 μm voids. However, there are several complicating factors suggesting that Figure 4.3b is not indicative of the actual percolation threshold. At 0.1 volume fraction voids, the capacitance for the 11 μm case for both the manganese oxide and the composite is larger than that of the 3 μm case. This is because the 11 μm voids produce more surface area than the 3 μm voids, and therefore have access to more manganese oxide. The "p_c" is found at 0.2 void content; however it is approximately 100 F/g

less than the maximum in the 3 µm void case. This could be due to decreased mechanical stability causing a decrease in connectivity to the active component. In fact, above 0.2, the electrode becomes more unstable and at 0.50 and above, the structures lose all mechanical stability and are unable to be electrochemically tested. From this analysis, it is clear that Figure 4.3b is not indicative of the actual percolation threshold.

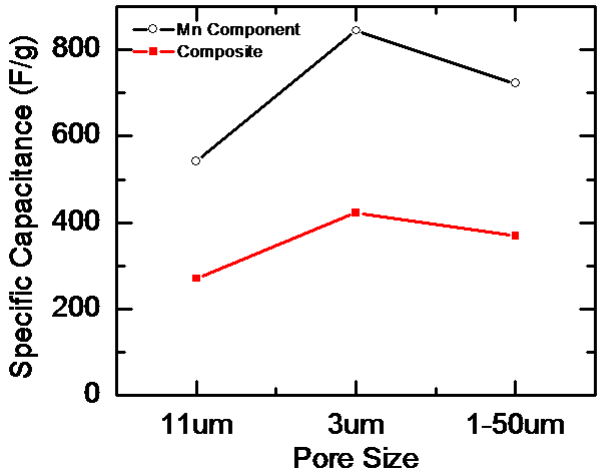

Figure 4.4: Specific capacitance at 40 volume percent voids for 3µm, 11µm and 1-50µm void sizes. (Sample content: 0.45/0.55 Ni/Mn, varied void content).

Comparing different void sizes at a constant 0.4 void volume fraction is shown in Figure 4.4b. The 3 µm voids produce the highest values of capacitance as compared to the 1-50 µm and 11 µm voids. Increasing the size of the voids is expected to produce a higher surface area exposed to the electrolyte and therefore higher capacities. However, this effect is muted by the decrease in mechanical stability of the electrodes as the void diameter increases. Therefore, the 3 µm

voids at 0.4 void volume fraction are the optimal void size and concentration, respectively.

4.4 Fully Optimized Electrode

The optimal tri-continuous structure has been found to maximize the composite specific capacitance. A Ni/Mn content of 0.45/0.55 was determined to give the ideal electrical conductivity maximizing the capacitance of the composite electrode. Analysis of the pore-former has yielded the best performing void content and size of 0.4 volume fraction and 3μm, respectively, allowing the optimal access to the electroactive MnO_2. The optimized tri-continuous fully percolated electrode was cycled at varying charge/discharge times to determine the capacity dependence on the length of the cycles (-0.5 V vs. OCP discharge, 0 V vs. OCP charge). Figure 4.5a is the current vs. log time response to cycling at the various durations.

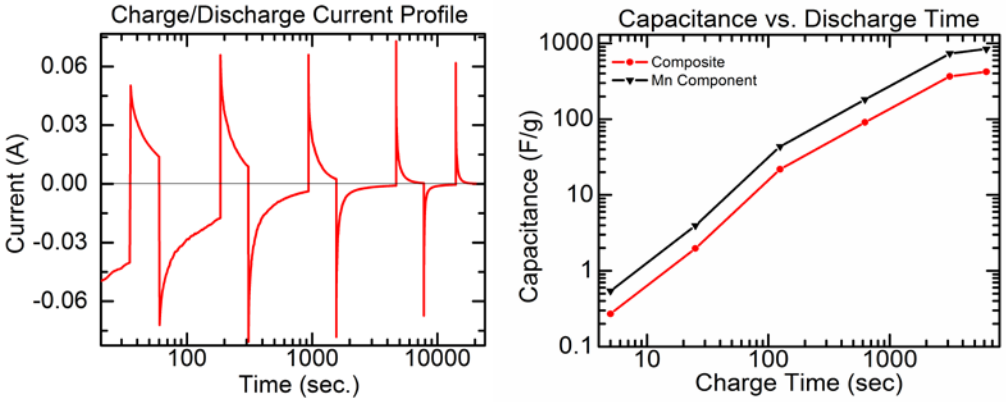

Figure 4.5: a) charge/discharge current profile and b) Capacitance at varying times for a fully optimized electrode.

A total of 6 charge/discharge cycles were performed, but the first cycle of 10 seconds is not plotted in this figure to give more clarity to the subsequent cycles given the log scale. At shorter times, the current shows that they are far from a limiting value, or in other words, far from being fully saturated, whereas at the longer holding times the current starts to reach a limiting value. Figure 4.5b is a log/log plot of capacitance vs. discharging time. At long enough times, > 3600 seconds, the capacitance begins to level off, signaling the existence of a limiting value of capacitance. At infinite time, the capacitance will reach this limiting value associated with complete saturation of the pseudocapacitive effect. The maximum specific capacitance is calculated from the 6250 second cycle and is recorded as 844 F/g for the Mn component and 422 F/g for the composite.

4.5 Conclusion

An innovative technique for designing a bulk composite manganese oxide electrode with excellent pseudocapacitive performance was performed and characterized. Percolation theory was used to produce an electrode architecture with a hierarchically designed tri-continuous percolated network. The three phases include the electroactive pseudocapacitive MnO_2, electrically conductive Ni and a templated pore network. The result yielded an electrically conductive percolated network allowing complete electrical access to the active component and a bulk porous system on the micro- and nano-scale creating pathways for ionic conduction of the electrolyte. The optimized structures yielded excellent Mn specific capacitances of up to 844 F/g and a composite capacitance of 422 F/g.

CHAPTER 5 ELECTRODEPOSITION IN IONIC LIQUIDS

5.01 Introduction

In the following chapter, a background of ionic liquids (ILs) used for electrodeposition of a variety of metals is given. Advantages to working in ILs range from low vapor pressure to a large electrochemical stability window. However, challenges to working in non-aqueous media, such as salt solubility and synthesis impurities, are also given. Introduction to Zn deposition in aqueous-alkaline systems and historical problems in Zn battery applications are presented. This history provides the reasoning behind exploring ILs as an alternative electrolyte to aqueous systems. Background on Zn deposition in various ILs shows a lack of characterization of the electrochemical properties and mechanisms for the different growth morphologies seen in each system. The IL studied in this work is also presented.

5.1 Background

The use of ionic liquids (IL) as electrolytes for the electrodeposition of metals has gained interest in recent years. There are several advantages of electrodeposition of metals in ILs. The most obvious benefit is that metals can be deposited that are not stable in aqueous solutions such as Al, Si, Ge and Ti [31]. Another advantage is the large electrochemical stability window allows for the avoidance of side reactions such as hydrogen evolution during the deposition where higher quality deposits are obtained by removing H-codeposition. Palladium, for example, produces very brittle deposits in aqueous media, whereas in an IL, shiny,

nanocrystalline deposits are formed [31]. The vapor pressure in ILs is also much lower or even immeasurable than that of water lending itself to applications where H_2O evaporation is an issue [32]. A wider range of stable deposition temperatures are accessible than in aqueous media which allows access to a wider range of electrodeposition conditions.

There are several challenges to working in ionic liquids including hydrophobicity/hydrophilicity, complexation chemistries, conductivity and organic synthesis impurities. Hydrogen co-deposition can be removed with an IL that is free of H_2O, however, the hydrophilicity of the IL as well as the metal salt determines the equilibrium water content. Fortunately, ILs the hydrophobicity is tunable based on the anion and cation selection to fix the water content of the system. However, if a highly hydrophilic metal salt is introduced into the system, a significant amount of water is likely present if care is not taken to control it. In many ionic liquids, the solubility of the salt, can be much lower than that of aqueous systems. This produces low limiting currents, which can require longer plating times and can produce a lower yield. The conductivity, σ, in ILs is similar to that of organic systems such as Li-ion batteries with values on order of 1-20 mS/cm, whereas in high concentration acid/base aqueous solutions, conductivities are on the order of magnitude higher (500-700 mS/cm) [33]. Due to the nature of the organic synthesis techniques of ILs, there is some controversy regarding their purity. Repeatability from batch to bactch of IL is challenging especially with respect to electrodeposition where impurity adsorption can deleteriously affect the

morphology. A variety of synthesis and purification techniques can yield different amounts of impurities including organic precursors, halides, water and impurities from incomplete metathesis reactions.

5.2 Zn Electrodeposition

Zn deposition in aqueous electrolytes has been extensively studied due to advantageous properties for Zn rechargeable battery applications. Its negative standard potential,-0.76 V vs. SHE, and large hydrogen reduction overpotential have made Zn an excellent anode material in alkaline aqueous systems. Zn is earth-abundant, non-toxic and inexpensive, providing an excellent renewable energy material. There are several battery cell systems that have been highly successful such as Zn-Ni, Zn-MnO_2 and Zn-air. In Zn-Ni batteries, the Ni undergoes transformation from $Ni(OH)_2$ to NiOOH (oxyhydroxide) at the positive electrode. This system has limited cycle life due to issues related to the shape change of the electrode as well as dendrite formation on the Zn side. Zn-MnO_2 systems require precise control over the charging voltage to ensure the MnO_2 phase is properly formed and no other oxidation state is formed which leads to loss of capacity. There is also loss of performance related to the to Zn ions entering the MnO_2 positive electrode during cycling, significantly decreasing battery lifetime [34]. Zn-Air systems have high specific energies and thus have potential for electric vehicle applications. In general, a porous Zn electrode is used at the anode and the oxygen reduction reaction (ORR) is conducted at the cathode. However, the efficiency and cycle life of these cells is limited due to

H_2O reduction during Zn deposition [35]. One challenge in Zn-Air systems comes from electrolyte evaporation since the cell is open to air, and with low vapor pressure ILs this problem is removed. Another challenge is that alkaline systems present problems with dendrite formation at the Zn electrode during recharging. Significant effort towards decreasing the dendrite formation was done with the use of additives and different charging methods to alter grain size and growth morphology [36,37]. The focus of this work is to characterize Zn deposition in ILs and to determine what factors influence dendritic growth, while keeping in mind a direct application to Zn-Air systems, where the anode can be subjected to ambient air and humidity conditions.

Dendritic Zn growth in alkaline media described above, as well as other Zn related applications such as anti-corrosion coatings have lead to significant interest in Zn deposition in ionic liquids. Studies have shown that Zn was successfully deposited from chloroaluminate based ionic liquids, however, these ILs tend to react with water and air [38]. While this is suitable for systems which are fully closed off from the environment, deposition from air stable ILs is of interest for use in ambient conditions such as Zn-Air batteries. Deposition of Zn from $ZnCl_2$ in various chloride based ILs such as Choline Chloride and 1-ethyl-3methylimidizolium chloride due to a high salt solubility [39-41]. Most of the deposition conditions that yield good morphology are performed at high temperatures in order to remove the H_2O brought into the system by the hygroscopic $ZnCl_2$ as well as to increase the deposition kinetics. Bakkar and

Neubert [41], however, reported good Zn morphology in both air and H_2O stable Choline Chloride/Urea – $ZnCl_2$ with significant H_2O (3-7 wt%) present at lower temperatures. It seems that a somewhat diverse selection of ILs have been studied for Zn deposition, however, an in depth study of deposition parameters such as overpotential dependence and H_2O content has not been done in any system to date.

Bis(trifluoromethanesulfonyl)imide or $[NTf_2]^-$ based ionic liquids have been studied for use in battery technologies due to their large stability window and non-volatility. The $[NTf_2]^-$ anion has a large negative limit making it applicable to batteries in need of a very cathodic potential such as Li and Zn. Yamamoto and coworkers deposited Zn in trimethyl propylammonium NTf_2 – $Zn(NTf_2)_2$ at 120 °C, although the deposits were highly rough and irregular [42]. Another group impregnated $Zn(NTf_2)_2$ in a conducting polymer gel with 1-ethyl-3-methylimidazolium NTf_2 ionic liquid testing the battery cycling properties, without analysis of morphology [43]. Most of the metal electrodeposition work has focused on whether or not the metal deposition is possible in a particular IL. However, there are only a few studies determining the morphological effects of the IL on the deposited metal or how the variations in H_2O content affects the morphology [38,44,45]. Because the Zn-Air batteries are subjected to air and humidity, an H_2O analysis is absolutely necessary.

The goal of this research is to electrochemically characterize Zn deposition, along with a complete analysis of the deposition morphology in the air-H_2O-stable ionic $[NTf_2]^-$ liquid N-ethyl-N-methylmorpholinium bis(trifluoromethanesulfonyl)imide, $[C_2nmm][NTf_2]$, Figure 5.1, with $Zn(NTf_2)_2$ as the Zn containing salt. $[C_2nmm][NTf_2]$ provides the ability to operate in a wide temperature range and higher salt solubility (0.7 M) compared to other non-aqueous IL electrolytes. $[C_2nmm][NTf_2]$ is a new IL and only some of its properties, such as stability window, thermogravimetric data and conductivity, have been documented by only one other group [46,47]. I am the first to complete an analysis of Zn electrodeposition in this IL.

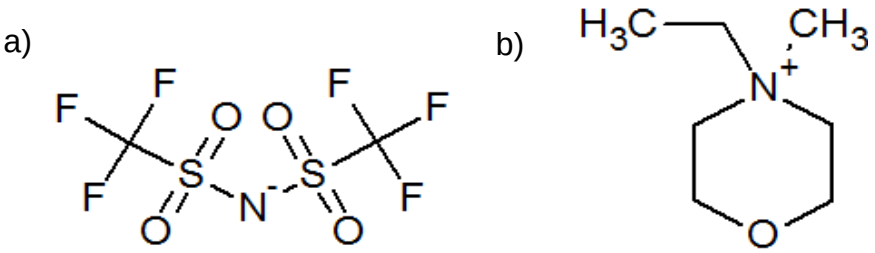

Figure 5.1: Structure of the ionic liquid N-ethyl-N-methylmorpholinium bis(trifluoromethanesulfonyl)imide $[C_2nmm][NTf_2]$ with a) $[NTf_2]^-$ anion and b) $[C_2nmm]$ cation (drawn in ChemSketch Freeware).

CHAPTER 6 ELECTROCHEMICAL CHARACTERIZATION

6.01 Introduction

Electrochemical characterization in $[C_2nmm][NTf_2]$ by completing voltammetry in neat and Zn containing solutions. Overpotentials seen on Cu{111} thin film and polished Zn working electrodes are analyzed. It was found that nucleation, diffusion and charge transfer overpotentials all play a roll under various conditions. Where nucleation overpotential is substrate dependent, diffusion and charge transfer overpotentials are influenced by the Zn complexation / solvation and the structure of the IL itself. Experiments were done determining how the addition of water effects the kinetics and diffusion of Zn in $[C_2nmm][NTf_2]$ through cyclic voltammetry and rotating disk electrode analysis. It was found that increasing water leads to increasing exchange current densities and increased diffusion coefficients.

6.1 Experimental

6.1.1 $[C_2nmm][NTf_2]$ Analysis

The primary ionic liquid used in this study was $[C_2nmm][NTf_2]$, and was synthesized by Fluidic Energy The $[C_2nmm][NTf_2]$ passed a AgCl precipitation test for Cl^-, thin layer chromatography for amine consumption and the pH reached neutrality as the first chemical tests to deem it chemically pure. The $[C_2nmm][NTf_2]$ also underwent elemental analysis (EA) to further determine the purity [48,49]. Special measures were not taken to dry the IL specimens prior to elemental analysis; rather, the waters of hydration are determined by Karl Fischer

analysis in the calculated CHN values. Samples within 0.4 wt% of the calculated C, H and N concentrations calculated for $[C_2nmm][NTf_2]$ are considered passing. Table 6.1 shows the calculated and measured values for C, H and N yielding a passing result. For more information on these testing methods, see Chapter 10.2.

Table 6.1: Elemental Analysis of $[C_2nmm][NTf_2]$

	C	H	N
Calculated	26.3	3.9	6.8
EA	26.1	4.0	6.7

The Zn salt, $Zn(NTf_2)_2$, was synthesized by dissolving ZnO powder in $HNTf_2$. The excess unreacted ZnO was removed with a 0.2 μm syringe filter. The $Zn(NTf_2)_2$ was then concentrated at 100 mbar / 60 °C initially, then at 30 mbar / 85 °C until only the solid remained.

6.1.2 General Electrochemical

All experiments in ionic liquids were done in a nitrogen glove box to better control the experimental conditions. Voltrammetry experiments were conducted in small volume (~1 mL) 3-electrode cells. For experiments in neat solutions without Zn (Figure 6.1), Pt working electrode, a coiled Pt-Ir counter electrode and a Pd-H reference electrode were used. The Pt and Pt-Ir were acid cleaned in heated, concentrated HNO_3 and H_2SO_4, rinsed in UPW, then flame annealed with a hydrogen flame. The Pt working electrode was then polished down to 1 μm Alumina. The Pd–H electrode was made by holding at –0.5 V vs SCE in 0.1 M

H_2SO_4 electrolyte until there was visible bulk hydrogen evolution from the surface. For experiments in Zn containing solutions, the working electrode was a patterned Cu thin film on a 1 mm glass substrate. The sample was prepared in a $5x10^{-10}$ Torr base pressure ultra high vacuum system fitted with DC magnetron sputter sources. A 10 nm Cr adhesion layer was first deposited, followed by Cu at 1 Å/s to a thickness of 500 nm. The films have a strong Cu {111} texture confirmed by XRD. The counter electrode was a Zn wire coil and the reference electrode was a Zn wire.

All solutions were deaerated with argon to remove oxygen and water at ~50 °C. The water content was tested with a Karl Fischer (KF) titration method and was found to be < 400 ppm H_2O for 0.1 M $Zn(NTf_2)_2$ solutions, though drying down further was difficult due to the hydrophilic nature of $Zn(NTf_2)_2$. For solutions in which the H_2O content was of interest, the content was stabilized by purging with humidified/dry Ar mixtures measured via a hydrometer, and was confirmed with the KF as well.

6.1.3 Rotating Disk Electrode

In order to examine the diffusion characteristics as a function of H_2O content (humidity), rotating disk electrode (RDE) system was utilized. The working electrode was a 0.2 cm^2 polished Zn disk, the counter electrode was a Zn wire coil, and the reference electrode was a Zn wire. Due to the small amount of electrolyte available, a small RDE cell was designed similar to that in Bartlett et. al. to use only 8 mL of electrolyte [50]. All work was done with an Ar deaerated 0.1 M $Zn(NTf_2)_2$ solution, and the water controlled through humidifying. The disk was held chronoamperometrically at varying potentials and the rotation was changed from 100-900rpm. The limiting current in the diffusion limited regime was recorded at each rotation rate and used to determine the diffusivity. The kinetic parameters as a function of H_2O concentration was determined by Butler-Volmer analysis using slow scan rate cyclic voltammetry.

6.2 $[C_2nmm][NTf_2]$

Cyclic voltammetry on a platinum working electrode was completed in the neat electrolyte at 50 °C, well above the melting temperature of T_m=29.2 °C [46] reported for $[C_2nmm][NTf_2]$. The electrochemical window of $[C_2nmm][NTf_2]$ is 5.5 V while water has a 1.23 V stability window (Figure 6.1a). There are several unidentified redox peaks that may be related to the adsorption of both the cation and $[NTf_2]^-$ anion as well as impurities from the IL synthesis. These impurities include chloride and protonated n-methyl morpholine with probable levels in the µM and mM range, respectively. An in-depth discussion on universal impurities

in ionic liquids is presented in Chapter 10. The addition of 0.8 M H_2O to the $[C_2nmm][NTf_2]$ (Figure 6.1b) shrinks the electrochemical window to approximately 2.5 V where significant water reduction (-0.55 V) and oxidation (+0.75 V) is present.

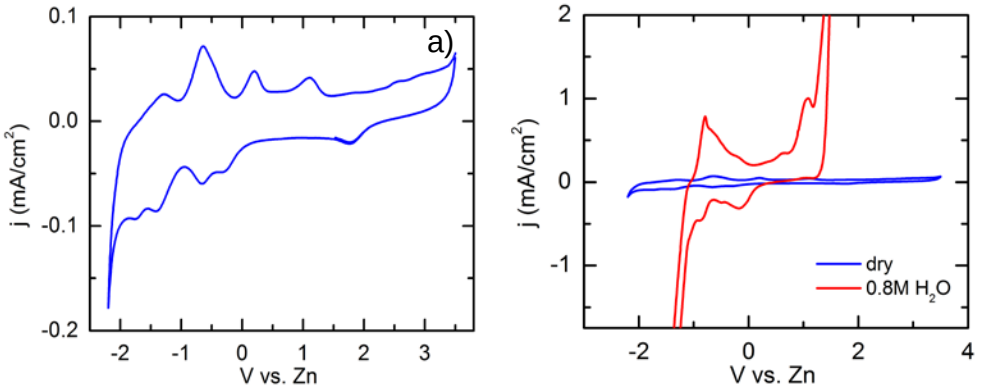

Figure 6.1: Cyclic voltammetry at 100 mV/s in $[C_2nmm][NTf_2]$ at 50 °C on a platinum WE a) without water, b) overlaid with 0.8 M H_2O. Data provided by Elise Switzer.

6.3 Overpotential of Zn Deposition in $[C_2nmm][NTf_2]$

6.3.1 Overpotential Overview

Zn-ions were added to the neat $[C_2nmm][NTf_2]$ electrolyte to study the redox behavior and morphology of electrodeposited Zn. Cyclic voltammetry on a Cu{111} thin film substrate was completed in a dry solution of $[C_2nmm][NTf_2]$ and 0.1 M $Zn(NTf_2)_2$ at two temperatures, 50 °C and 70 °C shown in Figure 6.2a.

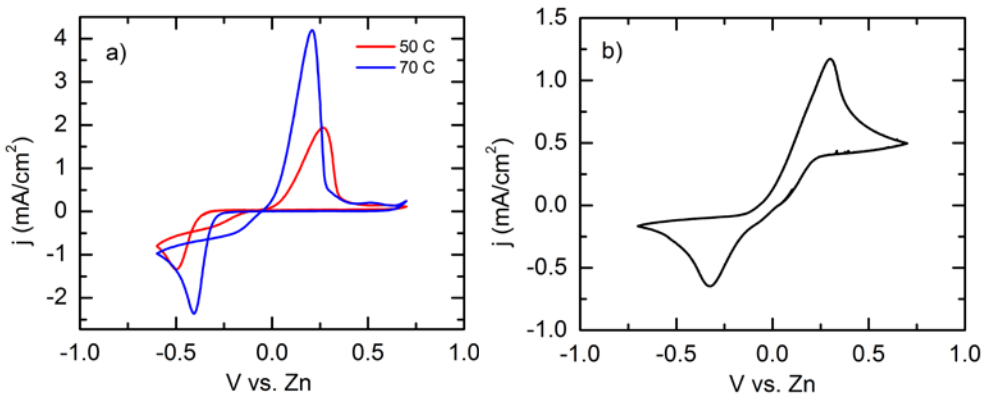

Figure 6.2: Cyclic voltammetry at a) 10 mV/s on a Cu {111} thin film working electrode (50 °C and 70 °C) and b) at 1 mV/s on a polished Zn disk working electrode (50 °C) in $[C_2nmm][NTf_2]$ + 0.1 M $Zn(NTf_2)_2$ deaerated with Ar (H_2O < 400ppm).

At 50 °C, the overpotential for $Zn^{2+} + 2e^- \rightarrow Zn$ (s) increases and the kinetics slow down as shown by the decrease in steepness of the slope as compared to redox at 70 °C. Voltammetry on a polished Zn disk working electrode at 50 °C, however, does not show as pronounced an overpotential for deposition (Figure 6.2b).

It is useful to introduce possible origins of overpotential in order to better understand the differences in behavior seen in Figure 6.2a and b. There are four typical sources of overpotentials in any electrochemical system; the charge-transfer overpotential, the reaction overpotential, the diffusion overpotential and the crystallization overpotential [51]. The charge-transfer overpotential, described by Marcus, is due to the change in the free energy of activation in the outer

sphere[52]. Outer sphere electron transfer takes place when the original coordination spheres of the reacting species are conserved in the activated complex [53]. Conversely, inner sphere electron transfer occurs when the activated complex shares a ligand. It is assumed that the reduction of $Zn(NTf_2)_2$ is an outer-sphere reaction. The reaction overpotential takes place when the chemical reaction rate constant is limiting. A chemical reaction is inherently independent of potential, but if a chemical step is needed to complete the overall electrochemical reaction, that reaction will be hindered if the chemical reaction is slowed. A diffusion overpotential is related to the mass transfer to the surface prior to the electron transfer event, involving the formation of a concentration gradient in the diffusion layer. Finally, the crystallization overpotential, or nucleation overpotential, takes into account the incorporation or removal of atoms into the lattice structure. The overpotential seen for Zn deposition in $[C_2nmm][NTf_2]$ come from 3 of the 4 types described above, excluding the reaction overpotential.

6.3.2 Nucleation Overpotential

In the case of deposition on Cu {111} the magnitude of the overpotential is due to mainly nucleation of Zn. It takes more energy to drive hexagonal Zn to deposit on FCC Cu. This is evidenced by the lack of overpotential for Zn deposition on Zn. Therefore, the nucleation overpotential on Cu will disappear when there is enough Zn to fully cover the surface of the Cu.

6.3.3 Diffusion Overpotential

There is also a contribution of diffusion overpotential which is independent of the substrate. The diffusion overpotential involves the formation of a concentration gradient in the diffusion layer. Figure 6.3 is a plot of Zn deposition and stripping at 50 °C with varying H_2O contents.

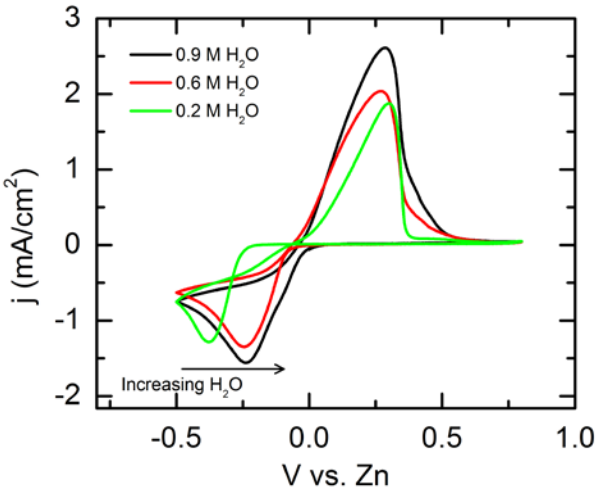

Figure 6.3: Cyclic Voltammetry at 10 mV/s on a Cu {111} thin film working electrode varying H_2O concentration. $[C_2nmm][NTf_2]$ + 0.1 M $Zn(NTf_2)_2$ deaerated with Ar at 50 °C.

When there is enough H_2O in the system, ($X_{H20}/X_{Zn} > 6$), it is more favorable for the Zn^{2+} to be solvated by the water than complexed with the $[NTf_2]^-$ and forms $[Zn(H_2O)_6]^{2+}$ (see discussion below). When there is no water is only complexed with $[NTf_2]^-$ and is $Zn(NTf_2)_2$. When the water content is low, $X_{H20}/X_{Zn} < 6$, there is a mixture of both hydrated Zn^{2+} as well as $Zn(NTf_2)_2$. This difference in solvation/complexation complicates the diffusion process. Diffusion of the molecules takes place by moving through the voids in the IL. $Zn(NTf_2)_2$ is a

large molecule and must rearrange more ions and voids to produce more space (compared to the space needed for the smaller molecule of $[Zn(H_2O)_6]^{2+}$) in order to move through the IL. Therefore, movement of $Zn(NTf_2)_2$ yields more viscous drag and possibly a larger concentration gradient contributing to a larger diffusion overpotential. A more in depth discussion of diffusion in the IL with the addition of water is presented in See Chapter 6.4.1.

6.3.4 Charge-Transfer Overpotential

Binding Energy

It was previously proposed that the charge-transfer overpotential could be contributing significantly to the decrease in overpotential with increasing H_2O content. It was suggested that solvent dynamics (Model 2 below) was playing a large role, however, after further discussion and literature review, it was found not to be the case. Charge transfer with respect to binding energy and electron tunneling distance does play a role due to differences in complexation/hydration and the structure of the double layer, though they may not be as large of a contributor as nucleation and diffusion overpotential. For completeness, the discussion for the basis of charge-transfer overpotential is given below.

The charge-transfer reaction is dependant on the activation energy of the anodic and cathodic reactions separately, and the potential dependence of these energies helps to define the relationship between current (reaction rate) and overpotential [51]. In the case of the cathodic deposition overpotential, dehydration

/ hydration (aqueous) or decomplexation / complexation (IL) of the metal cation, and ionization energy are all included in the energy needed to deposit the metal. In the aqueous case, where Zn^{2+} is solvated by six H_2O molecules (Figure 6.4a), the H_2O-Zn bonds are removed and replaced by coordinating metal ions before incorporation into metal lattice as Zn^0 [54].

a) b)

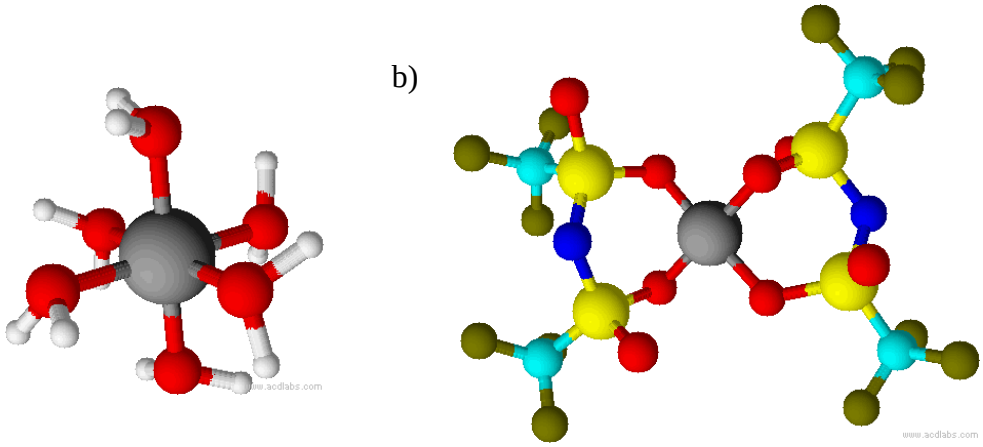

Figure 6.4: The molecular structure of a) Zn hexaaqua $[Zn(H_2O)_6]^{2+}$ where Zn is in the center of the molecule surrounded by 6-H_2O molecules and b) bidentate $Zn(NTf_2)_2$ (drawn in ChemSketch Freeware).

At high enough H_2O contents ($X_{H20}/X_{Zn} \geqq 6$) in the IL, the Zn favors solvation by H_2O. In the case of $Zn(NTf_2)_2$, the Zn is bidentate with each $[NTf_2]^-$ anion and binds with two oxygen atoms per $[NTf_2]^-$ (Figure 6.4b). The same process that occurs in aqueous media must occur with the $[NTf_2]^-$ complexed Zn in order for it to incorporate into the metal lattice, however, the binding energy for the $[NTf_2]^-$ [55] is larger than that of the $[Zn(H_2O)_6]^{2+}$ [56], which means that it is easier to reduce the Zn^{2+} from the water than it is from the $[NTf_2]^-$.

Marcus Theory

There are also two other possibilities effecting charge-transfer as described by Marcus Theory. Model 1 is related to the tunneling barrier (distance and height of the barrier) at which the species must transfer the electron, and Model 2 is related to the effect of solvent dynamics and the reorganization of the solvent molecules in order to transfer the electron. The expression for the kinetics of charge transfer is necessary to in order to introduce these models [53],

$$k = K_p \kappa_{el} \nu_n \exp[-(\Delta G^*_{os} + \Delta G^*_{is}).\,/\,RT, \tag{6.1}$$

where K_p is a constant corresponding to the ratio of the reactant concentration at the point of electron transfer and the bulk concentration, ν_n is the nuclear frequency factor, κ_{el} is the electronic transmission coefficient, and ΔG_{os}^* and ΔGi_s^* are the free energy of the outer-shell and inner-shell electron transfer respectively. For the following discussion, the contribution of ΔGi_s^* is small and will not be considered. Marcus developed the relationship for the activation barrier of outer-sphere electron transfer [57]

$$\Delta G^*_{os} = \frac{e^2}{8}\left(\frac{1}{a} - \frac{1}{R_e}\right)\left(\frac{1}{\varepsilon_{op}} - \frac{1}{\varepsilon_s}\right), \tag{6.2}$$

where, a is the molecular radius, R_e is the reactant-electrode image distance, and ε_{op} and ε_s are the optical and static dielectric constants. The R_e is the distance from the center of the reactant molecule to its mirror image in the electrode. The ε_{op} and ε_s are related to the electronic and orientation polarization of the solvent [58]. Comparing the molecular radius of hydrated vs. the complexed Zn, and assuming for example that $R_e = 2a$ for both cases, the larger $Zn(NTf_2)_2$ yields a lower

activation energy for outer-sphere electron transfer. The other terms of interest in the kinetics equation are v_n and κ_{el}. The nuclear frequency factor is the effective frequency of the reacting species at which the transition state is reached by the rearrangement of nuclear coordinates. Or said another way, v_n is the number of attempts on the energy barrier related to bond vibrations and solvent motion. The electronic transmission coefficient denotes the probability of the electron tunneling when the aforementioned nuclear transition state is formed.

Model 1: Electron Tunneling

The model where electron tunneling is the dominant method for charge transfer will be treated first with the expression for κ_{el}

$$\kappa_{el}(x) = \kappa_{el}^{0} \exp(-\beta x), \tag{6.3}$$

where x is the tunneling distance, and β is related to the height of the energy barrier [53]. The probability tunneling, therefore, exponentially decays with increasing barrier height or distance. When $\kappa_{el} < 1$, the system is nonadiabatic and the reactants weakly interact with each other. This causes the a small potential gap between the lower and higher states on the energy curves, $V_{12} < kT$. A consequence of this is, the probability of transitioning to the higher state increases and there is sampling of both lower and upper energy states before the reaction is completed and the value of $\kappa_{el} < 1$ [58]. Alternatively, in the adiabatic case, the reactants strongly interact with a high probability of completion of the reaction step allowing the system to remain on the lower energy curve, with $\kappa_{el} = 1$. The $Zn(NTf_2)_2$ has a higher overpotential than $[Zn(H_2O)_6]^{2+}$ shown in Figure

6.3. By applying the preceding model, it is likely that the $Zn(NTf_2)_2$ is farther away from the surface of the electrode and has a larger tunneling barrier height/distance.

PZC/Double Layer Structure

Furthermore, the structure of adsorption of the IL as well as the double layer structure may have an impact on the electron tunneling barrier. In order to introduce the double layer (DL) structure, the orientation of the anion/cation on the surface must be considered. Adsorption of ions are generally oriented at an angle to the surface, near the potential of zero charge (PZC) and can even lie flat at excessive potentials [59,60]. If the surface is charged positive of the PZC, the cation is repelled, whereas if it is charged negative, the anion is repelled. For the case of $[C_2nmm][NTf_2]$ on Pt, the PZC is at ~ +1.2 V vs. Zn. (I completed this experiment in both $[C_2nmm][NTf_2]$ and $[C_4mpy][NTf_2]$ on Pt working electrodes, however the experimental details do not give significant insight into the double layer structure and will not be reported in this manuscript.) Therefore, during Zn deposition, the electrode is negatively charged and the cation should be adsorbed onto the surface, though the exact orientation is unknown. However, it has been found by that the structure of the double layer is not just one layer thick. It can be many layers depending on the anion/cation of the IL, as well as the holding potential [61-63]. It is also possible that in the presence of H_2O, the layered structure of the double layer may have significantly different character, allowing the complexed or hydrated Zn to get closer to the surface decreasing this tunneling effect.

Model 2: Solvent Dynamics

The effect of solvent reorganization dynamics on the kinetics of electron transfer is treated in the term for ν_n. In systems where the inner-sphere electron transfer is negligible, the equation for ν_n is equal to ν_{os}, the outer-sphere frequency factor, given by:

$$\nu_n = \tau_L \left(\frac{\Delta G^*_{os}}{4\pi k_B T} \right)^{1/2}, \tag{6.4}$$

where τ_L is the longitudinal solvent relaxation time, which is related to the Debye relaxation time, τ_D, by the ratio of the dielectric constants, ε_{op}, and the ε_s [64],

$$\tau_L = \frac{\varepsilon_{op}}{\varepsilon_s} \tau_D . \tag{6.5}$$

The Debye model for τ_D considers a sphere that is large with respect to the solvent molecule, moving in a viscous incompressible continuum [65]. This analysis yields an expression for τ_D, which is proportional to the viscosity, η, and the molecular radius, a, over the temperature, T,

$$\tau_D = 4\pi\eta a^3 / kT . \tag{6.6}$$

The Debye relaxation time is defined as the time it takes, after the electric field has been turned off, for the polarization to relax [66], and is therefore dependant on the rotational dynamics of the molecule. Conversely, the τ_L, involves translational and small hindered rotations that screen the field. Longitudinal relaxation generally occurs faster than Debye relaxation because there is no net-motion of molecules [67]. The derivation of ν_n assumed a nonadiabatic system, where the reactants weakly interact and the energy gap is $V_{12} < kT$ and $\kappa_{el} < 1$ [58].

Often the nonadiabatic case is referred to as overdamped solvent motion, referring to the hindrance of the rotational motion (τ_D) of individual dipoles by the friction applied by the surrounding solvent molecules [68]. The relaxation time, however, was determined as too fast to influence charge transfer, therefore Model 2 does not apply to the charge-transfer overpotential argument [69].

6.4 Kinetics and Diffusion in 0.1 M $Zn(NTf_2)_2$

6.4.1 Zn Diffusion: RDE

In order to better understand the diffusion characteristics of Zn in $[C_2nmm][NTf_2]$, rotating disk electrode (RDE) experiments were completed. RDE is a hydrodynamic method by which an electrode is rotated with respect to the solution producing convective mass transport of reactants to the surface of the electrode [53]. Advantages to RDE include high precision and the ability to reach steady state rapidly where double layer charging is negligible. The velocity profile to the electrode was determined for RDE, thereby allowing for solutions to the hydrodynamic problem and convective diffusion equation for the steady state. From these equations, the determination of both kinetic parameters and diffusivity are straightforward. Figure 6.5a and b are representative plots to show the experimental method by which the diffusivity was calculated. The limiting currents were recorded at rotation rates from 100-900 rpm at several overpotentials in the diffusion limited regime (Figure 6.5a). A Koutecky-Levich plot, Figure 6.5b, was constructed from the limiting current values vs. the angular rotation rate, ω.

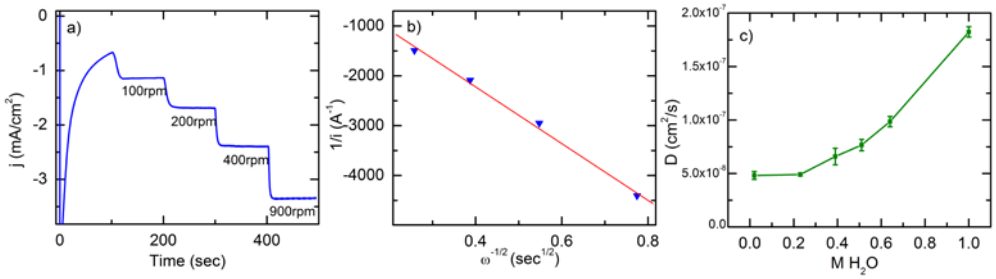

Figure 6.5: Representative plots of a) Current density vs. time at varying rotation rates at a potential in the diffusion limited regime (-0.3 V). b) Koutecky-Levich Plot of 1/i vs. $\omega^{-1/2}$ to determine *D*. $[C_2nmm][NTf_2]$ + 0.1M $Zn(NTf_2)_2$ + 1.8 M H_2O. c) Diffusion coefficient at varied H_2O contents.

The slope of *1/i* versus $\omega^{-1/2}$ in units of rad/s contains the diffusion coefficient, D_R, in cm^2/s,

$$slope = (0.62nFAC_R^* D_R^{2/3} \nu^{-1/6})^{-1}, \quad (6.7)$$

where *n* is the number of electrons, *F* is Faradays constant in C/mol, *A* is the surface area of the electrode in cm^2, C_R^* is the concentration of Zn in solution in moles/cm^3 and *v* is the kinematic viscosity in cm^2/s.

The diffusion coefficient increased from $4.8x10^{-8}$ cm^2/s at the lowest H_2O content, to $1.8x10^{-7}$ cm^2/s at the highest $X_{H2O.}$ These values are lower than diffusion values of $8.4x10^{-6}$ cm^2/s at 23 °C in aqueous $ZnCl_2$ [70] and $5.7x10^{-6}$ cm^2/s and 9.4 $x10^{-6}$ cm^2/s in aqueous Zn acetate at 25 °C and 50 °C respectively [71]. The origin of the decrease in diffusivity at the lower water contents is due to the viscosity and structure of the IL as it changes with additional water, as well as the

differences in molecular structure of Zn-hexaaqua and $Zn(NTf_2)_2$. Just as in aqueous media, transport in IL systems involves the drift or diffusion of ions due to an applied electric field, where the positive and negative ions to be oxidized or reduced are separated at an average distance depending on concentration [72]. The difference arises from the structure of the ILs and how the redox active ions move past the ions in the IL or IL water mixture. In aqueous solvents, the H_2O molecules do not greatly hinder the movement of these charged redox active species, Figure 6.6a. However in the ILs, the space between the redox active species is filled with charged IL ions as well as empty space, or voids, that are produced by thermally generated local density fluctuations from being in the liquid phase, Figure 6.6b [72].

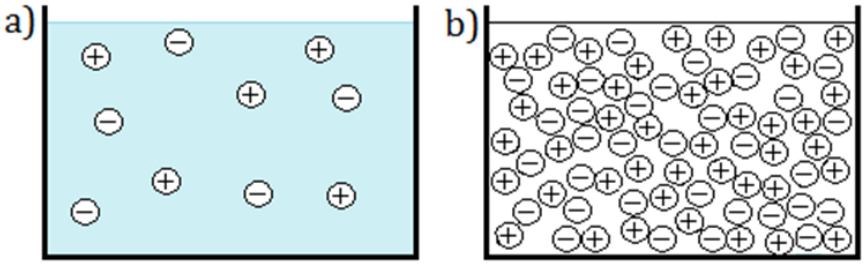

Figure 6.6: a) Charged ions in aqueous media, b) charged ions that make up an ionic liquid illustrating voids between ions. (Figure adapted from Bockris [72])

The diffusing species must move through these voids in order to reach the charged metal surface. These voids are both random in size and location and are constantly rearranging, growing and shrinking. The movement of voids can occur by the movement of an ion(s) into an already existing void, creating one in its

place. This phenomenon leads in to the concept of viscosity. The model of the kinetic theory of gases is analogous to the fluid motion in ILs, where the fluid in motion consists of layers parallel to the direction of the flow. The viscosity here is

$$\eta = 2nm\langle w\rangle\lambda, \tag{6.8}$$

where $<w>$ is the mean velocity of the particles normal to the fluid layer direction, λ is the mean free path, and n and m are the number per unit volume and mass of the particles respectively [72]. When particles (ions) jump from layer to layer, there is a momentum transfer causing viscous drag. Voids have apparent mass and momentum when they move between layers and also produce drag [72]. Comparing the $Zn(NTf_2)_2$ versus $[Zn(H_2O)_6]^{2+}$ diffusing in the IL provides insight into the structure of the IL and how the species must diffuse through it. $Zn(NTf_2)_2$ is a large complex and must rearrange more ions and voids to produce more space (compared to the space needed for the smaller complex of $[Zn(H_2O)_6]^{2+}$) in order to move through the IL. Therefore, movement of $Zn(NTf_2)_2$ yields more viscous drag and slower diffusion. Additionally, if $X_{H20}/X_{Zn} \geqq 6$, there is a large excess of water to mix with the IL, which can change the structure of the solution. Increasing H_2O can screen, or break up , the polar IL network, and with enough excess (> 75 mol%) a water micelle structure can form with distinct water-IL-water regions [73]. This significantly complicates arguments regarding how the ions rearrange to accommodate the diffusing Zn-ion species.

6.4.2 Kinetics: Butler-Volmer Analysis

Experimental analysis of the kinetics of Zn deposition is the subject of this section. First, it is necessary to give the definition of the parameter that describes rate of electron transfer, the exchange current density, i_0. At equilibrium, where there is zero overpotential, there exists balanced faradaic activity of i_a (anodic current) and i_c (cathodic current) where there is zero net current [53]. Any potentials positive this zero net current provides enough driving force to produce anodic currents, and vice verse for negative currents and cathodic currents. Values of exchange current density can vary widely and range from pA to A depending on the system. Small values of exchange current density correspond to sluggish kinetics and larger activation overpotentials for charge transfer. However, larger values of i_0 allow for very large currents at minimal overpotential.

Utilizing the RDE technique, and if the potential was held away from the diffusion limited regime, closer to the kinetically limited regime, then the intercept of the Koutecky-Levich corresponds to $1/i_K$. The current under purely kinetic limitation only

$$i_K = FAk_f(E)C_R^*, \tag{6.8}$$

allows for the determination of $k_f(E)$, the heterogeneous rate constant which directly relates to i_0, the exchange current density. The analysis to determine $k_f(E)$ was completed, however the data was not as expected giving spurious results. Therefore, kinetic analysis was alternatively done by fitting the Butler-Volmer equation to slow scan rate cyclic voltammetry [53]. The current at low

cathodic and anodic overpotentials, V < 50-100 mV, where the current is less than 10% of the limiting current and there are no mass transfer effects is fit to Equation 6.9,

$$i = i_0 \cdot \left(e^{\frac{-\alpha \cdot F}{R \cdot T}\eta} - e^{\frac{(1-\alpha) \cdot F}{R \cdot T}\eta} \right), \tag{6.9}$$

where α is the transfer coefficient, R is the gas constant and η is the overpotential, shown in Figure 6.7.

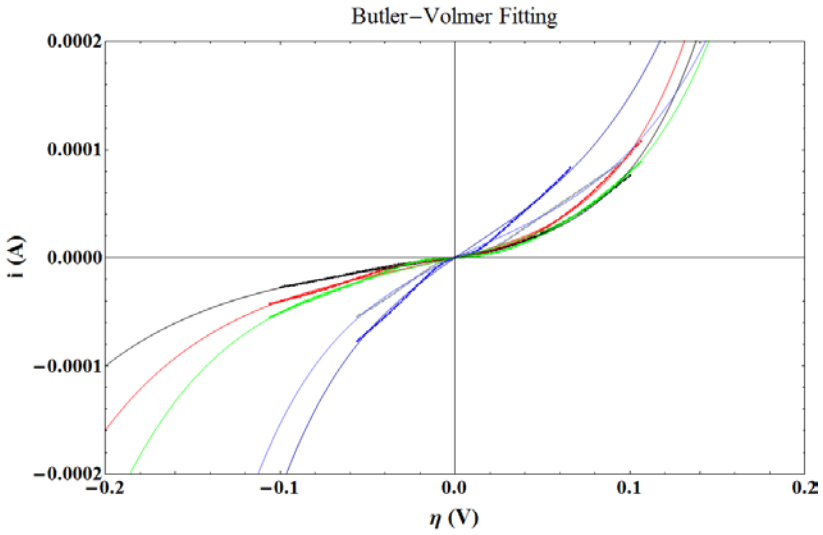

Figure 6.7: Fitting the cathodic and anodic branches of the 1 mV/s CV to the Butler-Volmer Equation 6.9 as a function of H_2O content. Black: 0.04 M, Red: 0.28 M, Green: 0.47 M, Light Blue: 0.67 M and Blue: 0.85 M H_2O..

The degree of inflection at η = 0 is proportional to the exchange current density. The water content was varied at 50°C, and held constant throughout the experiment with an overpressure of humid Ar at a relative humidity specified in

Figure 8.1a. A hysteresis in the voltammetry is seen in Figure 6.8a due to variation of Zn concentration at the surface.

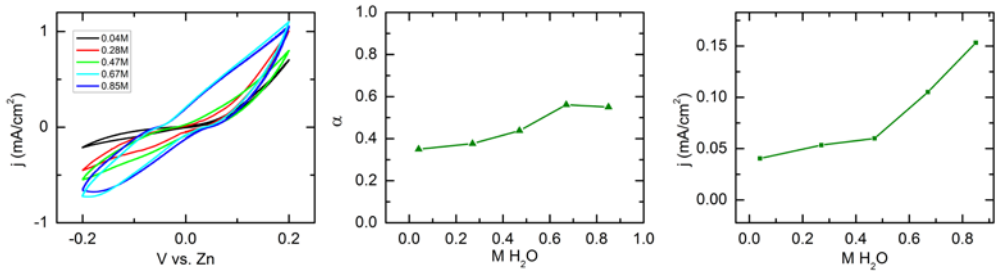

Figure 6.8: a) Cyclic voltammetry at varied H_2O concentrations. b) Transfer coefficient, α, and c) exchange current density, i_0, calculated by fitting to the Butler-Volmer equation..

This effect is more pronounced in the higher H_2O concentrations when the reduction and oxidation of Zn^{2+} is easier. To remove the hysteresis, the electrode was cycled until the voltammetry was at a steady state, or when the signal overlaid. The electrode was then allowed to sit in solution under open circuit conditions for 5 minutes to allow the system to come to rest, then scanned in the anodic direction for 50mV. This same procedure was repeated for the cathodic direction. Due to the lack of hysteresis, these scans were used to more accurately fit the Butler-Volmer equation and are shown in Figure 6.7. The transfer coefficient, α, is the measure of symmetry of the activation energy barrier for the reaction. The value of $\alpha = 0.5$ signifies a completely symmetric reaction. The experimental values of α center around 0.5, ranging from 0.56 to 0.39 (Figure 6.8b). At lower H_2O, it is observed that there is a larger barrier for Zn^{2+} reduction, whereas at higher H_2O the oxidation/reduction becomes symmetric and the

activation barrier for both is almost equal. The trend observed for the exchange current density as a function of H_2O concentration is shown in Figure 6.8c. Values range from 40-155 $\mu A/cm^2$, which 2-3 orders of magnitude smaller than values reported for 0.1 M $ZnCl_2$ in dilute aqueous acid at room temperature [70]. This indicates that the kinetics are much more sluggish, and that the activation overpotential is higher in this system for a particular current density. The reason for this trend is likely due to the solvation/complexation of Zn-hexaaqua or $Zn(NTf_2)_2$ as discussed in Chapter 6.3.4.

6.5 Conclusion

The voltammetry of in Zn electrodeposition in neat $[C_2nmm][NTf_2]$ on Pt showed a 5.5 V electrochemical window and redox peaks implying impurites from n-methylmorpholine. Zn redox was analyzed on both Cu{111} thin film and polished Zn disk substrates. The origins of overpotential were discussed in detail. Nucleation overpotential dominated on the Cu{111} substrate, whereas the diffusion overpotential is substrate independent. Diffusion of Zn to the surface of the electrode is greatly enhanced by the addition of water, which changes the complexation of the Zn from $Zn(NTf_2)_2$ to the hydrated $[Zn(H_2O)_6]^{2+}$, as well as changing the structure of the IL itself. Charge transfer overpotential was introduced in terms of binding energy of the Zn species. Marcus theory for electron transfer was explained in terms of electron tunneling, which may be highly influenced by the structure of the double layer. The solvent dynamic effects were also introduced, however, are not expected to play a large roll. The kinetics were measured by fitting the Butler-Volmer equation to slow scan rate CV, where higher water contents produced larger exchange current densities.

CHAPTER 7: ZN MORPHOLOGY

7.01 Introduction

A novel analysis of the overpotential dependence on morphology in the IL as a function of temperature, $Zn(NTf_2)_2$ concentration and overpotential. The morphology ranges from mossy growth with poor adherence to the substrate in the activation regime, dendritic growth in the diffusion limited regime, and nanocrystalline aggregates far into the diffusion limited regime. It is shown that at the higher overpotentials the ZnO may be forming from the presence of oxygen due to the breakdown of $[NTf_2]^-$. The nanocrystalline structures are analyzed using XRD to determine the crystal thickness. A comment on the cation effect on morphology is also provided.

7.1 Experimental

All Zn plating experiments were conducted in small volume (~1 mL) 3-electrode cells, unless otherwise specified. The experimental details are just as described in Chapter 6.1, where a Cu{111} thin film substrate was used as the working electrode. The water content was tested with a Karl Fischer titration method and was found to be < 400ppm H_2O for 0.1 M $Zn(NTf_2)_2$ solutions and < 10ppm H_2O for 0.01 M Zn solutions, though drying down further was difficult due to the hydrophilic nature of $Zn(NTf_2)_2$.

The Zn plating morphology was examined by x-ray-diffraction (XRD) using a Philips X'pert MPD diffractometer with a Cu K_α radiation source. The working

voltage and filament current was 45 kV and 40 mA, respectively. The phase identification was done referencing Joint Committee for Powder Diffraction Standard (JCPDS) database. Miller indices for hexagonal systems often utilize the 4-index scheme. The standard cubic (h k l) index becomes (h k i l), where a redundant index, $i = -h-k$, is used and can give more insight into the structure. However, for the following analysis, the standard 3-index scheme is sufficient for understanding the structure. Imaging was completed with an Hitachi s-4700 II Field Emission Scanning Electron Microscope at 15 kV accelerating voltage and 10 μA emission current.

7.2 Deposition Morphology at Low H_2O

7.2.1 Temperature Dependence

The morphology of electrodeposited Zn was evaluated on a Cu{111} thin film substrates at various overpotentials and temperatures. Conditions at -0.5 V at 50 °C and 70 °C, Figure 7.1a,c, yielded similar growths, however the kinetics are much slower in the 50 °C case shown by the CV in Figure 6.2.

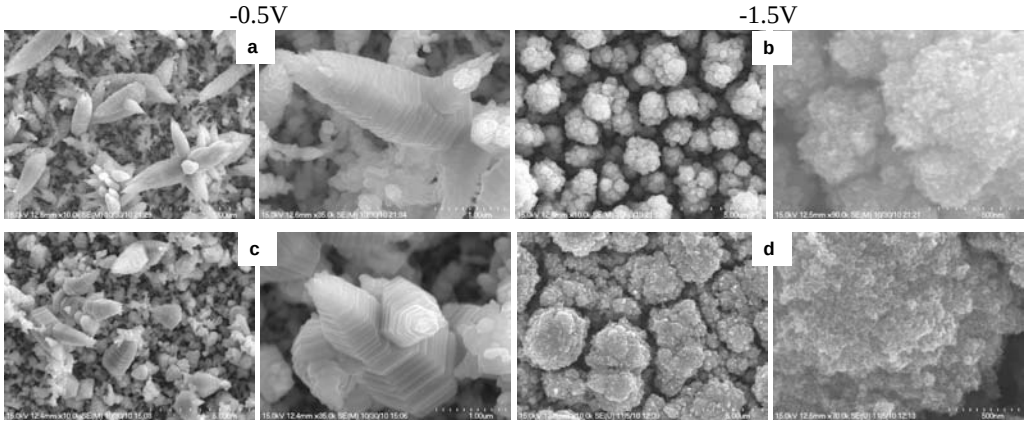

Figure 7.1: $[C_2nmm][NTf_2]$ + 0.1 M $Zn(NTf_2)_2$, Dry CA holds at -0.5 V and -1.5 V for 2 C/cm^2 at 50 °C (a,b) and 70 °C (c,d). Magnification varies from 10000x – 90000x.

This is also indicated by almost triple the time it takes to put down 2 C/cm^2 (Table 7.1). Both morphologies show dendritic hexagonal basal plane (002) plates of Zn.

Table 7.1: Deposition parameters for the samples shown in Figure 7.1.

	-0.5V	-1.5 V
50 °C (s)	13136	9774
mA/cm^2	-0.15	-0.172
70 °C (s)	5725	5588
mA/cm^2	-0.288	-0.354

The dendritic plates in the 50 °C case are less discrete, growing in “flowered” bunches with the tip of the dendrite growing longer and thinner perpendicular the (002 face). In the 70 °C case, the growths are broader at the base and grow

thicker, or more parallel to the (002) facet, producing shorter growths than in the 50 °C case. Increasing the deposition overpotential to 1.5 V (Figure 7.1b,d), yields aggregates of nanosized Zn (002) (2θ=36.29°) and (100) (2θ=38.99°) crystals as shown by XRD in Figure 7.2.

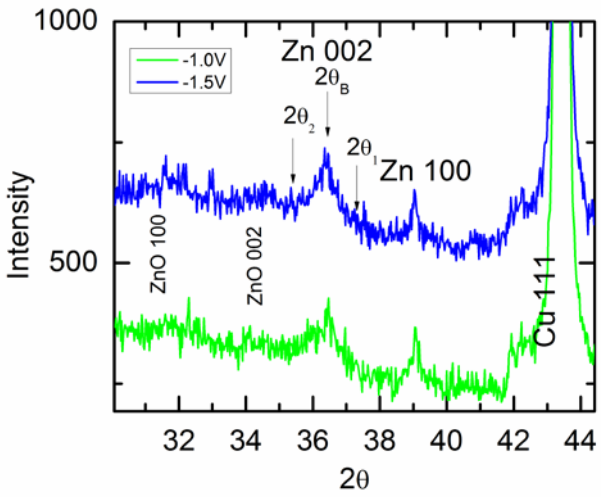

Figure 7.2: XRD of Zn deposition at 70 °C at -1.0 V and -1.5 V in $[C_2nmm][NTf_2]$ + 0.1M $Zn(NTf_2)_2$.

The 50 °C morphology aggregates in smaller more diffuse bunches, whereas the 70 °C morphology are much larger and packed in tighter. This brief analysis of temperature dependence has allowed us to choose 70 °C as the optimal temperature for continued analysis of overpotential and concentration dependence on the morphology. Further discussion of the mechanisms driving this morphology is provided below.

7.2.2 Overpotential and Concentration Dependence

A comparison of the morphology of Zn deposited from two concentrations, 0.1 M and 0.01 M $Zn(NTf_2)_2$ is shown in Figure 7.3, where dramatic changes in structure are revealed at fairly low overpotentials. The concentrations are compared with respect to similar morphologies and overpotentials, and Table 7.2 gives the average current density and deposition time at each overpotential.

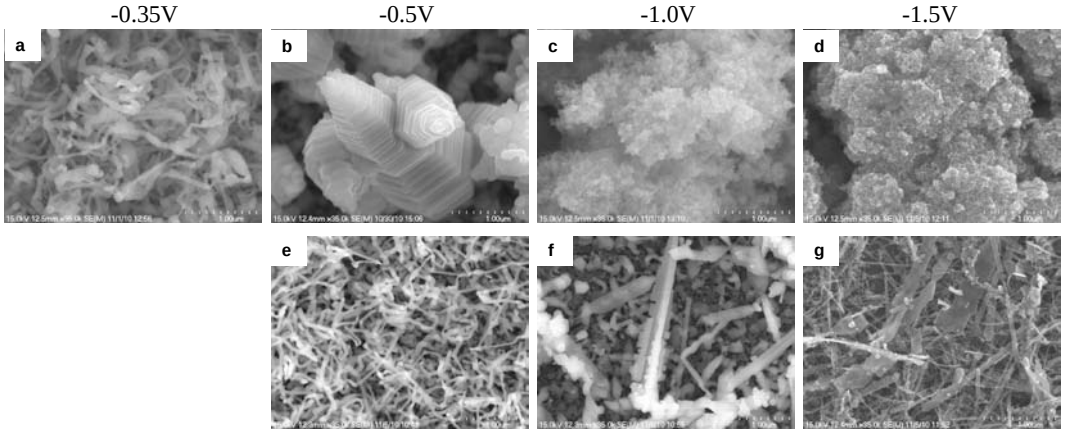

Figure 7.3:Deposition at 70 °C of Zn at various potentials in $[C_2nmm][NTf_2]$ + (a,b,c,d) 0.1 M $Zn(NTf_2)_2$ for 2 C/cm^2 and (e,f,g) 0.01 M $Zn(NTf_2)_2$ for 0.5 C/cm^2. All images are at 35000x magnification.

Table 7.2: Deposition parameters for the samples in Figure 7.3.

	-0.35 V	-0.5 V	-1.0 V	-1.5 V
0.1M:2 C/cm^2 (s)	5915	5725	5440	5588
mA/cm^2	-0.301	-0.315	-0.326	-0.3
0.01M:0.5 C/cm^2(s)	-	19530	15370	11360
mA/cm^2	-	-0.021	-0.028	-0.056

Low Overpotential

The morphology in the 0.1 M case widely varies over only 1.15 V from *a mossy* filament growth to dendritic then to an aggregate (Figure 7.3a-d). Deposition at -0.35 V results in a filament type growth, also known as spongy or mossy growth. This type of growth is also seen in aqueous alkaline zincate solutions and was observed as a black powder that does not adhere to the substrate, as is the case with the deposits obtained as well. Mossy growth occurs when in the purely activation limited regime, where the current produced by the overpotential provides only the activation energy needed to drive the reaction [53]. The exact mechanism for this, however, is still under debate [74-77]. Confirmed by the voltammetry in Figure 7.4, -0.35 V is in the kinetically limited activation regime and has not yet become diffusion limited.

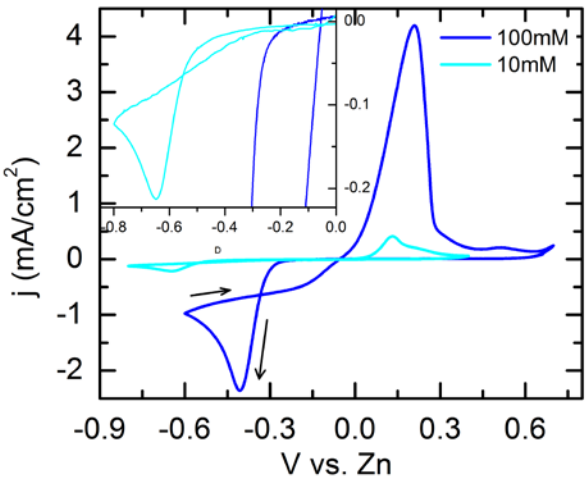

Figure 7.4: Cyclic Voltammetry 10 mV/s in $[C_2nmm][NTf_2]$ + 0.1/0.01 M $Zn(NTf_2)_2$ at 70 °C.

The XRD spectrum (Figure 7.5) indicates a highly crystalline mixture of both hexagonal (002) and (100) crystal directions present, as well as a Cu/Zn alloy phase formation. The alloy is a Cu 0.8 / Zn 0.2, corresponding to the α phase and will be discussed in detail in Chapter 9.3.2. There is no evidence of ZnO in the XRD or EDX.

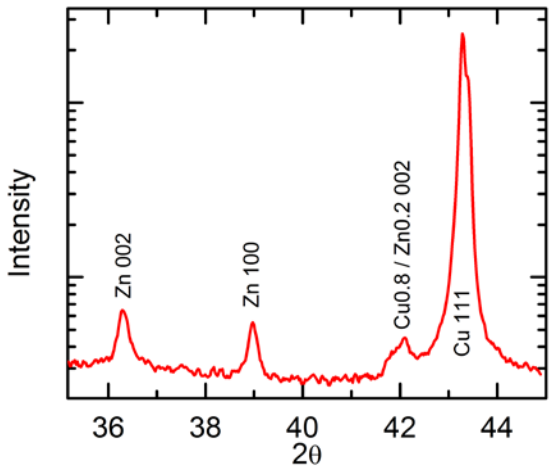

Figure 7.5: XRD of the Filament growth in Figure 7.3a.

At the 0.01M $Zn(NTf_2)_2$ concentration, a smaller charge density of 0.5 C/cm^2 was plated due to small current densities and long hold times necessary (Figure 7.3e-g). The same filament type growth observed with the 0.1 M $Zn(NTf_2)_2$ at -0.35 V overpotential is seen at an overpotential of -0.5 V, however the filaments are smaller in diameter. As seen from the CV in Figure 7.4, larger overpotentials are needed to deposit in the activated regime.

Diffusion Limited Deposition

When the system is driven harder into a regime that is both activation and diffusion limited, there is a mixture of dendritic and mossy growth. Dendritic growth becomes the primary morphology in a purely diffusion limited regime. Dendrites form when there is spherical diffusion to a point sink, the tip of the dendrite, rather than a planar sink which in effect creates higher current densities at the tip. This causes a lower overpotential, lower concentration gradient and possibly higher exchange current density at the tip causing it to grow faster than the rest of the substrate [54,75]. At -0.5 V, the 0.1 M $Zn(NTf_2)_2$ system becomes diffusion limited and produces dendritic growth of discrete basal plane plates. A similar type of growth is also seen by Thomas et al. [37] in aqueous 1 M $ZnCl_2$ at high current densities. Decreasing the concentration to 0.01 M $Zn(NTf_2)_2$ increases the overpotential to induce dendritic growth to -1 V. At that potential the system is well into the diffusion limited region, producing thin, needle-like dendrites with an average diameter of 30 nm at the base.

Large Overpotentials

Moving now to overpotentials much further into the diffusion limited regime, it is seen at 0.1 M $Zn(NTf_2)_2$ and overpotentials of -1 V and -1.5 V, the system produces aggregates of nano-sized Zn (002) and (100) crystals evidenced by small peaks in the XRD spectra, Figure 7.2. There are also small peaks at a 2θ of 31.77 and 34.43 which may corresponds to hexagonal (002) and (100) ZnO facets respectively. Energy-dispersive X-ray Spectrometry (EDX) also measures an

increase in oxygen concentration. The small equilibrium concentration of water in the system could be contributing to the formation of ZnO at the higher overpotentials. It is also possible however, that with only 400 ppm H_2O present in the system, more oxygen is needed to produce significant ZnO growth. MacFarlane and coworkers observed that in $[NTf_2]^-$ based ILs, the $[NTf_2]^-$ begins to break down at -2.7 V versus Zn on a Pt electrode in a fully dry electrolyte [78]. The presence of H_2O decreases the potential for $[NTf_2]^-$ breakdown, and with an increase of only 50 ppm H_2O the breakdown potential becomes more anodic by +300 mV. With 400 ppm H_2O present in the 0.1 M $Zn(NTF_2)_2$ solution, the potential for $[NTf_2]^-$ breakdown could become even more anodic, further aiding in the formation of ZnO. Analyzing the aggregates even further yields an average crystal size at high overpotentials is in the range of 30-60 nm from SEM images, however it is difficult to precisely discern. By using XRD spectra, the crystal thickness can be calculated using Scherrer's formula,

$$t = \frac{0.9\lambda}{B\cos 2\theta_B}, \tag{7.1}$$

to determine the crystal thickness, t [79]. The x-ray wavelength,

$$\lambda = 2d\sin\theta_B, \tag{7.2}$$

must be calculated using values for interplanar spacing, d, and Bragg angle, θ_B, as noted on Figure 7.2.

$$B = \frac{1}{2}(2\theta_1 - 2\theta_2) \tag{7.3}$$

The width, *B*, of the diffraction curve, also termed the Full Width-Half Maximum, is calculated using value of θ_1 and θ_2 also labeled on Figure 7.2. Calculations yield a (002) crystallite thicknesses of 4.25 nm and 5.5 nm, and (100) thicknesses of 19.4 nm and 27.7 nm for the -1.0 V and -1.5 V deposition potentials respectively. A trend is therefore observed wherein a higher overpotential produces larger crystallites.

Increasing the overpotential to -1.5 V with the 0.01 M $Zn(NTf_2)_2$ solution produces a different kind of Zn filament with an average diameter of 10-15 nm, intertwined within long nanometer-thin plates of Zn. There is no evidence of ZnO in the XRD spectrum of this morphology. The EDX detected a slight increase in oxygen signal and it is possible that ZnO is present; however, the coverage is very small and is close to the detection limit. The low concentration of Zn also translates to lower H_2O concentration (< 10 ppm) shifts the $[NTf_2]^-$ breakdown to a more cathodic potential [78]. Further study through analysis at higher charge densities in order to achieve a better XRD signal to noise ratio may clarify this issue. Also, deposition at more negative overpotentials as discussed with the 0.1 M $Zn(NTf_2)_2$ system deeper into the $[NTf_2]^-$ breakdown region to see an increase in ZnO signal may add value.

7.3 Adsorption Effect

As a further comment on the morphology evolution in described above, it is possible that these effects are also being influenced by adsorption of the cation at

varying potentials discussed in Chapter 6.3.4. If the surface is screened by a large cation ring it may increase the difficulty to both reduce and oxidize Zn^{2+}. Previous work by Endres and coworkers deposited Al from $[C_4mpy][NTf_2]$ yielding nanocyrstalline deposits as well as poor redox behavior on stripping. Deposition with a different cation, ethyl-methylimidizolium, $[EMIm][NTf_2]$ showed excellent microcrystalline deposits and reversible deposition and stripping. This result was attributed to stronger adsorbtion of the $[C_4mpy]$ on the surface that hinders both redox processes. It may be interesting to continue work with different cations to determine if there are differences in the Zn morphology, as well as with cation mixtures to characterize the evolution with different concentrations.

7.4 Conclusion

Dependence of morphology on temperature, $Zn(NTf_2)_2$ concentration and overpotential was shown. At low overpotentials, in the activation limited regime, both Zn concentrations yielded mossy growth. In the diffusion limited regime, dendritic growth dominated. At even higher overpotentials, aggregates of nanocrystalline Zn were formed in the 0.1 M $Zn(NTf_2)_2$ solution, with the possible formation of ZnO due to the breakdown of the $[NTf_2]^-$. Comments on possible effects of cation adsorption were discussed with ideas on changing the IL cation to look at the effect it would have on the morphology.

CHAPTER 8 H_2O EFFECT ON ZN MORPHOLOGY

8.01 Introduction

The following chapter outlines the morphological effects of humidity on the water content under various conditions. The kinetics and diffusion of Zn species greatly increases as more water is introduced into the system as shown in Chapter 6.4, which in turn yields better Zn deposits. The lower overpotentials also yield better morphologies as hydrogen evolution plays a large role in causing defected structures at greater overpotentials. Systems that tend to produce the (100) type facet are also more likely to show dendritic or abnormal growths. This fact has lead to refining conditions around systems with a majority of the planar (002) facets. With high Zn and high water contents (55 – 70 mol%), high charge density deposits are obtained. A difference in only 4 M H_2O gives morphologies where the faceting is either mainly (002) for 9 M H_2O or (100) for 5 M H_2O. Since the structure of IL is dramatically changing with increasing water contents, comments on how that may be affecting the morphology are also given.

8.1 Experimental

All Zn plating experiments were conducted in small volume (~1 mL) 3-electrode cells, unless otherwise specified. The experimental details are just as described in Chapter 6.1, where a Cu{111} thin film substrate was used as the working electrode. The water contents were controlled in the solutions by bubbling with mixtures of humidified and dry Ar and measured by a hygrometer. By changing the ratios of these mixtures, the water content could be precisely maintained. An

overpressure of humidified gas was used in order to maintain the water content during the experiment.. The water content was tested with a Karl Fischer (KF) titration method. Again, The Zn plating morphology was examined by XRD, SEM and EDX with details regarding their operation in Chapter 7.

8.2 Viscosity and Relative Humidity

The addition of H_2O into the system is of interest to further analyze the differences in Zn complexation / hydration, and is directly applicable to Zn-Air batteries where operation under ambient air/moisture conditions is necessary. Water content as a function of relative humidity in the 0.1 M $Zn(NTf_2)_2$ solution is shown in Figure 8.1a.

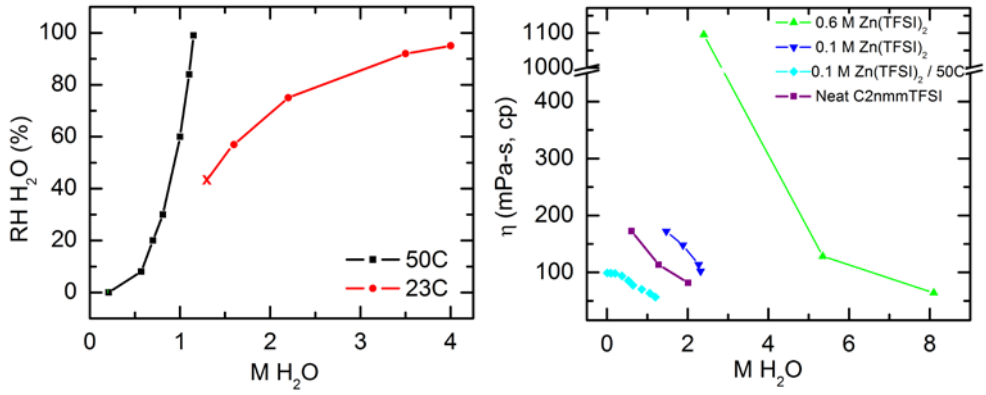

Figure 8.1: Water content as a function of relative humidity in $[C_2nmm][NTf_2]$ at 23 °C and 50 °C. At less than 1.2 M H_2O the solution has a melting temperature above 23 °C. b) Viscosity as a function of H_2O content in $[C_2nmm][NTf_2]$ with varying Zn concentrations from 0.1-0.6 M $Zn(NTf_2)_2$.

The black line corresponds to the solution at 50 °C, reaching a maximum water content of 1.2 M H_2O at 100% humidity. At 23 °C, without water present, [C_2nmm][NTf_2] has a melting temperature of 29.2 °C [46]. However, if there is enough water present, the melting temperature is reduced. When the water content is greater than 1.2 M (red line), the solution is liquid at room temperature and Zn deposition is possible. Knowing the viscosity of these solutions is extremely valuable because, as discussed previously in Chapter 6.4, the diffusion of the each Zn species is dependant on these values. Figure 8.1b plots viscosity in mPa-s versus M H_2O present in the IL. The neat [C_2nmm][NTf_2] itself is rather hydrophilic, and at room temperature and high water contents, its viscosity ranges from 90-180 mPa-s. At the same water contents, the addition of 0.1 M $Zn(NTf_2)_2$ increases the viscosity. Further increasing the $Zn(NTf_2)_2$ concentration to 0.6 M causes huge increases in viscosity at lower concentrations of H_2O to greater than 1000 mPa-s. With significantly more H_2O, X_{H2O} > 5 M, the viscosity decreases an order of magnitude to similar values of the neat and 0.1 M $Zn(NTf_2)_2$.

8.3 Zn Deposition Morphology at 50°C

Zn deposition with 0.1 M $Zn(NTf_2)_2$ containing 0.9 M H_2O was investigated at overpotentials of -0.1 V to -0.4 V at 50 °C (Figure 8.2, Table 8.1).

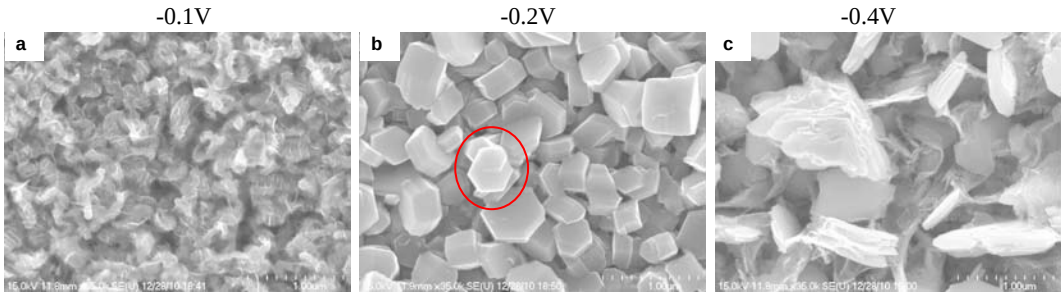

Figure 8.2: Zn Deposition at -0.1- 0.4 V at 50 °C at 0.9 M H_2O contents. Images a,b are at 35k and images e is at 10k. The red circle denotes a growth spiral.

Table 8.1 Deposition parameters for the samples in Figure 8.2.

	-0.1 V	-0.2 V	-0.4 V
0.9 M H_2O (s)	3273	2929	2306
mA/cm^2	-0.291	-0.308	-0.376 –› -0.5

The voltammetry in Figure 6.3 suggests higher exchange current densities for the higher H_2O contents, as well as higher diffusion values, which affect the morphology. At -0.1 V at signs of filament growth associated with deposition in the purely activated regime along with distinct crystallites are seen [74-77]. Small, wispy type growths developed all over the crystals, due to a competition between hydrogen evolution from the higher H_2O content and Zn deposition at such a low overpotential. At an overpotential of -0.2 V, the morphology becomes much more clearly faceted with both (200) and (100) planes verified by XRD, Figure 8.3.

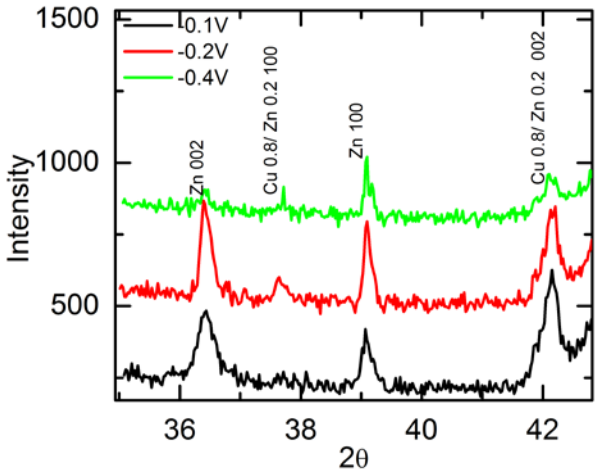

Figure 8.3: XRD in $[C_2nmm][NTf_2]$ + 0.1 M $Zn(NTf_2)_2$+ 0.9 M H_2O at 50 °C varying potential. -0.1 V (black), -0.2 V (red) and -0.4 V (green) corresponding to morphology in Figure 8.2.

At the center of Figure 8.2b, a growth spiral is clearly seen. This type of smooth growth starts from the interior of the facet and grows outward producing a flat surface. The rate of growth is determined by step height (lattice spacing), step separation (critical radius of 2-dimensional nucleation) and rate of the advancing step (free energy and driving force of the step edge) [80]. Increasing the overpotential to -0.4 V produces (100) type defected dendritic growth, suggesting that this non basal plane facet is more likely to produce dendrites. Potentials more cathodic of -0.4 V yield run-away dendrites due to bulk hydrogen evolution, which have poor adhesion to the substrate and fall off the sample during removal from the solution. At these low Zn charge densities, the XRD also detected peaks at 37.85 and 42.05 corresponding to a hexagonal Cu 0.8 / Zn 0.2 alloy. The relative peak intensities suggest a possible potential dependence on the formation

of alloy crystal planes. Furthermore, -0.4 V, the intensities for both alloy facets decrease due to decreased coverage of Zn on Cu. During dendritic growth, the majority of Zn is deposited perpendicular to the substrate causing less coverage of Zn on the surface, in turn, yielding less Zn to diffuse into the Cu. More discussion on the Cu / Zn alloying will be will be explored in Chapter 9.3.2.

8.4 Zn Deposition Morphology at 23°C

The morphology was also examined at very high water contents where the IL is liquid at room temperature. A drastic change in morphology is seen with only 0.1 V difference in potential. By first examining the voltammetry of the two water contents in Figure 8.4a, differences in overpotential and kinetics at two water contents, 1.7 M and 2.9 M H_2O are clearly visible.

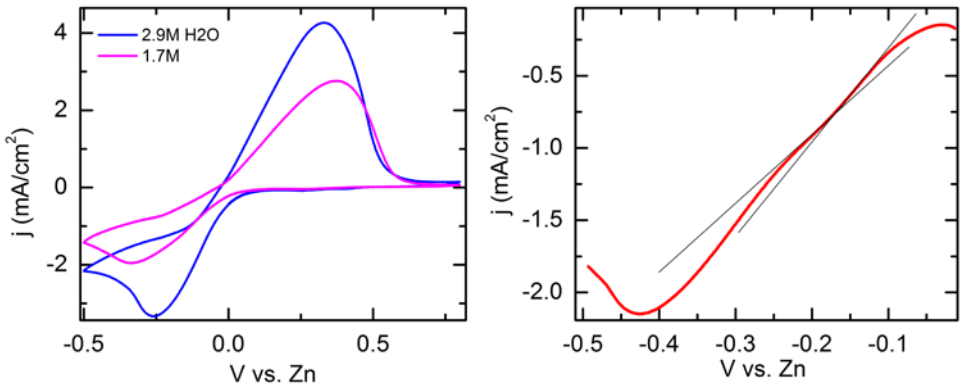

Figure 8.4: Cyclic voltammetry at 50 mV/s at 23 °C with 0.1 M $Zn(NTf_2)_2$ a) varying water content and b) first cathodic sweep showing a change in slope at in the activation region, 50 mV/s.

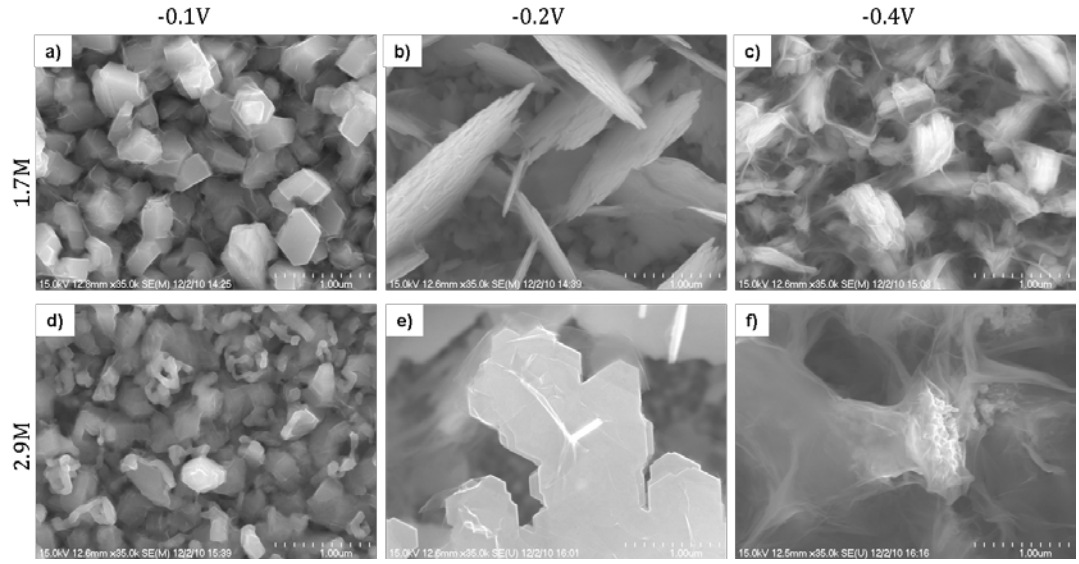

Figure 8.5: Zn morphology in $[C_2nmm][NTf_2]$ +0.1 M $Zn(NTf_2)_2$ at 23 °C at varying potentials up to 1 C/cm^2 with a,b,c) 1.7 M and d,e,f) 2.9 M H_2O.

Table 8.2: Deposition parameters for the morphologies shown in Figure 8.5.

	-0.1 V	-0.2 V	-0.4 V
1.7 M H_2O (s)	9940	6380	5280
mA/cm^2	-0.1	-0.151	-0.227 (-0.17)
2.9 M H_2O (s)	3960	3287	2265
mA/cm^2	-0.24	-0.352	-0.495

Growth at -0.1 V (Figure 8.5a) with 1.7 M Zn yields a mixture of hexagonal (002) and (100) crystal facets measured by XRD in Figure 8.6. Increasing the overpotential to -0.2 V changes the morphology to solely (100) crystal facets

(Figure 8.5b), producing “run-away” plate growth perpendicular to the sample surface approximately 20-50 nm wide.

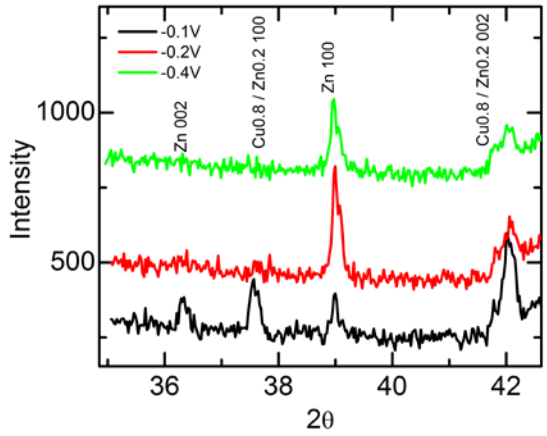

Figure 8.6: XRD in $[C_2nmm][NTf_2]$ +0.1 M $Zn(NTf_2)_2$+ 1.7 M H_2O at 23 °C corresponding to the growth morphology seen in Figure 8.5a,b,c.

To understand why there is such a large change in deposit morphology, a plot of the first cathodic scan into the Zn deposition region on the Cu {111} thin film electrode is shown in Figure 8.4b. There is a clear change in slope between -0.1 V and -0.2 V, possibly signifying a change in mechanism for Zn deposition producing the change in facet growth. In most cases, this slope change is hard to discern after the first scan on Cu. One possibility for this change in mechanism is the change adsorption of the cation with increased water. With higher water contents, the IL is increasingly screened [73], which could produce the growth observed. Increasing the potential to -0.4 V (Figure 8.5c) into the diffusion limited region retains the (100) facet, however, the structure is highly defected due to a significant amount of hydrogen evolution at these high H_2O contents.

Increasing the water content to 2.9 M produces similar morphology to that of the 1.7 M H_2O. The growth at -0.1 V produces smaller crystals, and more of the filament type growth that seen in the activation regime. Figure 8.5e shows the morphology at -0.2 V, which generates flat "dendrite-looking" (100) facets. At -0.4 V, there is more of the (100) facet that remained in the 1.7 M H_2O, however it is much more defected due to increased hydrogen evolution with higher H_2O.

8.5 High Zn Deposition Morphology

The effect of high Zn concentration on morphology is of great interest. For high storage applications such as electric vehicles, the ability to attain high charge and current densities is necessary. The solubility of $Zn(NTf_2)_2$ in $[C_2nmm][NTf_2]$ is approximately 0.7 M, so 0.6 M was chosen as the high Zn concentration. $Zn(NTf_2)_2$ is tremendously hydrophilic, demonstrated by IL solutions containing 0.1 M $Zn(NTf_2)_2$ which cannot be dried using Ar bubbling at 70 °C in a dry glove box beyond 0.03 M H_2O (X_{H2O}/X_{Zn}=1.3). With 0.6 M $Zn(NTf_2)_2$, the equilibrium H_2O concentration at room temperature under dry Ar is approximately 2.5M (X_{H2O}/X_{Zn}=4.2), resulting in an large increase in viscosity to 1100 mPa-s. The CV at 3.8 M H_2O, Figure 8.7, shows a larger overpotential for Zn deposition as well as much slower kinetics and rates of diffusion.

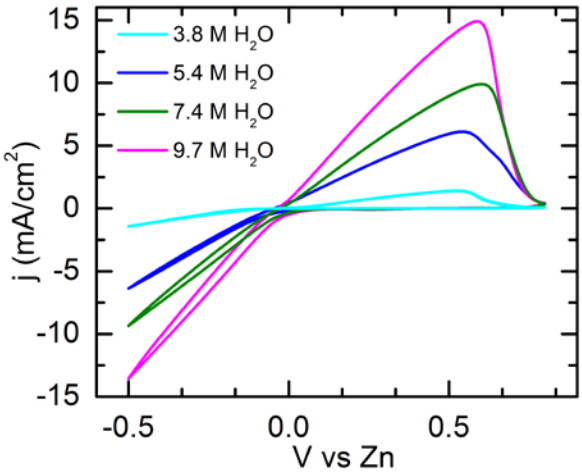

Figure 8.7: Cyclic voltammetry of $[C_2nmm][NTf_2]$ + 0.6 M $Zn(NTf_2)_2$ varying H_2O content from 3.8-9.7 M.

This is attributed to both the $Zn/H_2O/NTf_2$ complexation/hydration discussed in the previous sections, which also produces the increase in viscosity in the system because at low H_2O contents, movement of a mixture of both species $Zn(NTf_2)_2$ and $[Zn(H_2O)_6]^{2+}$ in a nearly saturated $Zn(NTf_2)_2$ solution is very difficult. As discussed in Chapter 6.4, diffusion of species in ionic liquids is dependant on the movement and rearrangement of ions and voids within the IL structure. The addition of 0.6 M Zn into solution has increased the viscous drag of the diffusing species and slowed diffusion to the surface. This, in turn, decreases the current density, deleteriously affecting the growth morphology, shown in Figure 8.8a.

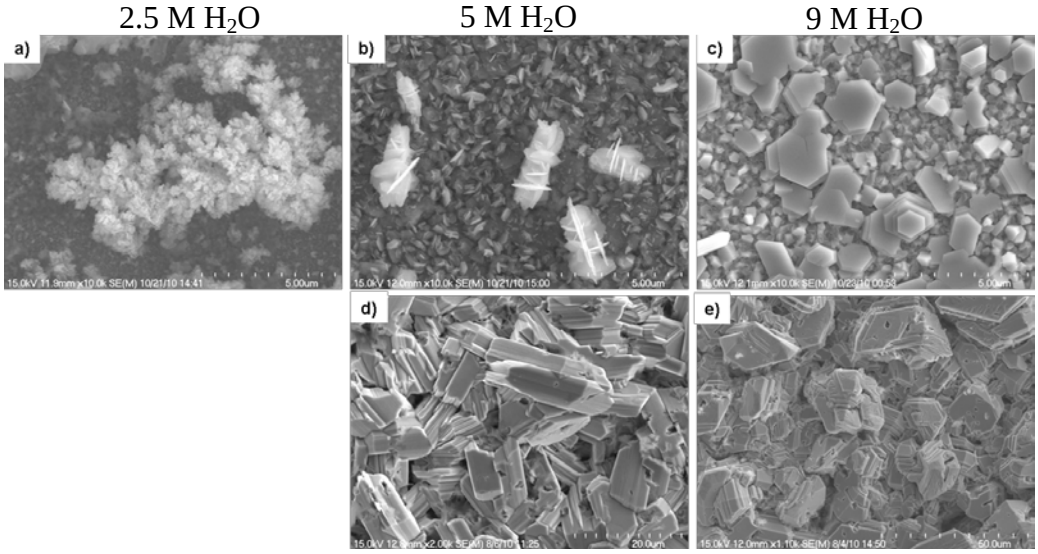

Figure 8.8: $[C_2nmm][NTf_2]$ + 0.6 M $Zn(NTf_2)_2$ deposited chronopotentiometrically at -3 mA/cm^2 varying H_2O concentrations at a,b,c) 1 C/cm^2 and d,e) 100 C/cm^2.

Table 8.3: Deposition parameters for the deposits shown in Figure 8.8.

	2.5 M	5 M	9 M
1C/cm^2: (V)	-1.9 –› -3	-0.32 –› -0.54	-0.21
100C/cm^2: (V)		-0.2	-0.12

At 2.5 M H_2O and -3mA/cm^2, the morphology is very dendritic, with the deposit falling off the sample when removed from the solution due to poor adhesion. The solution could not support the current density, with the potential starting at -1.9 V, and dropping to -3 V at the end of depositing 1C/cm^2 charge (Table 8.3). Upon increasing the H_2O concentration to 5 M (X_{H2O}/X_{Zn}=8), the Zn is entirely hexaaqua, and the viscosity has decreased by an order of magnitude to 130 mPa-s.

The current density in Figure 8.7 has also increased for the 5 M H_2O system, owing to a greater ease of diffusion of the completely hydrated $[Zn(H_2O)_6]^{2+}$ species. However, the diffusion limited regime of Zn^{2+} is not clearly distinguished in the CV due to competing bulk hydrogen evolution at increasingly cathodic potentials. The morphology at a current density of -3 mA/cm^2 and two charge densities of 1 C/cm^2 and 100 C/cm^2 are shown in Figure 8.8b and d, respectively. XRD, Figure 8.9, of this growth indicates primarily non-basal plane (100) and (110) crystal faceting.

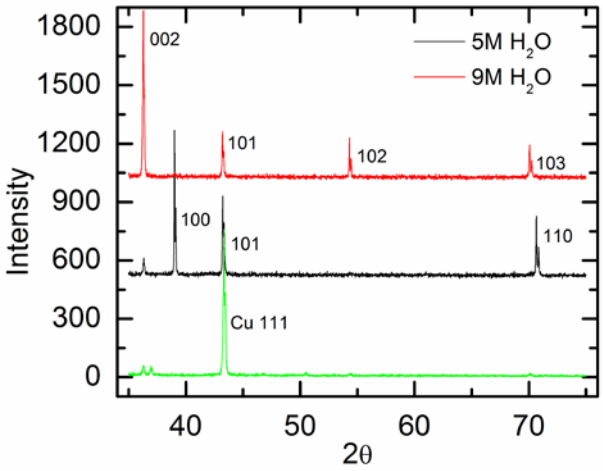

Figure 8.9: XRD on $[C_2nmm][NTf_2]$ + 0.6 M $Zn(NTf_2)_2$ + 5/9 M H_2O.

If the H_2O content is increased again to 9 M (X_{H2O}/X_{Zn}=15), there is a significant excess of H_2O, decreasing the viscosity even further to 65 mPa-s. The Zn^{2+} is still fully hydrated, though now diffusion to the surface is in a more dilute mixture of IL producing even higher current densities (Figure 8.7). The morphology at the same current charge densities as the 5 M system are shown in Figure 8.8c and e,

respectively. However, the growth for this morphology, Figure 8.9, yields facets of primarily basal plane (002) with minor signal from (102) and (103) facets as well. Surprisingly, a change in H_2O content of only 4 M has a strong effect on the growth kinetics of this system. It is seen that the (100) facet is more likely to form dendrites in the lower water systems, therefore understanding the mechanism for this type of growth can lend insights into avoiding it.

Various authors have shown various electrodeposition conditions and additives effect the developing Zn morphology [77,81-83]. The adsorption of the additives can cause the preferential growth of a particular facet. In the case of 5M and 9M H_2O, the IL is as acting like an additive, with adsorption of the cation on the surface of the electrode strongly effecting the growth. Alternatively, the layered structure of the double layer is changing significantly with these high water contents and may also be causing the differences [63]. Molar concentrations of 5 M and 9 M H_2O correspond to 55 mol% and 69 mol% H_2O in the system, respectively. Jiang and coworkers found increasing water content breaks up the IL structure and that at 75 – 80 mol% H_2O a micelle structure forms with distinctly separate IL-water regions [73]. This variation of IL-water structure may be greatly affecting the facet evolution through different adsorption processes. For example, at 55 mol%, more adsorption (or the orientation) of the C_2nmm cation could be causing the (100) facet to preferentially form, where as less adsorption could lead to the more planar (002) facet forming.

Looking now to the mechanisms for preferential faceting, it is known that the rate of electrogrowth on each crystal face is different and is attributed to the interface, growth mechanism and driving force [80]. This is attributed to ad-atom bond energy onto the crystal planes. Stronger bonding and fast charge transfer occurs when there is a large number of atoms on the crystal plane that are connected to the Zn depositing cation. The growth rate is also dependant on the work function of the specific planes and is related to the ease of electron tunneling to the depositing cation which in turn effects the charge transfer [54]. The result of this growth rate dependence on crystal faces is that the faster growing crystal facets disappear, whereas the slower growing facets dominate the structure. At 5 M H_2O, the slowest growing facet is primarily the (100) and (110) planes and at 9 M H_2O the (002) basal plane has the slowest growth rate. This result is remarkable and warrants further investigation through the completion of surface stress measurements as a function of H_2O concentration with high Zn in Chapter 9.

8.6 Conclusion

Faster kinetics and diffusion characteristics in the presence of water provide much better Zn deposits. The best deposit morphologies are found at low overpotentials. Conditions that produce a majority of (100) faceting are more likely to produce dendrites or abnormal plate growth. Avoiding these conditions, planar highly faceted (002) basal plane growth are obtained. High Zn, high water IL mixture systems can produce very planar (002) faceting at high charge densities.

CHAPTER 9 SURFACE STRESS

9.01 Introduction

In-situ electrochemical surface stress experiments were completed during growth of Zn on thin film Cu {111} substrates in $[C_2nmm][NTf_2]$, giving insight into possible mechanisms for specific morphological evolution. Mechanisms for stress development are described, including alloy formation and strain relaxation through flow of misfit dislocations. Compressive stress at higher charges may be generated by a chemical potential difference between the surface and grain boundaries producing a driving force for the flux of atoms into the grain boundaries. Grain size is a factor in the magnitude of stress generated, where a larger grain size produces less compressive stresses. The type of faceting that develops also has an effect on the stress response, with lower surface energy orientations in the grain boundaries generating smaller stresses. An in-depth look into the Cu/Zn α-brass alloy is also shown, where large tensile stresses develop upon dealloying.

9.1 Background

Deposition of thin films by any technique, vacuum or electrochemical, produces intrinsic stresses that may exceed the tensile strength of the depositing material itself [84]. These stresses can lead to film failure through cracking, peeling and deleterious physical properties such as electromigration. A tremendous amount of research has been done to determine the causes of these stresses, and ultimately find ways to grow low-stress films. In the microelectronics industry, stresses

generated in electrodeposition of thin Cu films via the damascene process aversely impact device reliability [85,86]. Additives are used to modify the morphology via surface adsorption during deposition and impact the stress response, creating uniform films. In vacuum, the most common thin film growth mode is Volmer-Weber (VW) where each stage of growth is accompanied by a stress response. Nucleation, island coalescence, and continuous film growth are correlated to compressive, tensile and compressive stress evolution respectively for metallic film growth on amorphous substrates [84,87,88]. For polycrystalline substrates the stress response is system dependant [84]. Other stresses can also develop in films due to factors such as heteroepitaxy, grain size and hydrogen incorporation though H is not a factor in vacuum deposition, it must be considered when in electrochemical aqueous environments [89-92].

The following work focuses on electrodeposition of Zn in the ionic liquid, N-ethyl-N-methylmorpholinium bis(trifluoromethanesulfonyl)imide, $[C_2nmm][NTf_2]$, in the presence of water generated by varying the humidity level. The effect of humidity level (water concentration) on morphology and consequently internal stresses induced in the films up to 10μm thick is studied. The stress induced by Zn cycling is also discussed, specifically with respect to the Cu/Zn alloying and dealloying behavior. The stresses were measured by a direct cantilever curvature technique. This high resolution, real time stress monitoring technique has been previously used in both ultra-high vacuum and electrochemical environments [93-101]. This stress measurement method monitors

the stress induced sample curvature, which is then converted to a stress-thickness product through the Stoney Relation

$$\Delta f = \Delta(\sigma_f \cdot t_f) = \frac{E_s t_s^2}{6(1-\nu_s)} \Delta\kappa, \tag{9.1}$$

where σ_f and t_f are the stress and thickness of the film, E_s , t_s, and ν_s are the elastic modulus, thickness, and Poisson's ratio of the substrate, and κ is the measured curvature [102,103].

9.2 Experimental

9.2.1 Surface Stress Technique

The in situ electrochemical stress monitoring cell utilizes a cantilever curvature technique that measures the deflection of the cantilever via a capacitive sensor allowing for subnanometer sensitivity and >1kHz time base resolution [93-96]. Previous stress measurement cells utilized a monolithic design in order to significantly reduce drift and sample placement error [96]. However, the cell design was modified to decrease the electrolyte volume. This was done by designing a split-small cavity cell, which is comprised of two separate PEEK blocks, where a cross sectional view is shown in Figure 9.1. The cantilever is then clamped near its bottom between the two blocks and held in place by compressing an o-ring. The o-ring extends to the full height of the PEEK blocks in order to seal the cell for the small electrolyte cavity which holds 6 mL of solution. The new cell configuration holds both the capacitance sensor and vertically oriented cantilevered electrode in the same way the large volume cell, Figure 9.1a. To

make contact with the working electrode, a gold contact pin was integrated into the PEEK cell at the o-ring compression point. The contact to the capacitance sensing electrode was made by fixing a stainless steel contact wire to the corner of the electrode with silver paint covered by chemically inert enamel, Figure 9.1b.

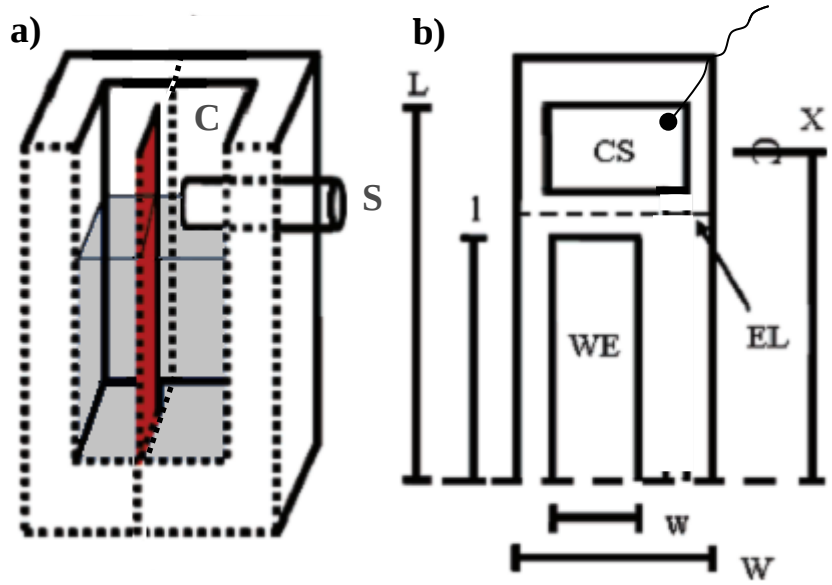

Figure 9.1: a) Cross Section of the split-small cavity cell where C, S and E denote the cantilever, sensor and electrolyte, respectively. b) Cu {111} patterned electrode defining the capacitive sense (CS), the working electrode (WE) and the electrolyte level (C). The sample geometry is shown as *W*, *w*, *L*, *l*, and *X*. Figure adapted from Heaton and Friesen [96].

Since the sample holder, cell, and detector are in a single unit, calibration is performed by simply orienting the cell so that the cantilever is normal to +/- Earth's gravitational field. A mathematical relation for surface stress per change in output voltage was derived in terms of the geometry and mechanics of the

cantilever deflection [104,105]. That deflection is related to the output voltage of the capacitive sensor given by

$$\frac{\Delta f \cdot h_f}{\Delta V} = \left(\frac{W}{w}\right)\left(\frac{\rho_s \cdot a_g}{6(1-\nu)}\right)\left(\frac{X^2(6L^2 - 4LX + X^2)}{l^2/2 + l(X-l)}\right)\left(\frac{1}{\Delta V_{tot}}\right), \tag{9.2}$$

where ΔV_{tot} is the stress voltage, ρ_s is the substrate density, a_g is the gravitational constant, ν is poisson's ratio and *W*, *w*, *X*, *L*, and *l* are defined by the sample geometry shown in Figure 9.1b. This technique removes the elastic moduli of the cantilever and a squared term in cantilever thickness from the relation between curvature and film stress, both of which are significant sources of error in wafer curvature measurements. All surface stress measurements presented here are reported as a stress-thickness in units of N/m.

9.2.2 Electrochemistry

The PEEK electrochemical cell was cleaned by rinsing with dilute sulfuric acid and rinsed in 18 MΩ-cm water. A high surface area Zn foil was used as a counter electrode and was placed parallel to the cantilever working electrode. A polished 1mm Zn wire was used as a pseudo-reference electrode. The working, reference and counter electrodes were placed in the cell prior to the loading of the electrolyte. The cantilever samples used during stress monitoring experiments consisted of a 160 μm thick, acid cleaned borosilicate glass substrate and patterned Cu{111} films (Figure 9.1b). DC magnetron sputtering was used to deposit a 1 nm Cr adhesion layer followed by 500 nm of Cu. A custom hard-mask was used to pattern the film creating a working electrode surface area of 2

cm^2. For all stress experiments, solutions of $[C_2nmm][NTf_2]$ + 0.6 M $Zn(NTf_2)_2$. The humidity level was controlled by bubbling with varying mixtures of dry and humidified Ar gas and measured via a hygrometer. Humidity levels of 60% and 90% yielded solutions of $[C_2nmm][NTf_2]$ with 5M and 9M H_2O with corresponding viscosities of 130 mPa-s and 65 mPa-s, respectively. For each experiment, a new cantilever was used and the IL was deaerated with mixtures of humidified (18 MΩ-cm water) and dry high purity Argon gas to remove all oxygen and maintain the desired H_2O concentration. The humidity level was measured with a hygrometer.

9.3 Results and Discussion

9.3.1 Zn Electrodeposition

The Cu{111} thin film was held chronopotentiometrically at -1mA/cm^2 up to 1C/cm^2. The stress response for two H_2O concentrations, 5 M and 9 M H_2O are shown in Figure 9.2a.

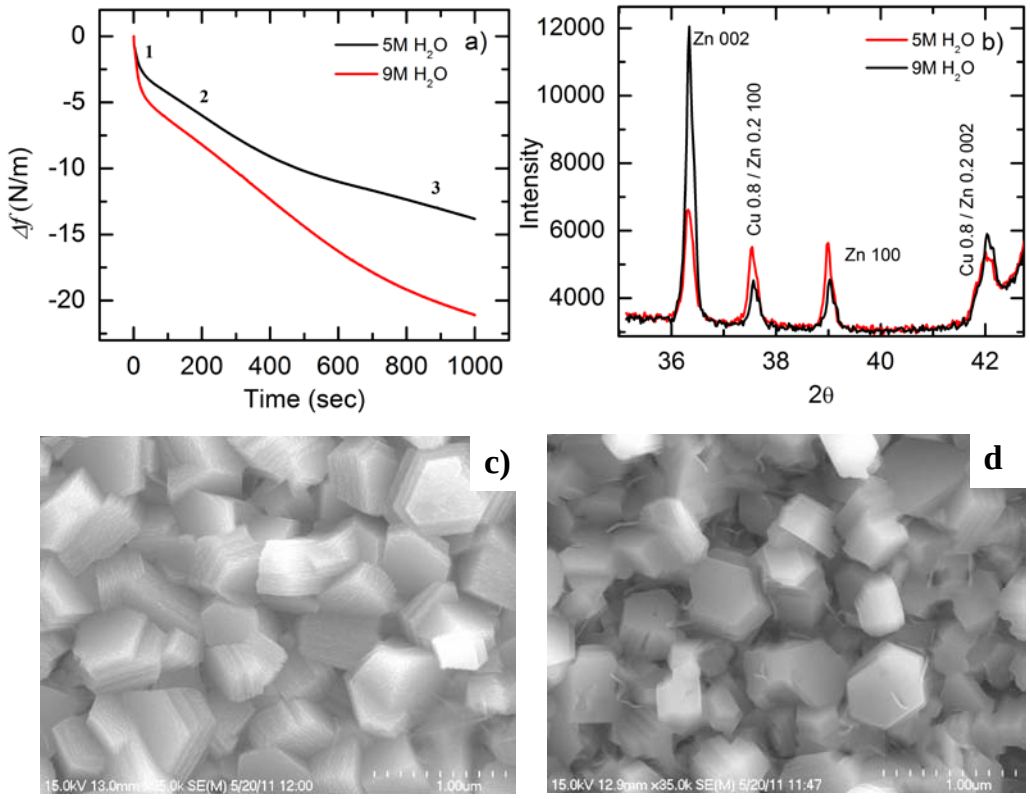

Figure 9.2: a) Surface stress response to the constant current, -1 mA/cm^2, deposition of Zn from 0.6 M $Zn(NTf_2)_2$ in $[C_2nmm][NTf_2]$ at 5 M and 9 M H_2O up to 1 C/cm^2 corresponding to a deposition overpotential of -0.3 V and -0.1 V vs. Zn respectively. The numbered regions correspond to different origins of compressive stress. b) XRD and c,d) SEM images of the 1 C/cm^2 deposition at 5 M and 9 M H_2O respectively at 35 kx.

The initial compressive stress response in Region 1 is due to deposition of Zn on Cu {111} and is attributed to either heteroepitaxy or Cu/Zn alloying. Insight into the heteroepitaxy hypothesis is found by calculation of the anticipated surface stress from the elastic strain accommodating the lattice mismatch between the Zn

and Cu [103]. The Cu {111} lattice constant is $a_{Cu\{111\}}$=0.22 nm, whereas the basal plane Zn (002) is a_{Zn}=0.266 nm [106,107]. The misfit strain, $\varepsilon_m=(a_s-a_f)/a_f$, is negative implying the formation of a compressive stress [103]. The biaxial modulus of Zn is 77 GPa, which yields a bulk stress, σ, of 12.9 GPa. At a constant deposition rate of -1 mA/cm^2, the thickness at 1 s is approximately 1 nm and yields a stress thickness of -12 N/m, which is an order of magnitude larger than the value measured. The large difference may be due to several factors such as the presence of an air formed Cu oxide on the Cu{111} surface prior to the experiment or stress relaxation related to the alloying of Cu/Zn. The likely cause is due to the alloying of Cu/Zn as evidenced by the XRD in Figure 9.2b. The stress associated with the elastic strain from alloying is a driving force for the formation of misfit dislocations near the interface [103]. A large enough strain in the growing metallic Zn film and concurrently developing alloy produces a critical stress above which plastic flow occurs. The motion of the misfit dislocations in the film produces strain relaxation and a decrease in the stress response to further film growth as shown by a decrease in compressive stress in Region 2 [101,108].

The slope becomes even less compressive in Region 3 indicating further relaxation at 400 s in the 5 M H_2O case, whereas it takes longer at 700 s in the 9 M H_2O case. This stress may be reaching a steady-state where further growth imparts the same surface stress change for the remainder of growth. The origin of compressive stress in this steady-state regime is possibly from a non-equilibrium surface state due to growth. Chason et. al. developed a thermodynamic model

deemed the diffusive model for thin film growth in vacuum, where the chemical potential of the surface is higher than that in the grain boundaries in the presence of a flux of atoms to the growth surface [97]. The larger chemical potential results in a driving force for atoms to move into the grain boundaries producing a compressive stress. As more atoms become incorporated into the grain boundaries, the driving force decreases, or the chemical potential difference between the surface and the grain boundary decreases, finally reaching a steady-state. Stresses continue to increase due to the growth of the grain boundary area with increasing film thickness. This mechanism is also valid for deposition in electrochemical environments [89,109].

While the shape and trending of the two curves Figure 9.2a are similar, the magnitude of the compressive stress is larger in the 9 M H_2O electrolyte. This difference may come from a few possibilities including hydrogen evolution, crystal structure and grain size. Due to the presence of H_2O, the absorption of a small amount of hydrogen is occurring in both solutions during Zn deposition, which can lead to compressive stresses. However, it was found that a large amount of hydrogen, (> 1 at%), is needed to produce such large changes in stress, and is not likely occurring in our system [89]. The crystal structures were examined via XRD after depositing 1 C/cm^2. The spectra show the presence of the α-brass Cu/Zn alloy as well as a mixture of basal plane (002) and (100) Zn, with a stronger signal of (002) Zn in the 5 M H_2O. The crystallographic texturing could be the cause of the stress differences, however, there is also a difference in grain

size between the two cases shown in Figure 9.2c,d. The morphology of the 5 M H_2O case (Figure 9.2c) is uniform throughout and yields a grain size of approximately 400 nm. The morphology yielded by the 9 M H_2O solution, however, is much less uniform due to the lower deposition overpotential. There is more competition between Zn deposition and hydrogen evolution producing an average grain size on the order of 250 nm. It was previously reported that the bulk stress in thin films is inversely proportional to the grain size as

$$\sigma = \frac{E\Delta}{d}, \tag{9.3}$$

where E is the Young's modulus of the depositing material, Δ is the constrained relaxation at the grain boundary and d is the grain size [90,110]. The surface stress measured yields larger stresses for the 9 M H_2O agreeing with the theory. However to further test the hypothesis that the majority of the stress is coming from the difference in grain size, a comparison of the rate of stress change per grain boundary area is useful. Taking the slopes in Region 3 gives values of -0.005 N/m·s and -0.008 N/m·s for 5 M and 9 M H_2O respectively. Normalizing these rates of stress change to the grain boundary surface area for each of the cases yields similar values of -6446 $N/m^3 \cdot s$ for 5 M H_2O and -6313 $N/m^3 \cdot s$ for 9 M H_2O. The similarity of the values gives significant evidence that the grain boundaries are the primary factor in the long term compressive stresses.

In order to further study the strain relaxation during the growth of Zn, deposition at a higher charge density was completed. The same deposition conditions used

for the 1 C/cm^2 deposition were utilized, however, growth was continued up to a charge of 10 C/cm^2. The stress response of both H_2O concentrations is shown in Figure 9.3a.

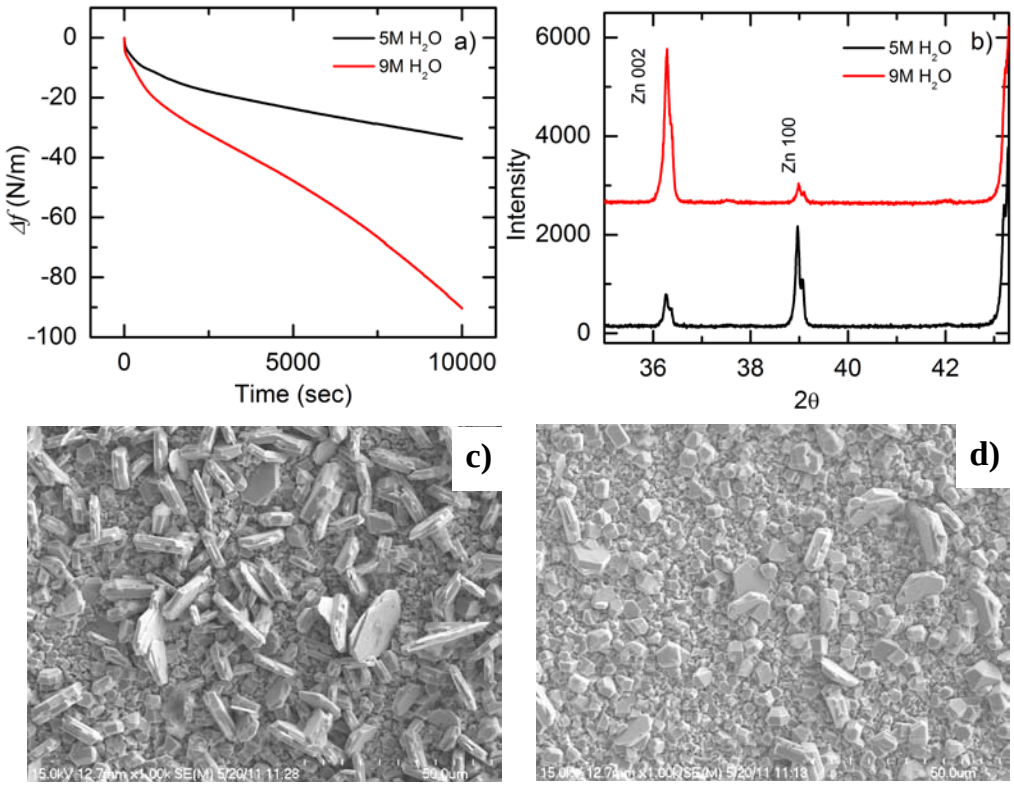

Figure 9.3: a) Surface stress response to the constant current, -1 mA/cm^2, deposition of Zn from 0.6 M $Zn(NTf_2)_2$ in $[C_2nmm][NTf_2]$ at 5 M and 9 M H_2O up to 10 C/cm^2 corresponding to a deposition overpotential of -0.3 V and -0.1 V vs. Zn respectively. b) XRD and c,d) SEM images of the 10 C/cm^2 deposition at 5 M and 9 M H_2O respectively at 1 kx.

The compressive stress for the 5 M H_2O case in Region 3 of Figure 9.2a had indeed reached a steady-state, verified by the linear stress response up to 10 C/cm^2. This is apparently the case for the 9 M H_2O up to approximately 5 C/cm^2,

where a gradual increase in the rate of compressive stress generated begins. The XRD spectra for the 10 C/cm^2 deposit (Figure 9.3b) shows the 002 basal plane becoming the dominant facet growing in the 9 M H_2O, whereas the 100 facet is the majority in the 5 M H_2O case. The difference in morphology is also apparent in the SEM images in Figure 9.3c,d. It is possible that the difference in crystal orientation is causing the increase in stress. As previously stated, the mechanism for compressive stress generation in the steady-state regime may be due to a chemical potential difference between the surface and grain boundary under a flow of atoms to the surface [97]. As the basal plane begins to dominate the surface morphology in 9 M H_2O at > 5 C/cm^2, the flow of atoms into the grain boundaries produces higher stresses. This suggests that the structure of grain boundaries of the 100 faceted grains generate lower stresses than the 002 faceted boundaries. The basal plane facet has the minimum surface energy compared to all other crystal facets in hexagonal Zn [111]. The (002) grains will have (100) grain boundaries, which are higher surface energy causing higher stresses to develop. Conversely, the 100 facets have (002) grain boundaries, which have a lower surface energy producing less compressive stress. This is only conjecture at this point, since more work needs to be done to verify the structure of the grain boundaries through methods such as XRD pole figures.

9.3.2 Stress Generated from Dealloying Cu/Zn

The Cu/Zn 80%/20% α-brass alloy present in the XRD spectra shown in Figure 9.2b is also present in the 0.1 M $Zn(NTf_2)_2$ in $[C_2nmm][NTf_2]$ under various

deposition conditions (Figure7.5, 8.3 and 8.6). Cu/Zn, or brass, alloys have been highly studied for a variety of applications [112-114], and is well known as the first system describing the Kirkendall Effect [115]. The phase diagram for the Cu/Zn system is complicated, with several alloy phases and intermetallic compounds. The most notable of the alloy phases is α-brass with concentrations of < 35% Zn. In order to more completely study this alloy formation, FIB cross sections were taken of the 1 C/cm^2 Zn deposition on Cu shown in Figure 9.4.

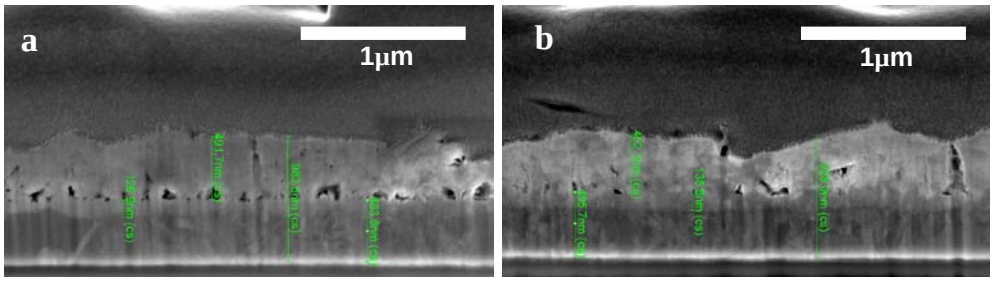

Figure 9.4: FIB cross-section of 1 C/cm^2 Zn in a) 5 M H_2O and b) 9 M H_2O solutions deposited on Cu where a Cu/Zn alloy layer is visible in each case.

The layers are described from top to bottom: Pt deposited in the FIB system to protect the Zn surface, electrodeposited Zn, α -brass Cu/Zn alloy, Cu thin film substrate. Both samples show Kirkendall voiding, which occurs when one species diffuses faster than the other. In this case, the Zn is the faster diffuser, causing voiding on the Zn side of the alloy-Zn interface [116]. Figure 9.5a shows the stress response during cyclic voltammetry at 10 mV/s.

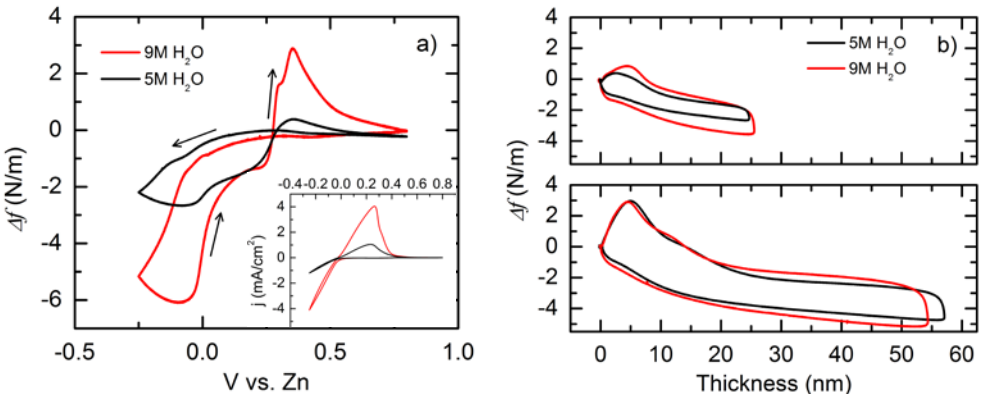

Figure 9.5: a) Surface stress vs. potential during cyclic voltammetry at 10 mV/s, j-V as inset, and b) Surface stress vs. thickness deposited as calculated from the charge density in the CV 0.6 M $Zn(NTf_2)_2$ in $[C_2nmm][NTf_2]$ at 5 M and 9 M H_2O.

Scanning cathodically, a compressive stress is generated from the deposition of Zn in the same way as described above. Upon scanning annodically, the stress is still compressive because the reduction of Zn^{2+} is still occurring until it reaches a potential near zero where the stress turns in the tensile direction due to the oxidation of Zn. The response becomes less tensile as more Zn is removed above 0V vs. Zn. When the potential reaches ~0.25 V, most of the metallic Zn on the surface has been oxidized, however a dramatic tensile rise is seen. This is due to the Zn oxidation from the α-brass Cu/Zn alloy. Analyzing the stress response between the two H_2O concentrations as a function of thickness of Zn deposited, calculated from the charge density, is shown in Figure 9.5b. For both thicknesses shown, the 9 M H_2O has a larger stress hysteresis than the 5 M H_2O, which is

explained by the grain size arguments discussed above. However, both H_2O contents show a similar stress response from dealloying.

To further study the stress response from dealloying, deposited Zn was allowed to remain on the Cu surface for varying times to allow for varying alloy thickness to develop. The potential response/profile of is shown in Figure 9.6a.

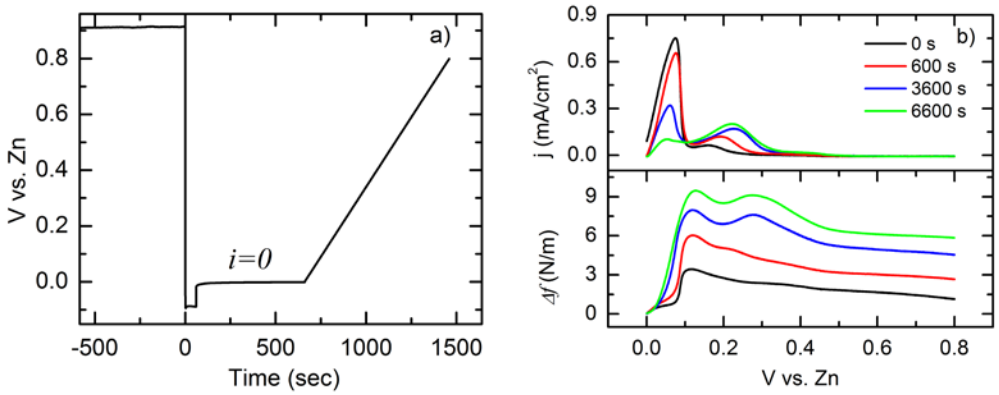

Figure 9.6: a) Potential-time profile of Zn deposition on Cu where the WE is held at OCP, pulsed down to -1 mA/cm^2 for 60 mC/cm^2, held at *i=0* for varied times (0, 600, 3600, 6600 s), then finally swept anodically at 1 mV/s from 0 V to 0.8 V vs. Zn. b) (Above) The current-voltage response and (Below) the corresponding surface stress-voltage response during the anodic sweep from 0 V up to 0.8 V vs. Zn in 0.6 M $Zn(NTf_2)_2$ in $[C_2nmm][NTf_2]$ at 9 M H_2O.

First the system is held at the open circuit potential of the Cu to characterized the drift in the stress response. Zn was then chronopotentiometrically deposited at -1 mA/cm^2 for 60 mC/cm^2 on the Cu thin film, then held at zero current for varying

times to allow the diffusion of Zn into the Cu. Immediately following the hold at *i=0*, the potential was scanned anodically at 1 mV/s from 0 V to 0.8 V vs. Zn. Each experiment was completed on a new cantilever to remove the surface roughening effects imparted by the dealloying step. The current response versus potential from the anodic scan seen in Figure 9.6b (above) shows an initial oxidation wave associated with the removal of metallic Zn on the surface, then another oxidation wave at higher potentials associated with removal of Zn from the Cu/Zn alloy. Longer holds at *i=0* results in a decrease in the initial oxidation wave, and an increase in the oxidation wave from the alloy. The corresponding surface stress response as a function of potential is shown in Figure 9.6b (below). At shorter hold times at *i=0* of 0 and 600 s, a small initial tensile rise up to 0.1V is clearly seen, which is due to the removal of metallic Zn on the surface. A large tensile stress develops above 0.1V associated with the dealloying of Zn, with signs of a second, more anodic peak developing in the 600 s signal. At the longer hold times, the initial tensile rise is no longer apparent and two tensile stress rises are seen due to the dealloying of Zn. These phenomenon are more clearly described by examining a plot of surface stress as a function of charge density shown in Figure 9.7.

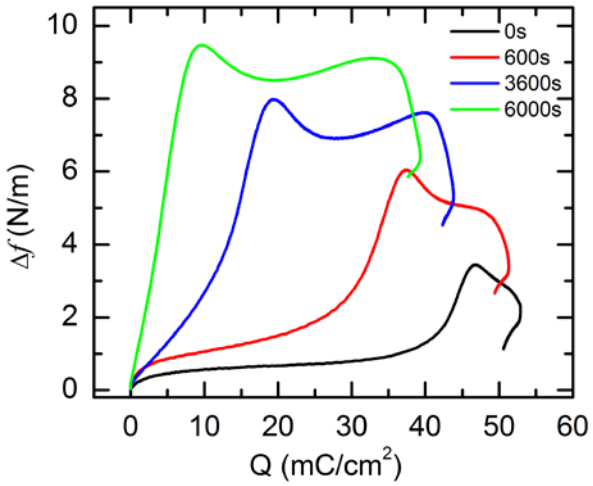

Figure 9.7: Surface stress vs. charge density during the anodic sweep (Figure 9.6) from 0 V up to 0.8 V vs. Zn in 0.6 M $Zn(NTf_2)_2$ in $[C_2nmm][NTf_2]$ at 9 M H_2O.

For the 0 s hold at *i=0*, the stress has a gradual tensile rise from the removal of metallic Zn until ~40 mC/cm^2, where tensile stress increases quickly from the removal of Zn from α-brass to a maximum indicating a majority of dealloying, then followed by turning compressive as more Zn is removed. Increasing the hold time at *i=0* to 600s yields an increase in magnitude of both the initial tensile rise and the tensile rise from the dealloying. There is also a second peak that is beginning to develop at the higher charge, just as was seen in Figure 9.6b (below). A decrease in the total charge removed during the anodic scans is also observed suggesting that some Zn is left alloyed or that significant self corrosion is occurring. However, EDX of the dealloyed Cu film shows a Zn signal confirming that the 1 mV/s anodic sweep does not remove all of the alloyed Zn. Further increasing the hold time at *i=0* to 3600s generates even higher initial tensile stresses which is due to the simultaneous removal of metallic Zn as well as Zn

from the alloy. The second peak related to the dealloying of Zn is now more clearly discernable. At the longest hold time of 6600 s, the initial rise is difficult to discern indicating the a majority of the Zn is now alloyed, and the majority of the large tensile stress is coming from the dealloying of Zn from α-brass. The origin of the two tensile stress peaks shown at longer holding times at $i=0$ comes from the removal of Zn at different locations within the alloy. The first peak comes from the removal of Zn from the alloy formed in easily accessible sites such as the surface and the grain boundaries. The second tensile peak is generated from the removal of Zn from the alloy formed in the bulk sites deeper within the Cu. Therefore, longer hold times at $i=0$ allows more Zn to diffuse into the Cu forming a thicker alloy layer allowing for Zn to diffuse into the bulk of the Cu, which in turn produces higher tensile stresses on dealloying.

Under non-steady state diffusion conditions, such as this, the concentration of Zn decreases exponentially with diffusion distance into the Cu. By simplifying a solution to the diffusion equation, an approximate expression for the diffusion thickness is $x \sim (Dt)^{0.5}$ [116]. Figure 9.8 shows the distance, x, that Zn diffused into the Cu versus time held at $i=0$.

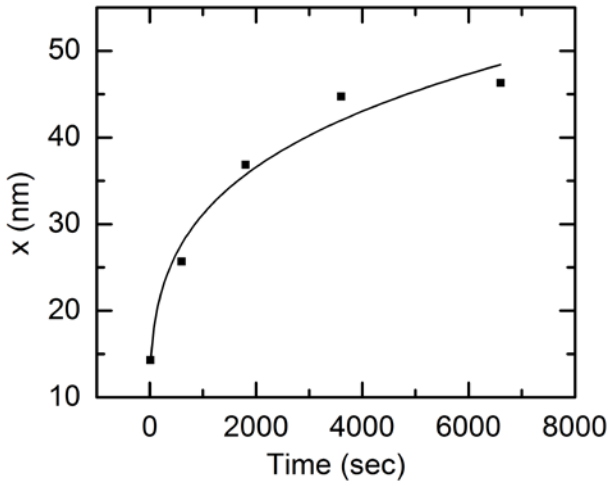

Figure 9.8: Distance Zn diffused into the Cu vs time. Thickness calculated by taking the charge under the first stripping wave in Figure 9.6a (below) via a Gaussian peak fit and subtracting it from the total charge deposited.

This was calculated by extracting the charge of the first stripping wave in Figure 9.6b (above). Because the charge of the first wave is convoluted by the second Zn stripping wave, a Gaussian fit of the wave was used to get a more accurate value of the charge. The values of each stripping charge were then subtracted from the total charge deposited to get the amount of Zn that diffused into the Cu forming the alloy. Fitting the curve in Figure 9.8 yields a fit of $x = Dt^{0.4}$, which is in good agreement with the approximate solution to the non-steady state diffusion equation.

The question of the structure of the dealloyed Cu came into question due to previous work done where porous structures were fabricated by dealloying Zn

from alloys of Cu, Au and Ag alloys [117-119]. Sieradzki et. al. developed a model describing the phenomenon of producing porous structures by dealloying. However, SEM images of the Cu film after dealloying Zn (Figure 9.9a) confirms that a porous structure is not forming under the experimental conditions tested.

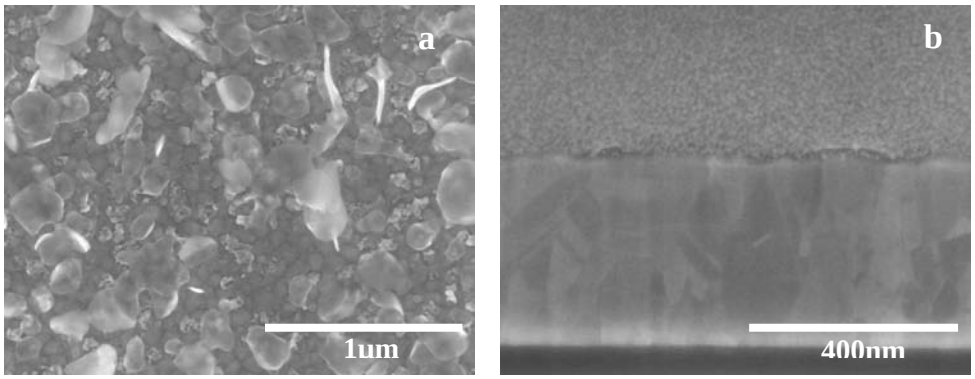

Figure 9.9: a) Copper surface after dealloying following 60 mC/cm^2 deposition with 360 0s holding at *i=0*. b) FIB cross section of the Cu (with a Pt over-layer) after dealloying showing a uniform film and a lack of porosity.

The Zn diffuses into both the grain boundaries as well as the bulk of the Cu grains. Upon dealloying, the Zn is removed from the Cu at the grain boundaries first, and then is pulled from the bulk of the Cu leaving thin dealloyed Cu "flakes" on the surface. The FIB cross-section, Figure 9.9b, confirms the lack of a porous structure.

9.4 Conclusion

The preceding work focused on electrodeposition of Zn from $[C_2nmm][NTf_2]$ / $Zn(NTf_2)_2$ ionic liquid/H_2O mixtures generated by varying the humidity. The H_2O concentration affected the morphology in terms of grain size and preferential grain orientation. The stresses that developed from these differences were measured by a direct cantilever curvature technique for film thicknesses up to 10μm. Smaller grains generate larger compressive stresses and the dominant facet in the grain boundary determines the stress magnitude that develops, where the stress from the (100) grain boundary is larger than the (002) grain boundary, $\Delta f_{\{100\}} > \Delta f_{\{002\}}$. The cycling behavior was also characterized with a large tensile stress signal developing from the Zn dealloying from the α-Cu/Zn alloy. Longer diffusion times generated larger alloy thicknesses yielding larger tensile stresses.

CHAPTER 10 AMINE, AMINE CONJUGATE ACID AND CHLORIDE CONTAMINATION IN IONIC LIQUIDS

10.01 Introduction

The motivation for the study of impurities in the ionic liquids presented itself by way of Zn deposition morphology repeatability issues in different batches of $[C_4mpy][NTf_2]$. The alkylation–anion exchange synthesis of ILs provided insight into the possible types of impurities present. Methods to determine purity ranged from elemental analysis, NMR, chromatographic techniques, cyclic voltammetry and cathodic stripping. Redox peaks on Pt were identified as a synthesis precursor, protonated n-methylpyrrolidine, and voltammetric experiments determined mM concentrations present in all batches. The presence of chloride was also examined, where μM concentrations were found, suggesting a possible alternate source of Cl^-.

10.1 Motivation and Background

An analysis into the purity of the ILs was spurred when morphological irregularities between batches was found. While testing the $[C_2nmm][NTf_2]$, concurrent analysis of several other ILs was done. An $[NTf_2]^-$ IL of particular interest was butyl-methyl pyrrolidinum bis(trifluoromethanesulfonyl)imide $[NTf_2]^-$ $[C_4mpy][TfN_2]$ due to its low melting temperature, T_m = -18 °C [120] as well as a higher $Zn(NTf_2)_2$ solubility of 1.3 M, Figure 10.1.

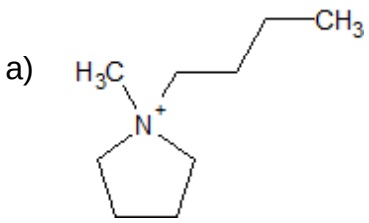

Figure 10.1: $[C_4mpy]$ cation in the $[C_4mpy][NTf_2]$.

The IL was widely commercially available, so testing a large number of batches from different sources was possible. Figure 10.2 shows Zn morphologies in different batches of $[C_4mpy][TfN_2]$ at -3 mA/cm^2 and 100 C/cm^2 in a solution containing 1M $Zn(NTf_2)_2$.

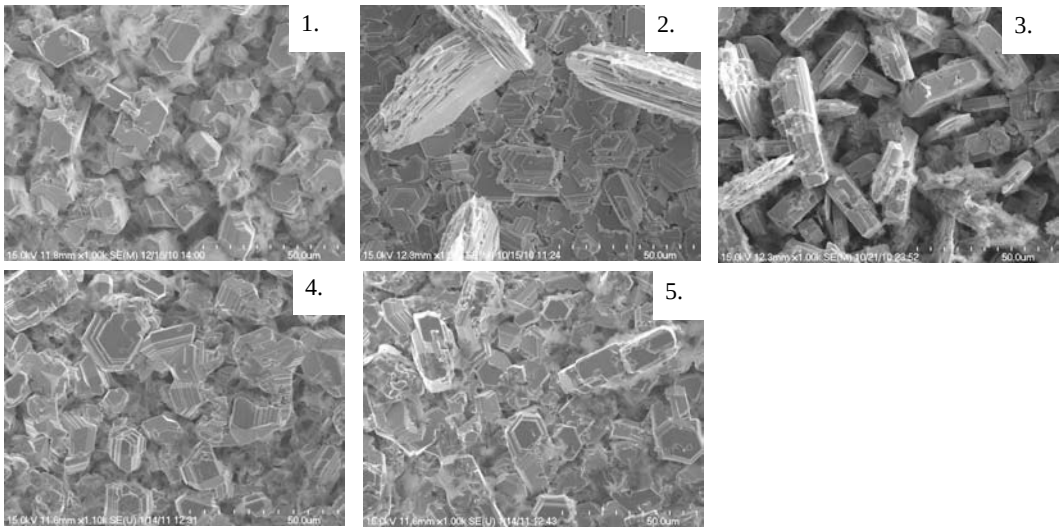

Figure 10.2: Zn deposition in several batches of $[C_4mpy][TfN_2]$ -3 mA/cm^2, 100 C/cm^2, 1M $Zn(NTf_2)_2$.

The deposition conditions were identical in each experiment, including water content, cell size and counter electrode placement. Batches (4) and (5) match fairly closely, however, batches (1)-(3) show markedly different growths suggesting spurious adsorption processes from unknown constituents in the ILs

was occurring. From these results a full analysis of the synthesis and purity analysis techniques was completed.

Literature that explicitly address the topic of ionic liquid (IL) purity [121-124] addresses the following four classes of impurities, all of which are characteristic of the typical alkylation–anion exchange synthesis of ILs, and some of which may be present in various degrees of protonation: unreacted reagents from the alkylation step, byproducts arising from the alkylation step, the reagent used to affect anion exchange, and residual solvents used throughout the preparation. With more applications where the use of ILs is beneficial, the area of IL preparation has been revisited frequently over the years [125-149]. However, these references generally do not insist on the necessity to prepare and work with ILs of high purity. Rather, the overarching themes are the necessity to make a reasonable effort to maximize IL purity either by existing methods or by methods of the author's creation, as well as to qualify the IL purity with respect to the particular application. Stark and coworkers put it well when they evaluated several quantitative and qualitative methods to detect each of the four classes of impurities, concluding, ". . . a detailed specification of the quality of [ILs] used for each experiment is most likely more essential than working with ultra-pure, expensive material." [124] With this in mind, an electrochemical method was developed to qualify the ILs particularly for contamination by residual amine building blocks, their conjugate acids, and residual chloride. To demonstrate the universality of this technique, ILs of different anions and cations were analyzed:

butyl-methylpyrrolidinum bis(trifluoromethanesulfonyl)imide,[C_4mpy][NTf_2], and 1-butyl-2,3-butyl-dimethylimidazolium triflate, [C_4dmim][OTf].

10.2 Experimental

10.2.1 General IL Purity

The [C_4mpy][NTf_2] and [C_4dmim][OTf] batches examined are from multiple commercial sources. The purpose of this work is to provide insight as to the quantity and impact of known impurities in the ILs with known synthesis and processing techniques. Therefore, the vendor sources are not differentiated. Six [C_4mpy][NTf_2] commercial batches were used in these experiments. The ^{1}H and ^{13}C NMR spectra (Appendix A) of all specimens, except Batch (6) were free of peaks uncharacteristic of the IL. The ^{1}H spectrum yielded an unidentified peak at 2.3 ppm for Batch (6). Each specimen was also characterized by elemental analysis (EA), which is a better indicator than NMR of the absolute purity of the sample. The IL is combusted in an O_2 rich atmosphere, where the combustion products of CO_2, H_2O and N_2 are measured to determine the weight percent of C, H and N respectively [150]. Note the batches were not dried prior to elemental analysis; rather, the water content was included, determined by Karl Fischer analysis, in the calculated CHN values (Table 10.1). Samples within 0.4 wt% of the calculated C, H and N concentrations are considered passing, though batches (3) and (6) both failed EA. Furthermore, ethanol solutions of [C_4mpy][NTf_2] stocks were subjected to the silver test and all passed; Stark and coworkers demonstrated that ethanol does not interfere with the silver test [124]. The resulting

pyrollidinium-based ILs are shown in Figure 10.3, where the batches range from clear to dark brown. The presence of color has been seen as an indicator of an increase in impurity level [48].

Table 10.1: Elemental analysis for $[C_4mpy][NTf_2]$ batches. Batch (3) and (6) failed.

Batch	Analysis			
		C	H	N
1	Calculated	31.3	4.8	6.6
	Found	30.9	4.8	7.0
2	Found	31.2	4.5	6.3
3	Found	30.8	5.4	6.7
4	Found	31.3	5.1	6.7
5	Found	31.2	4.9	6.9
6	Found	31.4	5.5	6.7

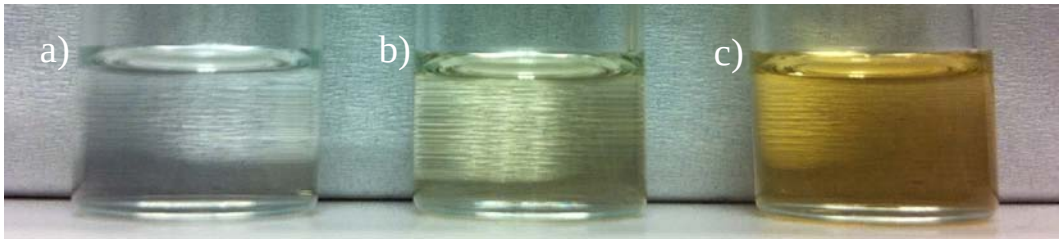

Figure 10.3: Different batches of $[C_4mpy][NTf_2]$ with varying color. a) Batch (1), b) Batch (2) and c) Batch (3). Batch (4), (5) and (6) are indistinguishable from a).

Moving now to the imidazolium based ILs, four batches were tested. The ^1H and ^{13}C NMR spectra of all specimens were free of peaks uncharacteristic of the

IL (Appendix A). Elemental analysis was completed in the same way as described for the $[C_4mpy][NTf_2]$, where water contents determined by KF analysis were included in the calculated CHN values (Table 10.2).

All [C_4dmim][OTf] batches, except Batch (7), failed EA. The resulting imidazlium-based ILs are shown have similar coloring to the pyrrolidinium ILs in Figure 10.3. Batches (9) and (10) are close to Figure 10.3a, with only a slight presence of color, and Batch (7) and Batch (8) are indistinguishable from Figure 10.3b and Figure 10.3c respectively.

Table 10.2: Elemental analysis for [C_4dmim][OTf] batches. Batches (8)-(10) failed.

Batch	Analysis			
		C	H	N
7	Calculated	39.7	5.7	9.3
	Found	39.5	6.1	9.5
8	Found	39.5	6.3	9.3
9	Found	39.8	6.4	9.2
10	Found	39.5	6.3	9.1

10.2.2 Amine Detection

Chromatographic techniques are commonly used to evaluate amine concentrations in the ILs. Thin layer chromatography is commonly used during the synthesis of ILs to determine the extent of consumption of amine, however since this is a qualitative method, the sensitivity is ill-defined [151]. Ion Chromatography (IC)

and High Performance Liquid Chromatography (HPLC) can also utilized to determine excesses, though qualification of these methods are beyond the scope of this study [48,124,152,153]. Stark and coworkers also developed a UV-spectroscopy technique to detect the presence of non-aromatic amines. The following work outlines a novel electrochemical method to quantify residual amine concentration in this study via cyclic voltammetry on Pt. A small, 1 mL three electrode cell was designed in order to preserve IL with a Pt working electrode, a coiled Pt-Ir counter electrode and a Pd-H reference electrode. The Pt and Pt-Ir were acid cleaned in heated, concentrated HNO_3 and H_2SO_4, rinsed in UPW (ultra-pure water), then hydrogen flame annealed. The Pt working electrode was then polished down to 1 μm Alumina. The Pd–H electrode was made by holding at –0.5 V vs. SCE in an aqueous 0.1 M H_2SO_4 electrolyte until there was visible bulk hydrogen evolution from the surface. Because the Pd-H reference electrode tends to shift with additions of acid, the results are reported versus ferrocene/ferrocenium, Fc/Fc^+. All experiments were done in a dry nitrogen glove box in order to maintain an O_2 and H_2O free working environment. In order to fully remove the H_2O from the ionic liquid prior to the experiment, it was heated to 70 °C and purged with Ar (>18 hours). The water content was tested with a Karl Fischer titration method and was found to be <1 ppm H_2O for all experiments.

10.2.3 Chloride Detection

Various electrochemical techniques have also been implemented to determine the presence chloride and precursor impurities [48,49,154-157]. The standard method for the determination of the amount of chloride present in an aqueous solution is by the titration of excess silver nitrate. AgCl(s) is precipitated out of solution via the following reaction [150]

$$Ag^{+} + Cl^{-} \rightarrow AgCl(s)\,. \qquad (10.1)$$

The solubility of AgCl in 100 g water is 89 μg at 10°C [158], 190 μg at 25°C [159], and 2100 μg at 100°C [158], corresponding to 6.2 μM, 13.3 μM, and 146.5 μM, respectively. Kazarian and coworkers [160] have stated that the chloride content of an IL must be less than the solubility limit of AgCl in water when an aqueous wash of either a hydrophobic IL or a hydrophilic IL in an organic solvent does not respond to $AgNO_3$. This spot test for residual halide is known as the silver test, though as it is an indirect measure of chloride, an absolute value in each batch cannot be determined. Additionally, there is no confidence that the partition coefficient of the offending halide salts between water and any IL or a solution of it is 1. Thus, it is more accurate to say that when the IL passes the silver test, it only indicates a meaningful amount of halide can no longer be extracted from the formulation. Therefore, it is not a determination that IL formulation is free of halide or that the level of halide contamination to be below a certain number.

Chromatographic methods of IC and HPLC are also an an effective means for quantification of Cl^{-} beyond the detection limits of the silver test, where ppm levels are easily attainable, and ppb levels are possible depending on the

method[152,154,161]. Electrochemical techniques such as cyclic and square wave voltammetry have been done to quantify larger concentrations of Cl^- on order of 1mM is commonly done [155]. For solutions with lower Cl^- levels, cathodic stripping of AgCl from a silver wire is much more sensitive [154]. The following work will outline a technique for the electrochemical detection of Cl^-. With the same 1 mL three electrode cell design, voltammetry on a 0.5mm diameter Ag disk working electrode was done in order to determine chloride concentration. The Ag disk was polished in the glove box just before running in order to ensure a clean, oxide free surface. A coiled Pt-Ir counter electrode and a Pd-H reference electrode were also used and prepared with the same methods described for the amine test. All experiments were done in a dry nitrogen glove box and electrolyte was prepared in the same way as described above to remove water.

10.3 Results and Discussion:

10.3.1 Electrochemical Quantification of Amine

Cyclic voltammetry on a polished Pt working electrode in various batches of $[C_4mpy][NTf_2]$ is shown in Figure 10.4a. The electrochemical window is similar for all batches, however there is the dramatic presence of an impurity wave at approximately -1 V versus Fc/Fc^+, which varies in magnitude.

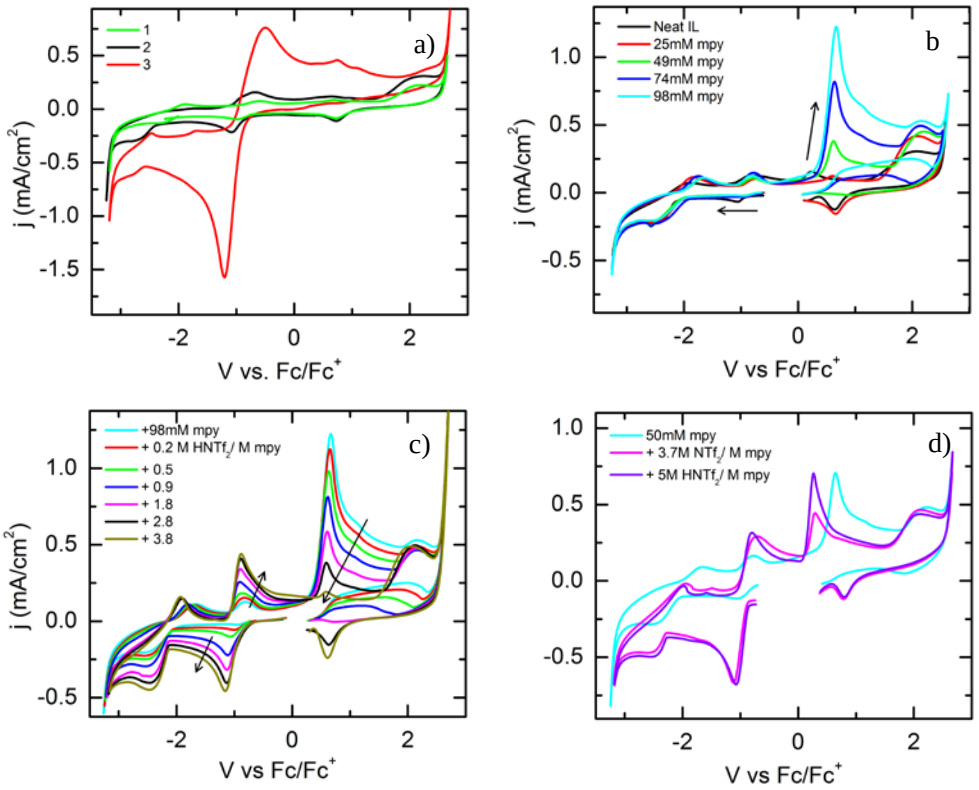

Figure 10.4: a) CV in various batches of dried (< 1 ppm H_2O) $[C_4mpy][NTf_2]$. Additions were made to Batch (1) for the following experiments starting with the b) titration of n-methyl pyrrolidine (mpy) with an oxidation wave at 1.5 V increases with increasing mpy addition. c) Addition of $HNTF_2$ to a solution of 98mM mpy. d) Excess $HNTF_2$ shows the oxidation of $HNTF_2$ at ~1 V. 100 mV/s, 1st scan on Pt WE, Pt-IR CE, PdH RE.

The voltammetry of Batches (1) and (2) show the turn on of the oxidation and reduction of PtO at 1.5 V and 1 V, respectively. The voltammetry of Batch (3) shows the presence of an additional oxidation wave at 0.7 V and a complete muting of PtO oxidation and reduction. In order to test the hypothesis that the n-

methylpyrrolidine, mpy, precursor is causing the impurity wave seen at -1V, a titration of mpy was completed in Batch (1) shown in Figure 10.4b, having the lowest impurity signal. An oxidation wave at 0.6 V increases with increasing mpy addition, and PtO oxidation and reduction is muted, similar to what was seen in Batch (3) in Figure 10.4a . However, the impurity wave at -1 V is not increasing with mpy addition alone. Figure 10.4c shows the addition of the conjugate acid $HNTF_2$ to the solution of 98mM mpy. mpy oxidation decreases with increasing $HNTF_2$, indicating the conjugate acid of mpy is protected against oxidation. The impurity wave at -1 V increases with increasing $HNTF_2$, reaching a maximum at a concentration of approximately 3:1M $HNTF_2$ to mpy where all of the mpy is protontated to $mpyH^+$. It is surprising that the ratio is not 1:1 $HNTF_2$:mpy, though there is some dispute over the acid strength of $HNTF_2$[162-164]. To be sure the impurity wave is not due to $HNTF_2$ alone, an excess was added in Figure 10.4d, where a new $HNTF_2$ oxidation wave is seen at 0.4 V negative of the oxidation of mpy. This observation confirms the impurity wave at -1 V is due to the deprotonation (cathodic) and reprotonation (anodic) of $mpyH^+$. The additional oxidation wave seen in the voltammetry of Batch (3) in Figure 10.4a at 0.7 V is due to an excess of unreacted mpy, which also explains the muting of the PtO response.

In order to determine the amount of residual amine present in each batch of $[C_4mpy][NTf_2]$, controlled amounts of discrete, prepared of 3:1 $HNTF_2$:mpy were added to Batch (1) shown in Figure 10.5a.

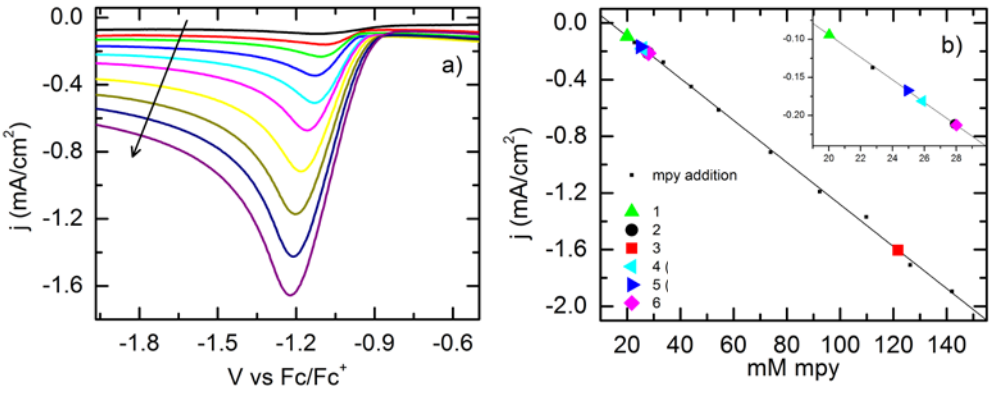

Figure 10.5: a) Additions of 3:1 $HNTF_2$: mpy to $[C_4mpy][NTf_2]$ (Batch (1)) b) cathodic peak current density vs. mM mpy in several batches of $[C_4mpy][NTf_2]$. All work done in dry (<1 ppm H_2O) IL at 100 mV/s, 1st scan on Pt WE, Pt-IR CE, PdH RE.

The cathodic peak current density was then plotted against the amount of mpy added, Figure 10.5b. The peak current densities of the impurity wave for each of the batches were fitted to the calibration, subtracting the initial signal from the neat Batch (1), yielding absolute values of mpy. All batches contained less than 30 mM (<1 at.%) mpy, though Batch (3) was found to have 120 mM, or 3.8 at%, mpy. The large value found in Batch (3) is not surprising, since it failed EA with a large mass percentage deviation (Table 10.1) and it arrived with a dark brown color (Figure 10.3c). Interestingly, though, Batch (6) which also just barely failed EA, yielded a similar mpy value to that of the passing Batch (2).

In a similar manner to the electrochemical experiments in $[C_4mpy][NTf_2]$, cyclic voltammetry was performed on a polished Pt working electrode in various batches of $[C_4dmim][OTf]$ as shown in Figure 10.6a.

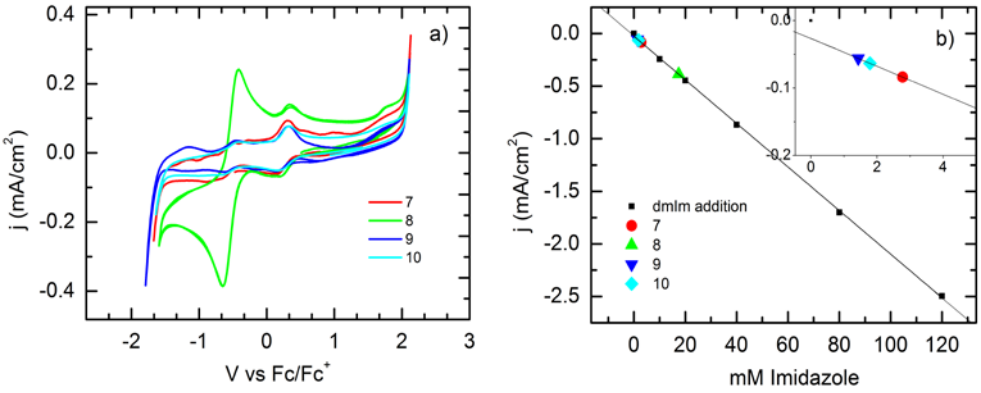

Figure 10.6: a) Cyclic voltammograms for Pt disk working electrode in various batches of $[C_4dmim][OTf]$. b) Calibration curve of cathodic peak current density versus additions of 1:1 TfOH: imidizole to $[C_4dmim][OTf]$. All work done at 50°C in dry (<1 ppm H_2O) IL at 100 mV/s, 1st scan on Pt WE, Pt-IR CE, PdH RE. Data provided by Elise Switzer.

The electrochemical window is similar for all batches, although an impurity wave exists at approximately -0.5 V versus Fc/Fc^+, most notably in Batch 8. In order to test the hypothesis that the impurity wave is a result of residual 1,2-dimethylimidazole, a titration of 1:1M 1,2-dimethylimidazole to triflic acid (TfOH) was performed in Batch 9, which had the lowest impurity signal. In an identical manner to the $[C_4mpy][NTf_2]$ experiments, the cathodic peak current density was plotted against the imidazole concentration resulting in a calibration curve, Figure 10.6b. The peak current densities of the impurity wave for each of

the batches was fitted to the calibration, yielding values of less than 3 mM (<0.1 at.%) for all but Batch 8, which has 17 mM, or 0.4 at.% unreacted imidazole. Again mM concentrations of unreacted imidazole are seen, though levels are lower than what was found for mpy in $[C_4mpy][NTf_2]$. This result is somewhat unexpected since Batches (8)-(10) all failed EA, though the largest electrochemical impurity signal is only seen in Batch (8). The signal amount detected in Batch (7), which passed EA, is also similar to that found in failing Batches (9) and (10).

The mM concentrations of these other batches are quite large with respect to impurities levels normally allowed in electrochemical experiments. For example, testing highly surface sensitive systems (e.g. catalysis and electrodeposition), mM impurities can have a huge deleterious affect. Testing ILs with different cations and anions shows the universality of this electrochemical testing method for detecting residual unreacted amine. Even more apparent from these experiments is that NMR is not sufficient in detecting impurities relevant for electrochemical applications. EA seems to detect larger amounts of impurities quite well, however, errors in this technique appear at lower levels of impurities as evidenced by Batches (6) and (7) for $[C_4mpy][NTf_2]$ and $[C_4dmim][OTf]$, respectively. The electrochemical method outlined is an excellent addition to these standard testing techniques because it is able to show the absolute amount of residual protonated amine present in the IL.

10.3.2 Electrochemical Chloride Detection

The chloride levels were tested in the [C_4mpy][NTf_2] ILs only. Figure 10.7a shows cyclic voltammetry in Batch (1) with the addition of 10mM [C4mpy][Cl].

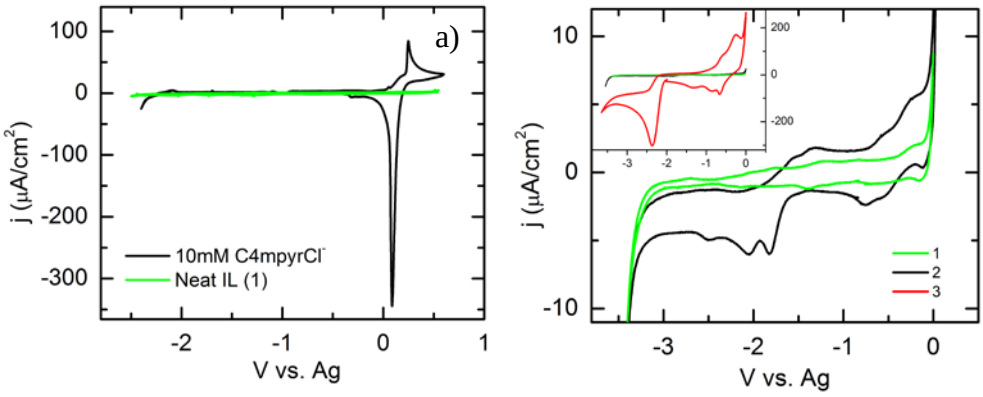

Figure 10.7: a) Addition of 10 mM [C4mpy][Cl] in Batch (1) vs Ag reference electrode. and b) Neat ILs. All done at 10mV/s WE: Polished Ag wire, CE: Flame Annealed Pt-Ir, RE: Pd-H or Ag.

The oxidation of Ag^+ at 0 V vs Ag is hindered by the anodic formation of AgCl in the presence of Cl^- via Equation 10.1. Upon scanning cathodically, the AgCl is stripped off the surface into solution. Figure 10.7b is the voltammetry in Batches (1)-(3) on a Ag working electrode. It is apparent that the amine is highly active on the Ag surface (~ -2 V), however, there is no sign anodic of AgCl formation at this scan rate. This observation only indicates that there is not enough Cl^- is present to be detectable by CV at this scan rate (< 10 mM). To determine if any detectable Cl^- is present, the Ag working electrode was held at -0.1 V vs. Ag, just below the Ag oxidation potential to anodically deposit AgCl. In order to

maximize the AgCl formation, the solution was held this potential for 18 hours and stirred to provide convection to the electrode surface. Following the chronoamperometric hold to form AgCl, the stirring was stopped and the solution was allowed to become quiescent. The electrode was then scanned using linear sweep voltammetry (LSV) cathodically from -0.1 to -1.5 V vs. Ag at 1 mV/s. All batches yielded a cathodic AgCl stripping wave of varying magnitudes as seen in Figure 10.8a.

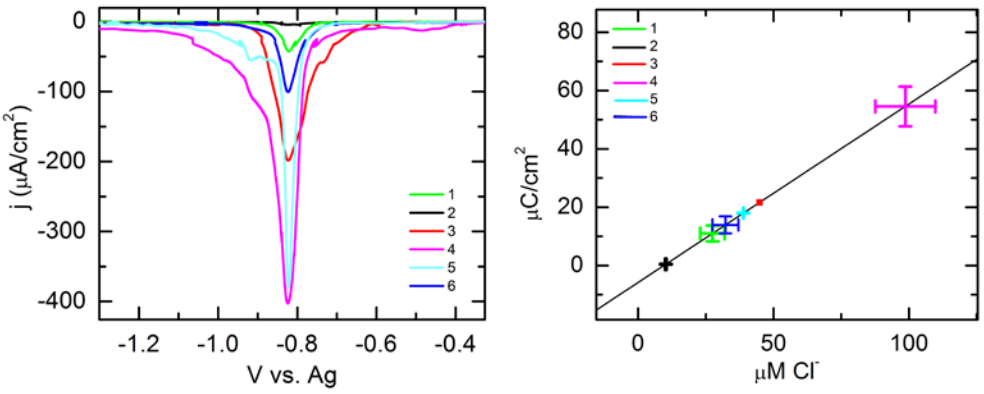

Figure 10.8: a) LSV at 1mV/s on Ag WE after being held in AgCl region in various $[C_4mpy][NTf_2]$ batches. b) Calibration titration of $[C_4mpy][Cl]$ into Batch (2) (black line) and the fit of each batch.

This is surprising because Batch (6) was advertised as inherently halide-free. Batch (2) had the lowest Cl^- concentration, and was used to develop a calibration curve by performing a $[C_4mpy][Cl]$ titration. Chronoamperometric holds were performed in solutions containing 0.1 μM to 200 μM $[C_4mpy][Cl]$, followed by LSV under the same conditions described above. The charge density under the stripping wave was calculated for each concentration, subtracting the initial Cl^-

signal from Batch (2), and plotted against [C4mpy][Cl] concentration as shown in Figure 10.8b (black line). The charge measured for each batch was fitted to the calibration curve, allowing the determination of Cl^- concentration. The values ranged from 10 – 100 μM (~1-10 ppm) which is below the detection limit of the silver nitrate precipitation test.

Just as shown in the amine levels, the amount of Cl^- may also be detrimental to extremely surface sensitive electrochemical systems. The vendor that produced Batch (6) stated that the preparation does not expose the IL to any source of discrete chloride, so curiosity was piqued when detectable levels of Cl^- were found. It is well known that NTf_2 ILs are prepared with $LiNTf_2$ as a precursor [141]. Purity and electrochemistry of this salt has been evaluated, though not with respect to Cl^- content [165,166]. To test whether $LiNTf_2$ may be a source of Cl^-, a large quantity (1.2 M) was added to Batch (2), producing a highly viscous solution. Cyclic voltammetry on Ag revealed a large AgCl wave, similar to that shown in Figure 10.7a, suggesting that there is on the order of 10mM Cl^- introduced into the solution by the addition of the $LiNTF_2$ salt. This result may reveal a hidden source of Cl^- in the IL synthesis. As $LiNTf_2$ is a widely used salt in many IL applications, a broader study of the $LiNTf_2$ may be highly useful, and is suggested for further study.

Table 10.3: Summary of $mpyH^+$ and Cl^- concentrations by batch.

Batch	mM mpy or dmIm	at% mpy or dmIm	Average µM Cl^-
(1)	20.0	0.63	27.5
(2)	27.9	0.87	10.2
(3)	121.7	3.80	44.8
(4)	25.9	0.81	98.6
(5)	24.9	0.78	38.9
(6)	28.0	0.88	32.3
(7)	2.8	0.06	-
(8)	17.4	0.41	-
(9)	1.4	0.03	-
(10)	1.8	0.04	-

10.4 Conclusion:

Elemental analysis and NMR were not sufficient testing methods for impurity levels relevant for electrochemical experiments. Electrochemical methods allowed both the identification and quantification of residual amine building blocks, their conjugate acids, and residual chloride impurities from the known alkylation–anion exchange synthesis in $[C_4mpy][NTf_2]$ and $[C_4dmim][OTf]$. Impurity peaks found during voltammetry on platinum were due to excess protonated amine, with levels in the mM range for both ILs. By testing this method on ILs with different anions and cations, it is expected that this type of electrochemical analysis is relevant for the ever increasing library of ILs. All $[C_4mpy][NTf_2]$ batches testing positive for µM chloride levels. Preliminary results suggest that the $LiNTf_2$ synthesis precursor may be an indirect source for Cl^-.

CHAPTER 11 SUMMARY AND FUTURE WORK

11.1 Summary

Manganese oxide is one of the most studied systems for both primary battery and pseudocapacitive supercapacitor technologies [2]. The theoretical specific capacitance for MnO_2 is 1370 F/g [7], though the highest values currently achieved are from thin films with values ranging between 450 to 930 F/g [4,167]. Despite the large capacitance values measured from the thin film systems, they leave little direct application for a bulk supercapacitor device. Leveraging percolation theory to drive electrode architecture in an attempt to achieve higher specific capacitance, while having total capacities relevant to supercapacitor applications, an electrode structure was developed with a hierarchically designed tri-continuous percolated network. The three percolated phases are made up of the MnO_2 faradaically-active material, electrically conductive Ni nanoparticles and void space (pore former-templated). The pores create pathways for ionic conductivity, while the nanoscale electrically conducting phase provides both bulk conductivity and local electron transfer with the electrochemically active phase. These electrodes have yielded excellent composite specific capacitances of 422 F/g and Mn specific capacitances of 844 F/g.

Deposition of Zn in aqueous alkaline electrolytes was extensively studied due to the theoretical properties of Zn rechargeable batteries. Zn-Air batteries are of particular interest due to high specific capacities and potential for high energy density portable and motive applications. However, all of these alkaline systems

present problems with dendrite formation at the Zn electrode during recharging. These challenges in aqueous electrolytes have led to our interest in Zn deposition in ILs. Because Zn-Air batteries are open to the air, deposition from air-stable ILs is of interest. $[NTf_2]^-$ based ionic liquids are non-volatile and have a large electrochemical stability window, and $[C_2nmm][NTf_2]$ was chosen because it provides the ability to operate in a wide temperature range and it has a relatively high salt solubility compared to other non-aqueous IL electrolytes. $[C_2nmm][NTf_2]$ is a new IL electrolyte and only some of its properties, such as stability window, thermogravimetric data and conductivity, have been documented by only one other group[46,47]. The preceding work provided an in-depth electrochemical analysis of Zn deposition in $[C_2nmm][NTf_2]$, where the diffusivity of Zn and exchange current density determined as a function of H_2O concentration was completed. These results were correlated to the impact of overpotential and water on morphology. The resulting microstructure, and degree of preferential texturing were studied in detail with the addition of surface-stress measurements during Zn growth. A novel study of IL purity was also provided to show the effects of the IL alkylation–anion exchange synthesis on precursor impurities.

11.2 Future Work

Following the examination of IL impurities, the addition of the effect of the IL cation on Zn deposition is also of interest. As $[C_4mpy][NTf_2]$ Batch (1) had the lowest level of protonated n-methylpyrrolidine present and a lack of (100) faceting in the morphology, therefore making it the ideal candidate for the study. Initial work was done at varying $Zn(NTf_2)_2$ concentrations and H_2O contents. Figure 11.1 shows the morphology at 0.1M $Zn(NTf_2)_2$ and 1M $Zn(NTf_2)_2$ deposited chronopotentiometrically at -0.5mA/cm^2 and -3mA/cm^2 respectively.

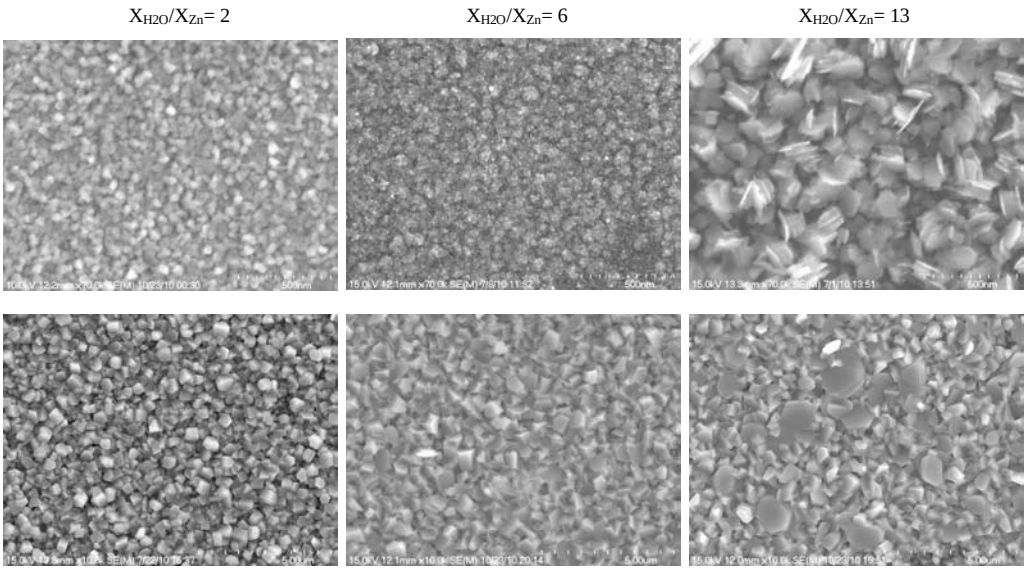

Figure 11.1: $[C_4mpy][NTf_2]$, (Batch 1) up to 1 C/cm^2 with 0.1 M $Zn(NTf_2)_2$ at -0.5 mA/cm^2 and a magnification of 70 kx (a-c), and 1 M $Zn(NTf_2)_2$ (d-f) at -3 mA/cm^2 at 10 kx magnification.

The melting temperature of $[C_4mpy][NTf_2]$ is below -18 °C, therefore a full range of H_2O concentrations can be tested at room temperature. The $Zn(NTf_2)_2$ solubility is also higher than $[C_2nmm][NTf_2]$ with a limit of 1.3M. There are some differences to the $[C_2nmm][NTf_2]$ deposition morphology, most notably is the ability to deposit of the 0.1 M Zn at a higher current density of -0.5mA/cm^2 as well as the ability to deposit in the 1 M Zn at low H_2O concentrations without dendrites forming. The morphologies at both Zn concentrations are compared by the ratio of X_{H2O}/X_{Zn} mole fractions. Increasing the H_2O concentration increases the crystallite size in both Zn contents which is tabulated in Table 11.1.

Table 11.1: Deposition parameters and crystallite size in $[C_4mpy][NTf_2]$ + 0.1M/1M $Zn(NTf_2)_2$ corresponding to the morphology shown in Figure 11.1.

X_{H2O}/X_{Zn}	2 M	6 M	13 M
0.1 M $Zn(NTf_2)_2$: V (-0.5mA/cm^2)	-0.3 → -2.6 V	-0.3→ -2.4 V	-0.2→ -1.2 V
Ave. Crystallite Size (nm)	50	80	150
0.1 M $Zn(NTf_2)_{2:}$ V (-3mA/cm^2)	-0.56 V	-0.31 V	-0.11 V
Ave. Crystallite Size (nm)	400	800	500-2000

A significant difference in crystal faceting is not seen at these charge densities, however, similar results were seen $[C_2nmm][NTf_2]$. A full analysis mirroring what has been done in the $[C_2nmm][NTf_2]$, including determination of kinetic and diffusion characteristics, and morphology dependence on overpotential, Zn concentration and water content, would be a useful comparison to study the cation

adsorption effect on the morphology. Analysis of a different cation under the same conditions will give insight into the adsorption characteristics during deposition. By additions of $[C_4mpy][NTf_2]$ into $[C_2nmm][NTf_2]$ the structure of the double layer will change. The alteration of the layered structure with these additions and change the adsorption characteristics to obtain advantageous preferential faceting.

REFERENCES

1. Kotz, R. & Carlen, M. Principles and applications of electrochemical capacitors. *Electrochimica Acta* **45**, 2483-2498 (2000).

2. Conway, B.E. *Electrochemical Supercapacitors Scientific Fundamentals and Technological Applications*. (New York, 1999).

3. Zheng, J.P., Cygan, P.J. & Jow, T.R. Hydrous Ruthenium Oxide as and Electrode Material for Electrochemical Capacitors. *Journal of The Electrochemical Society* 2699-2703 (1995).

4. Zheng, J. & Jow, T.R. High energy and high power density electrochemical capacitors. *Journal of Power Sources* **62**, 155-159 (1996).

5. Chabre, Y. et al. STRUCTURAL AND ELECTROCHEMICAL PROPERTIES OF THE PROTON / y-Mn02 SYSTEM. *Science* **23**, (1995).

6. Thackeray, M., Division, C.T. & Program, E.T. Manganese oxides for lithium batteries. *Science* **25**, 0003-4 (1997).

7. Toupin, M., Brousse, T. & Bélanger, D. Charge Storage Mechanism of MnO 2 Electrode Used in Aqueous Electrochemical Capacitor. *Chemistry of Materials* **16**, 3184-3190 (2004).

8. Pang, S.C., Anderson, M.A. & Chapman, T.W. Novel Electrode Materials for Thin-Film Ultracapacitors: Comparison of Electrochemical Properties of Sol-Gel-Derived and Electrodeposited Manganese Dioxide. *Journal of The Electrochemical Society* **147**, 444-450 (2000).

9. Mondoloni, C. Rechargeable Alkaline Manganese Dioxide Batteries. *Journal of The Electrochemical Society* **139**, 954 (1992).

10. Chae, J.H., Ng, K.C. & Chen, G.Z. Nanostructured materials for the construction of asymmetrical supercapacitors. *Proceedings of the Institution of Mechanical Engineers, Part A: Journal of Power and Energy* **224**, 479-503 (2010).

11. Hu, C. Ideal capacitive behavior of hydrous manganese oxide prepared by anodic deposition. *Electrochemistry Communications* **4**, 105-109 (2002).

12. Chang, J.-K., Huang, C.-H., Tsai, W.-T., Deng, M.-J. & Sun, I.-W. Ideal pseudocapacitive performance of the Mn oxide anodized from the nanostructured and amorphous Mn thin film electrodeposited in BMP–NTf2 ionic liquid. *Journal of Power Sources* **179**, 435-440 (2008).

13. Shinomiya, T., Gupta, V. & Miura, N. Effects of electrochemical-deposition method and microstructure on the capacitive characteristics of nano-sized manganese oxide. *Electrochimica Acta* **51**, 4412-4419 (2006).

14. Nagarajan, N., Cheong, M. & Zhitomirsky, I. Electrochemical capacitance of MnOx films. *Materials Chemistry and Physics* **103**, 47-53 (2007).

15. Nakayama, M., Kanaya, T., Lee, J.-W. & Popov, B.N. Electrochemical synthesis of birnessite-type layered manganese oxides for rechargeable lithium batteries. *Journal of Power Sources* **179**, 361-366 (2008).

16. Wang, X., Yuan, A. & Wang, Y. Supercapacitive behaviors and their temperature dependence of sol–gel synthesized nanostructured manganese dioxide in lithium hydroxide electrolyte. *Journal of Power Sources* **172**, 1007-1011 (2007).

17. Chin, S.-F., Pang, S.-C. & Anderson, M. a Material and Electrochemical Characterization of Tetrapropylammonium Manganese Oxide Thin Films as Novel Electrode Materials for Electrochemical Capacitors. *Journal of The Electrochemical Society* **149**, A379 (2002).

18. Broughton, J. & Brett, M.J. Investigation of thin sputtered Mn films for electrochemical capacitors. *Electrochimica Acta* **49**, 4439-4446 (2004).

19. Djurfors, B., Broughton, J.N., Brett, M.J. & Ivey, D.G. Microstructural characterization of porous manganese thin films for electrochemical supercapacitor applications. *Journal of Materials Science* **38**, 4817-4830 (2003).

20. Sharma, R., Oh, H., Shul, Y. & Kim, H. Carbon-supported, nano-structured, manganese oxide composite electrode for electrochemical supercapacitor. *Journal of Power Sources* **173**, 1024-1028 (2007).

21. Lee, H.Y. & Goodenough, J.B. Supercapacitor Behavior with KCl Electrolyte. *Journal of Solid State Chemistry* **223**, 220-223 (1999).

22. Yang, X., Wang, Y., Xiong, H. & Xia, Y. Interfacial synthesis of porous MnO2 and its application in electrochemical capacitor. *Electrochimica Acta* **53**, 752-757 (2007).

23. Xu, M.-W., Zhao, D.-D., Bao, S.-J. & Li, H.-L. Mesoporous amorphous MnO2 as electrode material for supercapacitor. *Journal of Solid State Electrochemistry* **11**, 1101-1107 (2007).

24. Dong, X. et al. MnO2-embedded-in-mesoporous-carbon-wall structure for use as electrochemical capacitors. *The journal of physical chemistry. B* **110**, 6015-9 (2006).

25. Zallen, R. *The Physics of Amorphous Solids*. (Wiley-Interscience: New York, 1983).

26. Stauffer, D. & Aharony, A. *Introduction to Percolation Theory*. (Taylor and Francis: Washington D.C., 1991).

27. Dovzhenko, a Y. & Bunin, V. a Effect of the shape and size of conducting particles on the percolation cluster formation in a ceramic composition. *Technical Physics* **48**, 1058-1060 (2003).

28. Xue, Q. The influence of particle shape and size on electric conductivity of metal–polymer composites. *European Polymer Journal* **40**, 323-327 (2004).

29. Zhirkov, P.V. & Dovzhenko, A.Y. The Effect of Particle Size Distribution on the Formation of Percolation Clusters. *Physics Letters A* **204**, 247-250 (1995).

30. Cho, M.S., Park, S.Y., Hwang, J.Y. & Choi, H.J. Synthesis and Electrical Peroperties of Polymer Composites with Polyaniline Nanoparticles. *Materials Science and Engineering C2* **24**, 15-18 (2004).

31. Endres, F. Ionic liquids: solvents for the electrodeposition of metals and semiconductors. *Chemphyschem : a European journal of chemical physics and physical chemistry* **3**, 145-54 (2002).

32. Paulechka, Y.U., Zaitsau, D.H., Kabo, G.J. & Strechan, a a Vapor pressure and thermal stability of ionic liquid 1-butyl-3-methylimidazolium Bis(trifluoromethylsulfonyl)amide. *Thermochimica Acta* **439**, 158-160 (2005).

33. Galinski, M., Lewandowski, a & Stepniak, I. Ionic liquids as electrolytes. *Electrochimica Acta* **51**, 5567-5580 (2006).

34. Beck, F. & Ru, P. Rechargeable batteries with aqueous electrolytes. *Environment* **45**, 2467 - 2482 (2000).

35. Friesen, C., Sieradzki, K. & Buttry, D. *Sustainable, High-Energy Density, Low Cost Electrochemical Energy Storage: Metal-Air Ionic Liquid (MAIL) Batteries*. (Arpa-E Grant Proposal, Department of Energy, 2009).

36. Lee, C., Sathiyanarayanan, K., Eom, S., Kim, H. & Yun, M. Effect of additives on the electrochemical behaviour of zinc anodes for zinc/air fuel cells. *Journal of Power Sources* **160**, 161-164 (2006).

37. Thomas, B. & Fray, D.J. Effect of additives on the morphology of Zn electrodep from ZnCl2 at high current densities. *Journal of Applied Electrochemistry* **11**, 677-683 (1980).

38. Abbott, A.P., Capper, G., Mckenzie, K.J. & Ryder, K.S. Electrodeposition of zinc – tin alloys from deep eutectic solvents based on choline chloride. *Journal of Electroanalytical Chemistry* **599**, 288-294 (2007).

39. Abbott, A.P., Boothby, D., Capper, G., Davies, D.L. & Rasheed, R.K. Deep Eutectic Solvents Formed between Choline Chloride and Carboxylic Acids : Versatile Alternatives to Ionic Liquids. 9142-9147 (2004).

40. Hsiu, S.-i, Huang, J.-fang, Sun, I.-wen, Yuan, C.-hui & Shiea, J. Lewis acidity dependency of the electrochemical window of zinc chlorideÁ 1-ethyl-3-methylimidazolium chloride ionic liquids. *Electrochimica Acta* **47**, 4367-4372 (2002).

41. Bakkar, a & Neubert, V. Electrodeposition onto magnesium in air and water stable ionic liquids: From corrosion to successful plating. *Electrochemistry Communications* **9**, 2428-2435 (2007).

42. Yamamoto, H., Kinoshita, H., Kimura, M., Shirai, H. & Koyama, K. Electrodeposition of Zn from Trimethyl propylammonium bis(trifluoromethylsulfonyl)imide Organic Molten Salt. *Electrochemistry Communications* **74**, 370-373 (2006).

43. Xu, J., Ye, H. & Huang, J. Novel zinc ion conducting polymer gel electrolytes based on ionic liquids. *Electrochemistry Communications* **7**, 1309-1317 (2005).

44. Simka, W., Puszczyk, D. & Nawrat, G. Electrochimica Acta Electrodeposition of metals from non-aqueous solutions. *Electrochimica Acta* **54**, 5307-5319 (2009).

45. Endres, F. Do Solvation Layers of IL's influence Echem reactions. *Physical Chemistry Chemical Physics* (2010).doi:10.1039/c001176m

46. Kim, K.-S. et al. Ionic liquids based on N-alkyl-N-methylmorpholinium salts as potential electrolytes. *Chemical communications (Cambridge, England)* 828-9 (2004).doi:10.1039/b400198b

47. Kim, K., Park, S., Choi, S. & Lee, H. Ionic liquid–polymer gel electrolytes based on morpholinium salt and PVdF(HFP) copolymer. *Journal of Power Sources* **155**, 385-390 (2005).

48. Billard, I. et al. Stability of divalent europium in an ionic liquid: spectroscopic investigations in 1-methyl-3-butylimidazolium hexafluorophosphate. *Inorganic chemistry* **42**, 1726-33 (2003).

49. Appetecchi, G.B., Scaccia, S., Tizzani, C., Alessandrini, F. & Passerini, S. Synthesis of Hydrophobic Ionic Liquids for Electrochemical Applications. *Journal of The Electrochemical Society* **153**, A1685 (2006).

50. Bartlett, P.N. & Whitaker, R.G. Small-volume electrochemical cell designed for rotating disk studies in bioelectrochemistry. *Analytical Chemistry* **61**, 2803-2805 (1989).

51. Vetter, K. *Electrochemical Kinetics: Theoretical and Experimental Aspects*. (Academic Press: New York, 1967).

52. Marcus, R. a On the Theory of Oxidation-Reduction Reactions Involving Electron Transfer. I. *The Journal of Chemical Physics* **24**, 966 (1956).

53. Bard, A. & Faulkner, L. *Electrochemical Methods: Fundamentals and Applications*. (John Wiley & Sons: New Jersey, 2001).

54. Bockris, J., Reddy, A. & Gamboa-Aldeco, M. *Modern Electrochemistry 2A*. (Kluwer Academic/ Plenum Publishers: New York, 2000).

55. Li, X.Y. & Nie, J. Density Functional Theory Study on Metal Bis(trifluoromethylsulfonyl)imides: Electronic Structures, Energies, Catalysis, and Predictions. *The Journal of Physical Chemistry A* **107**, 6007-6013 (2003).

56. Hartmann, M., Clark, T. & van Eldik, R. Hydration and Water Exchange of Zinc(II) Ions. Application of Density Functional Theory. *Journal of the American Chemical Society* **119**, 7843-7850 (1997).

57. Marcus, R. a On the Theory of Electron-Transfer Reactions. VI. Unified Treatment for Homogeneous and Electrode Reactions. *The Journal of Chemical Physics* **43**, 679 (1965).

58. Bockris, J. & Khan, S. *Surface Electrochemistry*. (Plenum Press: New York, NY, 1993).

59. Baldelli, S. Surface structure at the ionic liquid-electrified metal interface. *Accounts of chemical research* **41**, 421-31 (2008).

60. Lockett, V., Horne, M., Sedev, R., Rodopoulos, T. & Ralston, J. Differential capacitance of the double layer at the electrode/ionic liquids interface. *Physical chemistry chemical physics : PCCP* **12**, 12499-512 (2010).

61. Hayes, W. At the Interface: Solvation and Designing IL's. *Physical chemistry chemical physics : PCCP* **12**, 1648 (2010).

62. Moustafa, E.M. et al. Electrodeposition of Al in 1-butyl-1-methylpyrrolidinium bis(trifluoromethylsulfonyl)amide and 1-ethyl-3-methylimidazolium bis(trifluoromethylsulfonyl)amide ionic liquids: in situ STM and EQCM studies. *The journal of physical chemistry. B* **111**, 4693-704 (2007).

63. Kornyshev, A.A. Double-Layer in Ionic Liquids : Paradigm Change ? *Society* 5545-5557 (2007).

64. McManis, G.E., Golovin, M.N. & Weaver, M.J. Role of solvent reorganization dynamics in electron-transfer processes. Anomalous kinetic behavior in alcohol solvents. *The Journal of Physical Chemistry* **90**, 6563-6570 (1986).

65. Hill, N.E., Vaughan, W.E., Price, A.H. & Davies, M. *Dielectric Properties and Molecular Behaviour*. (Van Nostrand Reinhold Company: London, 1969).

66. Calef, D.F. & Wolynes, P. Classical Solvent Dynamics and Electron Transfer. 1. Continuum Theory. *Journal of Physical Chemistry* **87**, 3387-3400 (1983).

67. Miller, R.J.D., McLendon, G.L., Nozik, A.J., Schmickler, W. & Willig, F. *Surface Electron Transfer Processes*. (VCH Publishers: New York, NY, 1995).

68. Gennett, T., Milner, D.F. & Weaver, M.J. Role of solvent reorganization dynamics in electron-transfer processes. Theory-experiment comparisons for electrochemical and homogeneous electron exchange involving metallocene redox couples. *The Journal of Physical Chemistry* **89**, 2787-2794 (1985).

69. Ito, N. & Richert, R. Solvation dynamics and electric field relaxation in an imidazolium-PF6 ionic liquid: from room temperature to the glass transition. *The journal of physical chemistry. B* **111**, 5016-22 (2007).

70. Trejo, G. Nucleation and Growth of Zinc from Chloride Concentrated Solutions. *Journal of The Electrochemical Society* **145**, 4090 (1998).

71. Yu, J., Wang, L., Su, L., Ai, X. & Yang, H. Temperature Effects on the Electrodeposition of Zinc. *Journal of The Electrochemical Society* **150**, C19 (2003).

72. Bockris, J. & Reddy, A. *Modern Electrochemistry 1*. (Plenum Press: New York, NY, 1970).

73. Jiang, W., Wang, Y. & Voth, G. a Molecular dynamics simulation of nanostructural organization in ionic liquid/water mixtures. *The journal of physical chemistry. B* **111**, 4812-8 (2007).

74. Naybour, R.D. Morphologies of zinc electrodeposited from zinc-saturated aqueous alkaline solution. *Electrochimica Acta* **13**, 763-769 (1968).

75. Diggle, J.W., Despic, a R. & Bockris, J.O. The Mechanism of the Dendritic Electrocrystallization of Zinc. *Journal of The Electrochemical Society* **116**, 1503 (1969).

76. Jaksic, M. Impurity Effects on the Macromorphology of Electrodeposited Zinc III: Potential Sweep Analysis. *Surface and Coatings Technology* **29**, 95 - 104 (1986).

77. Wang, R.Y., Kirk, D.W. & Zhang, G.X. Effects of Deposition Conditions on the Morphology of Zinc Deposits from Alkaline Zincate Solutions. *Journal of The Electrochemical Society* **153**, C357 (2006).

78. Howlett, P.C., Izgorodina, E.I., Forsyth, M. & MacFarlane, D.R. Electrochemistry at Negative Potentials in Bis(trifluoromethanesulfonyl)amide Ionic Liquids. *Z. Phys. Chem.* **220**, 1483-1498 (2006).

79. Cullity, B.D. & Stock, S.R. *Elements of X-Ray Diffrction.* (Prentice Hall: New Jersey, 2001).

80. Sunagawa, I. Growth and Morphology of Crystals*. *Forma* **14**, 147-166 (1999).

81. Bockris, J.O.M., Nagy, Z. & Drazic, D. On the Morphology of Zinc Electrodeposition from Alkaline Solutions. *Journal of The Electrochemical Society* **120**, 30-41 (1973).

82. Lamping, B.A. & T.J., O. Evaluation of Zinc Sulfate Electrolytes by Cyclic Voltammetry and Electron Microscopy. *Metallurgical Transactions B* **7B**, 551-558 (1976).

83. Zhang, Q. & Hua, Y. Effect of ionic liquid additive [BMIM]HSO4 on zinc electrodeposition from impurity-containing sulfate electrolyte. Part I: current efficiency, surface morphology, and crystal orientations. *Journal of Applied Electrochemistry* **41**, 481-490 (2011).

84. Koch, R. The intrinsic stress of polycrystalline and epitaxial thin metal films. *Journal of Physics: Condensed Matter* **6**, (1994).

85. Ahmed, S., Ahmed, T.T., O'Grady, M., Nakahara, S. & Buckley, D.N. Investigation of stress and morphology in electrodeposited copper nanofilms by cantilever beam method and in situ electrochemical atomic force microscopy. *Journal of Applied Physics* **103**, 073506 (2008).

86. Heaton, T. An in situ Surface Stress Study of Electrochemical Phenomena: Electrodeposition & Molecular Adsorption. (2011).

87. Spaepen, F. Interfaces and stresses in thin films. *Acta Materialia* **48**, 31-42 (2000).

88. J.A., V. Atomic processes in crystal growth. *Surface Science* **299/300**, 798-817 (1994).

89. Hearne, S.J. & Floro, J. a Mechanisms inducing compressive stress during electrodeposition of Ni. *Journal of Applied Physics* **97**, 014901 (2005).

90. Czerwinski, F. Grain Size-Internal Stress Relationship in Iron-Nickel Alloy Electrodeposits. *Journal of The Electrochemical Society* **143**, 3327 (1996).

91. Landolt, D. Electrodeposition Science and Technology in the Last Quarter of the Twentieth Century. *Journal of The Electrochemical Society* **149**, (2002).

92. Haiss, W., Nichols, R.J. & Sass, J.-K. In situ monitoring of intrinsic stress changes during copper electrodeposition on Au(111). *Surface Science* **388**, 141-149 (1997).

93. Friesen, C. & Thompson, C.V. Reversible Stress Relaxation during Precoalescence Interruptions of Volmer-Weber Thin Film Growth. *Physical Review Letters* **89**, 1-4 (2002).

94. Friesen, C. & Thompson, C. Correlation of Stress and Atomic-Scale Surface Roughness Evolution during Intermittent Homoepitaxial Growth of (111)-Oriented Ag and Cu. *Physical Review Letters* **93**, 1-4 (2004).

95. Friesen, C., Seel, S.C. & Thompson, C.V. Reversible stress changes at all stages of Volmer–Weber film growth. *Journal of Applied Physics* **95**, 1011 (2004).

96. Heaton, T. & Friesen, C. Pt{111} and Au{111} Electrocapillarity: Interphase Structure, the pzc, and Oxygen Reduction. *Journal of Physical Chemistry C* **111**, 14433-14439 (2007).

97. Chason, E., Sheldon, B., Freund, L., Floro, J. & Hearne, S. Origin of Compressive Residual Stress in Polycrystalline Thin Films. *Physical Review Letters* **88**, 1-4 (2002).

98. Chason, E. & Sheldon, B.W. Monitoring Stress in Thin Films During Processing. *Surface Engineering* **19**, 387-391 (2003).

99. Mickelson, L., Heaton, T. & Friesen, C. Surface Stress Observations during the Adsorption and Electrochemical Oxidation of CO on Pt{111}. *Journal of Physical Chemistry C* **112**, 1060-1063 (2008).

100. Mickelson, L.L. & Friesen, C. Direct observation of bifunctional electrocatalysis during CO oxidation at Ru(theta=0.37)/Pt{111} surfaces via surface stress measurements. *Journal of the American Chemical Society* **131**, 14879-84 (2009).

101. Engstrom, E.L., Heaton, T., Kennedy, J.K. & Friesen, C. Observations in the H-Pd{111} System via Stress and EQCM Measurements. *Journal of The Electrochemical Society* (2011).

102. Stoney, G.G. The Tension of Metallic Films Deposited by Electrolysis The Tension of Metallic Films deposited by Electrolysis. *Society* **82**, 172-175 (1909).

103. Freund, L. & Suresh, S. *Thin Film Materials: Stress, Defect Formation and Surface Evolution*. (Cambridge University Press: Cambridge, 2003).

104. Gere, J.M. *Mechanics of Materials*. (Thomson: Belmont, CA, 2004).

105. Mickelson, L. Stress Evolution during Electro-Oxidation of Carbon Monoxide and Bulk Stress Evolution during Electrochemical Intercalation of Lithium. (2011).

106. Horiguchi, T. & Nakanishi, S. Cu 111 lattice parameter.pdf. *Japanese Journal of Applied Physics* **20**, L214-L216 (1981).

107. Chityuttakan, C., Wantong, K., Chatraphorn, S. & Yoodee, K. Evolution of crystal structure of Zn:N films under high temperature. *Crystal Research Technology* **45**, 925-928 (2010).

108. Nix, W. Yielding and strain hardening of thin metal films on substrates. *Scripta Materialia* **39**, 545-554 (1998).

109. Shin, J. & Chason, E. Compressive Stress Generation in Sn Thin Films and the Role of Grain Boundary Diffusion. *Physical Review Letters* **103**, 1-4 (2009).

110. Hoffman, R. Stresses in thin films: The relevance of grain boundaries and impurities. *Thin Solid Films* **34**, 185-190 (1976).

111. Matysina, Z.A. The relative surface energy of hexagonal closed-packed crystals. *Materials Chemistry and Physics* **60**, 70-78 (1999).

112. Peterson, N.L. & Rothman, S.J. Diffusion and Correlation Effects in Copper-Zinc Alloys. *Physical Review B* **2**, 1540-1547 (1970).

113. Fujiwara, Y. & Enomoto, H. Intermetallic phase formation in electrochemical alloy deposition. *Journal of Solid State Electrochemistry* **8**, 167-173 (2004).

114. Kryshtop, I.G., Yurchenko, N.P. & Trofimenko, V.V. Peculiarities of the Initial Stage of Zn Electrocrystallization on the Cu Electrode from a Zincate Electrolyte. *219th Electrochemical Society Meeting* **0**, 1552 (2011).

115. Kirkendall, E.O. Diffusion of Zinc in Alpha Brass. *Transactions of the American Institute of Mining and Metallurgical Engineers* **147**, 104-110 (1942).

116. Porter, D.A. & Easterling, K.E. *Phase transformations in metals and alloys*. (Van Nostrand Reinhold: 1981).

117. Lin, Y.-W., Tai, C.-C. & Sun, I.-W. Electrochemical Preparation of Porous Copper Surfaces in Zinc Chloride-1-ethyl-3-methyl Imidazolium Chloride Ionic Liquid. *Journal of The Electrochemical Society* **154**, D316 (2007).

118. Huang, J.-F. & Sun, I.-W. Fabrication and Surface Functionalization of Nanoporous Gold by Electrochemical Alloying/Dealloying of Au-Zn in an Ionic Liquid, and the Self-Assembly ofL-Cysteine Monolayers. *Advanced Functional Materials* **15**, 989-994 (2005).

119. Yeh, F.-H., Tai, C.-C., Huang, J.-F. & Sun, I.-W. Formation of porous silver by electrochemical alloying/dealloying in a water-insensitive zinc chloride-1-ethyl-3-methyl imidazolium chloride ionic liquid. *The journal of physical chemistry. B* **110**, 5215-22 (2006).

120. Zhang, S., Sun, N., He, X., Lu, X. & Zhang, X. Physical Properties of Ionic Liquids: Database and Evaluation. *Journal of Physical and Chemical Reference Data* **35**, 1475 (2006).

121. Seddon, K.R., Stark, A. & Torres, M.-J. Influence of chloride, water, and organic solvents on the physical properties of ionic liquids. *Pure and Applied Chemistry* **72**, 2275-2287 (2000).

122. Scammells, P.J., Scott, J.L. & Singer, R.D. Ionic Liquids : The Neglected Issues. *Australian Journal of Chemistry* **58**, 155-169 (2005).

123. Earle, M.J., Gordon, C.M., Plechkova, N.V., Seddon, K.R. & Welton, T. Decolorization of ionic liquids for spectroscopy. *Analytical chemistry* **79**, 758-64 (2007).

124. Stark, A. et al. Purity specification methods for ionic liquids. *Green Chemistry* **10**, 1152 (2008).

125. Wier, T.P. & Hurley, F.H. Electrodeposition of Metals from Fused Quaternary Ammonium Salts. *Journal of The Electrochemical Society* **98**, 203-206 (1951).

126. Koch, V.R., Miller, L.L. & Osteryoung, R.A. Electroinitiated Friedel-Crafts Transalkylations in Room-Temperature Molten-Salt Medium. *Journal of the American Chemical Society* **98**, 5277-5284 (1975).

127. Gifford, P.R. & Palmisano, J.B. A Substituted Imidazolium Chloroaluminate Molten Salt Possessing an Increased Electrochemical Window. *Journal of The Electrochemical Society* **134**, 610-614 (1987).

128. Wilkes, J.S. & Zaworotko, M.J. Air and water stable 1-ethyl-3-methylimidazolium based ionic liquids. *Journal of the Chemical Society* **1992**, 956-967 (1992).

129. Carlin, R.T., Long, H.C.D., Fuller, J. & Trulove, P.C. Dual Intercalating Molten Electrolyte Batteries. *Electrochemical Society Letters* **141**, 7-10 (1994).

130. Bonhôte, P. et al. Additions and Corrections 1996,. *Inorganic chemistry* **35**, 166 (1996).

131. Earle, M.J. & Seddon, K.R. Imidazole Carbenes - Patent. (2001).

132. Cammarata, L., Kazarian, S.G., Salter, P. a & Welton, T. Molecular states of water in room temperature ionic liquidsElectronic Supplementary Information available. See http://www.rsc.org/suppdata/cp/b1/b106900d/. *Physical Chemistry Chemical Physics* **3**, 5192-5200 (2001).

133. Holbrey, J.D. et al. Efficient, halide free synthesis of new, low cost ionic liquids: 1,3-dialkylimidazolium salts containing methyl- and ethyl-sulfate anions. *Green Chemistry* **4**, 407-413 (2002).

134. Lancaster, N.L., Salter, P. a, Welton T, T. & Young, G.B. Nucleophilicity in ionic liquids. 2. Cation effects on halide nucleophilicity in a series of bis(trifluoromethylsulfonyl)imide ionic liquids. *The Journal of organic chemistry* **67**, 8855-61 (2002).

135. Holbrey, J.D. et al. 1 , 3-Dimethylimidazolium-2-carboxylate : the unexpected synthesis of an ionic liquid precursor and carbene-CO 2 adduct. *Chemical Communications* 28-29 (2003).

136. Dyson, P.J., Ellis, D.J., Henderson, W. & Laurenczy, G. A Comparison of Ruthenium-Catalysed Arene Hydrogenation Reactions in Water and 1-Alkyl-3-methylimidazolium Tetrafluoroborate Ionic Liquids. *Advanced Synthesis and Catalysis* **345**, 216-221 (2003).

137. Zhang, J., Martin, G.R. & Desmarteau, D.D. Direct methylation and trifluoroethylation of imidazole and pyridine derivatives. *Chemical Communications* 2334-2335 (2003).

138. Karkkainen, J., Asikkala, J., Laitinen, R.S. & Lajunen, M.K. Effect of temperature on the purity of product in the prepartion of 1-butyl-3-methylimidazolium-based ionic liquids. *Zeitschrift für Naturforschung. B* **59**, 763-770 (2004).

139. Zhou, Z.-B., Takeda, M. & Ue, M. New hydrophobic ionic liquids based on perfluoroalkyltrifluoroborate anions. *Journal of Fluorine Chemistry* **125**, 471-476 (2004).

140. Creary, X. & Willis, E. Preparation of 1-butyl-3-methylimidazolium tetrafluoroborate. *Organic Synthesis* **82**, 166 (2005).

141. Appetecchi, G.B., Scaccia, S., Tizzani, C., Alessandrini, F. & Passerini, S. Synthesis of Hydrophobic Ionic Liquids for Electrochemical Applications. *Journal of The Electrochemical Society* **153**, A1685 (2006).

142. Smiglak, M. et al. Ionic liquids via reaction of the zwitterionic 1,3-dimethylimidazolium-2-carboxylate with protic acids. Overcoming synthetic limitations and establishing new halide free protocols for the formation of ILs. *Green Chemistry* **9**, 90 (2007).

143. Kuhlmann, E., Himmler, S., Giebelhaus, H. & Wasserscheid, P. Imidazolium dialkylphosphates - a class of versatile, halogen-free and hydrolytically stable ionic liquids. *Green Chemistry* **9**, 233 (2007).

144. Burrell, A.K., Sesto, E.D., Baker, S.N., Mark, T. & Baker, G.A. The large scale synthesis of pure imidazolium and pyrrolidinium ionic liquids. *Green Chemistry* **9**, 449-454 (2007).

145. Burrell, A.K., Sesto, R.E.D., Baker, S.N., McCleskey, T.M. & Baker, G. a The large scale synthesis of pure imidazolium and pyrrolidinium ionic liquids - correction. *Green Chemistry* **9**, 449 (2007).

146. Nockemann, P. et al. Choline saccharinate and choline acesulfamate: ionic liquids with low toxicities. *The journal of physical chemistry. B* **111**, 5254-63 (2007).

147. Konig, A., Stepanski, M., Kuszlik, A., Keil, P. & Weller, C. Ultra-purification of ionic liquids by melt crystallization. *Chemical Engineering Research and Design* **86**, 775-780 (2008).

148. Holbrey, J.D., Rogers, R.D., Shukla, S.S. & Wilfred, C.D. Optimised microwave-assisted synthesis of methylcarbonate salts: a convenient methodology to prepare intermediates for ionic liquid libraries. *Green Chemistry* **12**, 407 (2010).

149. Zhang, J. et al. Voltammetric studies on the reduction of polyoxometalate anions in ionic liquids. *Inorganic chemistry* **44**, 5123-32 (2005).

150. Harris, D.C. *Quantitative Chemical Analysis*. *New York* (W. H. Freeman and Company: New York, 2007).

151. Harwood, L.M., Moody, C.J. & Percy, J.M. *Experimental Organic Chemistry: Standard and Microscale*. (Blackwell Science Ltd.: Malden, MA, 1989).

152. Hao, F., Haddad, P.R. & Ruther, T. IC Determination of Halide Impurities in Ionic Liquids. *Chromatographia* **67**, 495-498 (2008).

153. Stepnowski, P. & Mrozik, W. Analysis of selected ionic liquid cations by ion exchange chromatography and reversed-phase high performance liquid chromatography. *Journal of separation science* **28**, 149-54 (2005).

154. Villagrán, C., Banks, C.E., Hardacre, C. & Compton, R.G. Electroanalytical determination of trace chloride in room-temperature ionic liquids. *Analytical chemistry* **76**, 1998-2003 (2004).

155. Xiao, L. & Johnson, K.E. Electrochemistry of 1-Butyl-3-methyl-1H-imidazolium Tetrafluoroborate Ionic Liquid. *Journal of The Electrochemical Society* **150**, E307 (2003).

156. Gnahm, M. & Kolb, D.M. The purification of an ionic liquid. *Journal of Electroanalytical Chemistry* **651**, 250-252 (2011).

157. Mayrand-Provencher, L. & Rochefort, D. Origin and effect of impurities in protic ionic liquids based on 2-methylpyridine and trifluoroacetic acid for applications in electrochemistry. *Electrochimica Acta* **54**, 7422-7428 (2009).

158. *CRC Handbook of Chemistry and Physics - 75th Edition*. (1994).

159. *CRC Handbook of Chemistry and Physics - 91st Edition*. *Science* (2011).

160. Cammarata, L., Kazarian, S.G., Salter, P. a & Welton, T. Molecular states of water in room temperature ionic liquids. *Physical Chemistry Chemical Physics* **3**, 5192-5200 (2001).

161. Anderson, J.L., Ding, J., Welton, T. & Armstrong, D.W. Characterizing ionic liquids on the basis of multiple solvation interactions. *Journal of the American Chemical Society* **124**, 14247-54 (2002).

162. Belieres, J.-philippe & Angell, C.A. Protic Ionic Liquids : Preparation , Characterization , and Proton Free Energy Level. *Society* 4926-4937 (2007).

163. Robert, T., Magna, L., Olivier-Bourbigou, H. & Gilbert, B. A Comparison of the Acidity Levels in Room-Temperature Ionic Liquids. *Journal of The Electrochemical Society* **156**, F115 (2009).

164. Bautista-Martinez, J.A. et al. Hydrogen Redox in Protic Ionic Liquids and a Direct Measurement of Proton Thermodynamics. *J. Phys. Chem. C.* **113**, 12586-12593 (2009).

165. Paillard, E. et al. Electrochemical and Physicochemical Properties of PY[sub 14]FSI-Based Electrolytes with LiFSI. *Journal of The Electrochemical Society* **156**, A891 (2009).

166. Dominey, L. a, Koch, V.R. & Blakley, T.J. Thermally stable lithium salts for polymer electrolytes. *Electrochimica Acta* **37**, 1551-1554 (1992).

167. Gupta, V. & Miura, N. Polyaniline/single-wall carbon nanotube (PANI/SWCNT) composites for high performance supercapacitors. *Electrochimica Acta* **52**, 1721-1726 (2006).

APPENDIX A

NMR ANALYSIS OF $[C_4mpy][NTf_2]$ $[C_4dmim][OTf]$

The ^{13}C and ^{1}H NMR spectra for $[C_4mpy][NTf_2]$ and $[C_4dmim][OTf]$ batchs analyzed in Chapter 10 are shown below. The NMR was taken by Daniel Mahlman and analyzed by Derek Wolfe. All batches are indistinguishable, with the exception of $[C_4mpy][NTf_2]$ Batch (6) which yields a spurious peak at 2.3 in the ^{1}H NMR. Some finer points about the spectrum are as follows. All $[NTf_2]^-$ ILs have two carbon signals that overlay and are presented in the inset. The proton coupling in the C_4mpy ILs is weak, producing peak broadening and low resolution for the fine structure. The fluorine-carbon coupling is a quartet and is seen in all ILs.

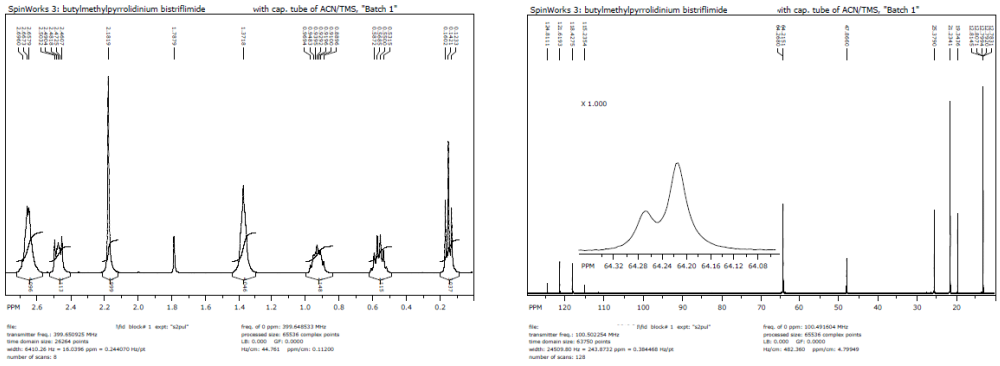

Figure A.1: $[C_4mpy][NTf_2]$ Batch (1) NMR spectra for left) ^{1}H and right) ^{13}C.

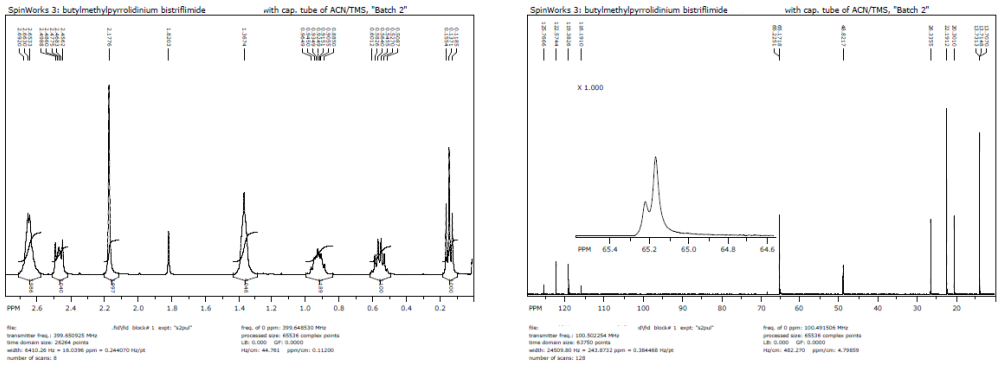

Figure A.2: $[C_4mpy][NTf_2]$ Batch (2) NMR spectra for left) ^{1}H and right) ^{13}C.

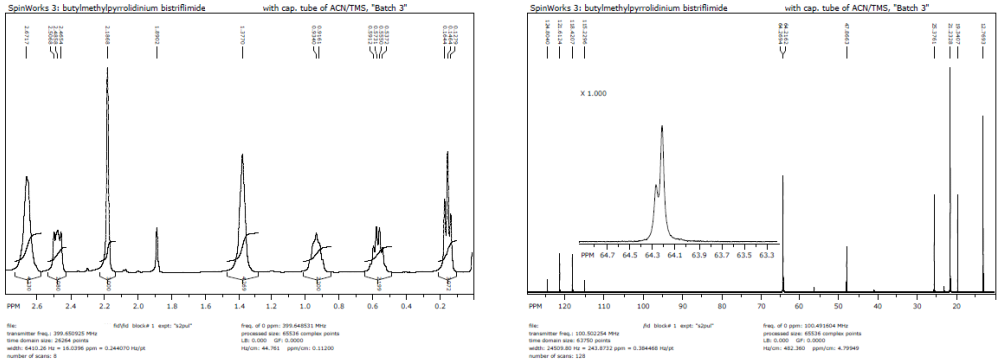

Figure A.3: $[C_4mpy][NTf_2]$ Batch (3) NMR spectra for left) ^{1}H and right) ^{13}C.

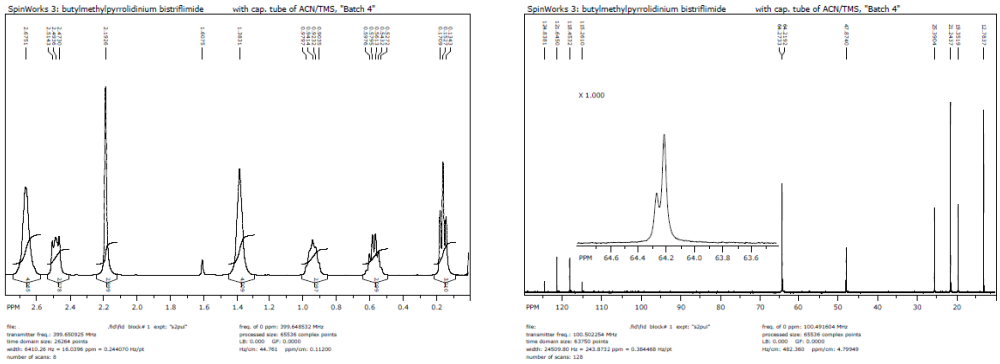

Figure A.4: $[C_4mpy][NTf_2]$ Batch (4) NMR spectra for left) ^{1}H and right) ^{13}C.

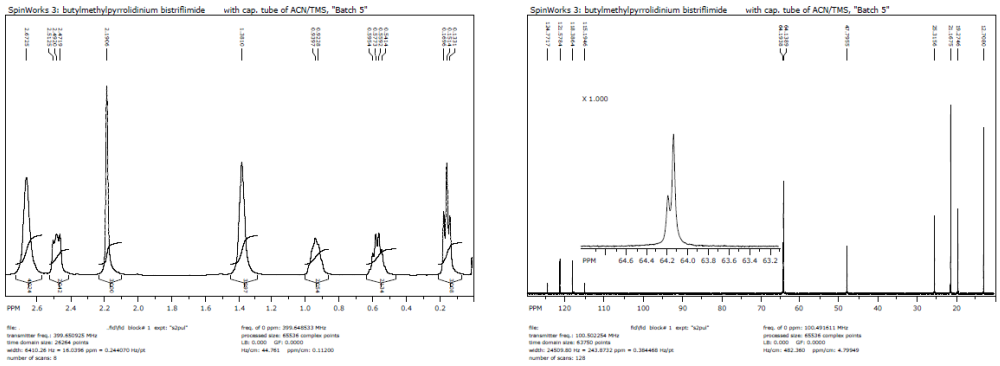

Figure A.5: [C_4mpy][NTf_2] Batch (5) NMR spectra for left) ^{1}H and right) ^{13}C.

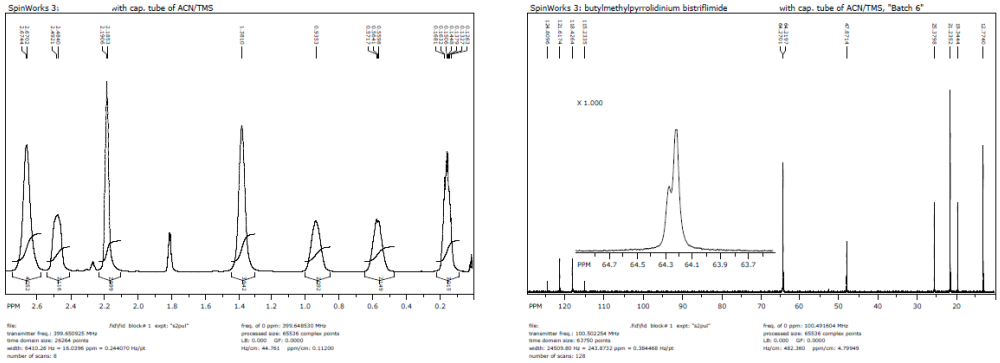

Figure A.6: [C_4mpy][NTf_2] Batch (6) NMR spectra for left) ^{1}H with an unidentified peak is present at 2.3, and right) ^{13}C.

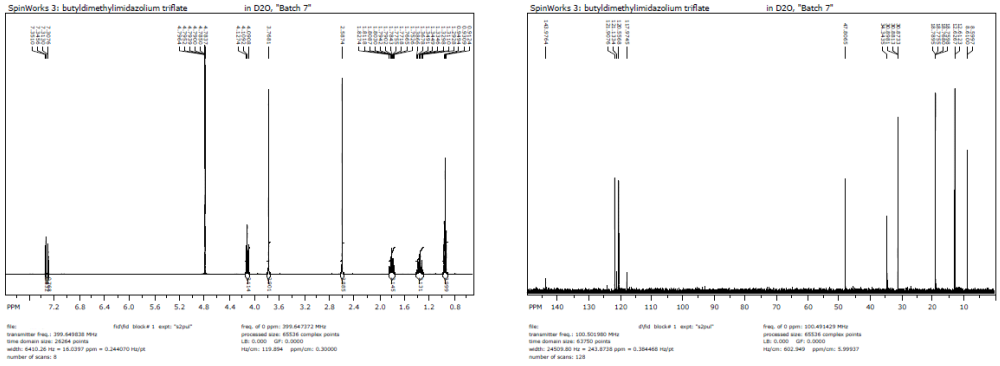

Figure A.7: [C_4dmim][OTf] Batch (7) NMR spectra for left) ^{1}H and right) ^{13}C.

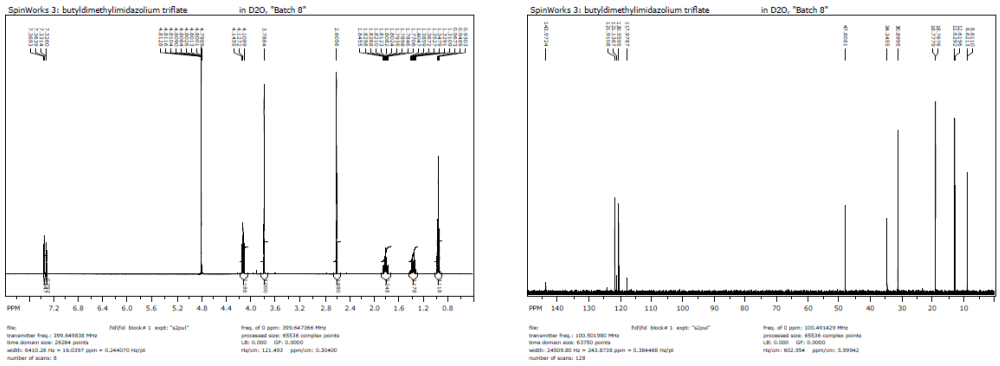

Figure A.8: [C_4dmim][OTf] Batch (8) NMR spectra for left) ^{1}H and right) ^{13}C.

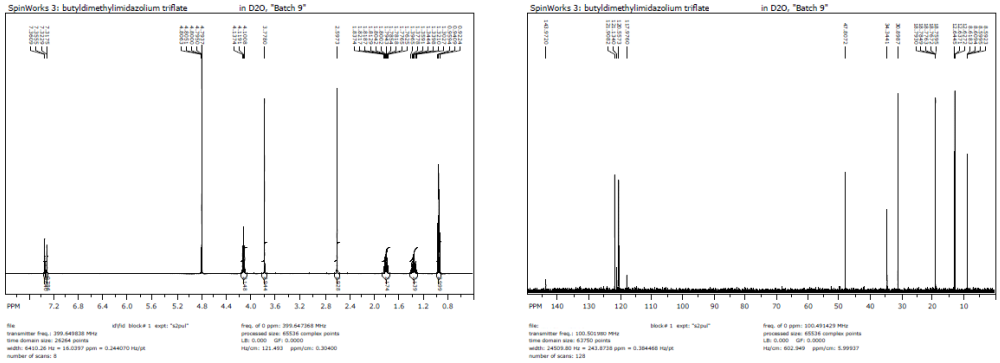

Figure A.9: [C_4dmim][OTf] Batch (9) NMR spectra for left) ^{1}H and right) ^{13}C.

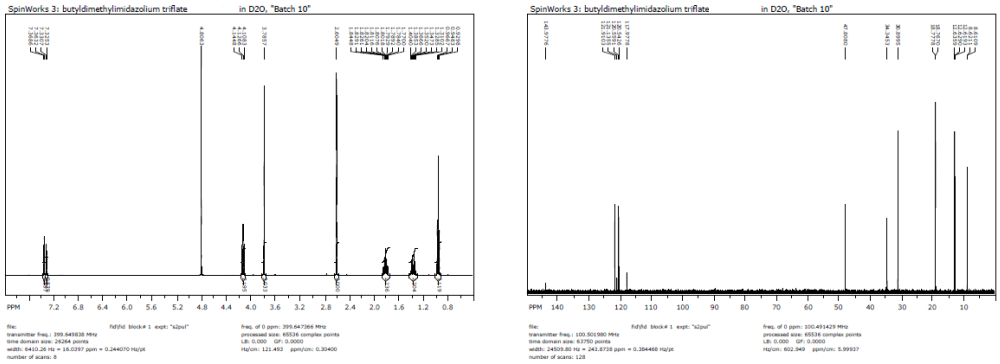

Figure A.10: [C_4dmim][OTf] Batch (10) NMR spectra for left) ^{1}H and right) ^{13}C.

APPENDIX B

OBSERVATIONS IN H-PD {111} SYSTEM VIA STRESS AND EQCM MEASUREMENTS

This following is a manuscript that was submitted to the Journal of the Electrochemical Society in August 2011. The study focused on the stress and mass response to the electrochemical absorption of hydrogen in palladium thin films. The work did not contribute to the narrative of the body of the thesis and is better suited for an appendix. I am the first co-author on this article and I have received verbal permission from the other co-authors, Thomas Heaton, Jordan Kennedy and Cody Friesen to include this in my dissertation.

Observations in the H-Pd{111} System via Stress and EQCM Measurements

E. L. Engstrom (Erika L. Engstrom), Th. Heaton (Thomas Heaton), J. K. Kennedy (Jordan K. Kennedy), C. Friesen* (Cody Friesen)

Arizona State University, School for Engineering of Matter, Transport and Energy
Engineering Center G-Wing
501 E. Tyler Mall
Tempe, AZ 85281

***cfriesen@asu.edu**

Abstract

The under-potential deposition (UPD) & absorption of hydrogen in thin film palladium (45-75nm) was investigated electrochemically utilizing both EQCM and thin film stress measurement techniques. The total frequency change during H absorption (desorption) as measured by EQCM is attributed to both an increase (decrease) in mass, Δf_m, as well as the associated thin film stress evolution, Δf_s. In order to deconvolute these two contributions, the changes in the Pd{111} thin-film stresses were measured directly by a high-resolution cantilever curvature-based stress monitoring technique. Mass incorporation and stress generation due to hydrogen absorption were recorded during cyclic voltammetric scans of increasingly cathodic potentials as well as during chronoamperometric holds in the hydrogen UPD region. The combination of stress measurements and mass uptake due to hydrogen provided a measure of the partial molar volume of hydrogen in the Pd thin films, $\overline{V}_{H-Pd}^{biax}$ =0.44 cm^3/mol. Additionally, the occurrence of hysteresis and dramatic changes in slope of stress vs. H concentration during

saturation loading of thin films is explained in the context of elastic-plastic transitions that occur in the film.

Introduction

The unique interaction between hydrogen and palladium has aroused great scientific curiosity since it was discovered in 1866 that large amounts of hydrogen could be absorbed by palladium[1]. The large solubility of H in Pd and the rapid diffusion of H through Pd have led to a significant amount of interest in Pd and Pd-based alloys as membranes[2,3] and hydrogen storage materials[4]. Furthermore, the rapid absorption of H in Pd generates a unique electrochemical response when Pd is used as an electrode during hydrolysis of water[5].

As with many metal/transition-metal systems, a process known as underpotential deposition (UPD) occurs in both the H/Pt and H/Pd systems [6,7]. In the case of a Pt electrode in an aqueous solution, the Pt surface catalyzes the reduction of H^+ as the potential is swept cathodically to ~300 mV vs RHE and a single monolayer (ML) of adsorbed H is formed[6,8]. In this particular system, continued reduction does not occur because the adsorbed monolayer screens the underlying Pt electronic structure. The UPD monolayer of H is stable until the potential is decreased below the reversible potential of H (0 V vs RHE) where bulk reduction occurs to form molecular hydrogen. In the case of the H/Pd UPD system, a unique process occurs due to the high solubility and diffusion rate of H in Pd metal. Because the kinetics of proton reduction in the UPD regime are slower

than the absorption kinetics of the previously adsorbed H, this process prevents the completion of a full UPD monolayer[9]. Thus, the reduction wave due to H-UPD is not limited to a single ML thickness as in the H/Pt system. In the results presented here, this two-step hydrogen incorporation process of underpotentially deposited hydrogen followed by its subsequent absorption into the Pd bulk will be referred to as underpotential absorption (UPA).

The H-Pd UPA process leads to the two effects studied in this work: an increase in electrode mass and the generation of compressive stress due to the diffusion of H into Pd octahedral interstices and defect sites[10,11]. Both of these effects contribute to the modification of the frequency signal that is measured using an electrochemical quartz crystal microbalance (EQCM). Unfortunately, there is no empirical method to separate the two contributions without an additional experimental measurement. Previously, several studies on Pd thin films (100 – 400 nm) were completed using the EQCM technique to track the changes in the frequency signal during absorption and desorption of H in Pd during electrochemical cycling [5,12-14]. In these EQCM studies, the mass changes were correlated to frequency changes measured directly from a quartz crystal resonator. However, since the measured frequency of quartz crystal resonators are affected by a variety of physical factors, EQCM frequency measurements on Pd thin films cannot be directly converted to mass changes. Some of these factors are changes in mass due to hydrogen ingress and egress, molecular and ionic adsorption, oxide formation, density and viscosity changes of the near surface solution, thin film

stress accumulation, as well as effects associated with the roughness of the electrode surface[15,16]. In the case of a Pd thin film immersed in dilute aqueous acid electrolyte, changes in frequency are limited to contributions from the mass increase (decrease) from atomic hydrogen insertion (extraction), Δf_m, and the associated thin film stress evolution, Δf_s. Thus the measured frequency signal of the EQCM is the sum of these two contributions

$$\Delta f_{total} = \Delta f_m + \Delta f_s, \quad (1)$$

both of which are nonlinear and dependent on the electrode potential. That is, any measurements of H uptake into Pd film electrodes must be adjusted properly to account for non-negligible film stress induced frequency shifts. To this end, one must consider the theoretical predictions of the frequency changes due to each individual contributing factor. First, the frequency shift due to the mass change is predicted by the well-known Sauerbrey equation and can be written as

$$\Delta f = \frac{-\Delta m \cdot f_0}{\rho_q \cdot t_q}, \quad (2)$$

where f_0 is the resonant frequency in Hz, Δm is the mass change in grams, ρ_q is the density of quartz (2648 kg/m^3), and t_q is the thickness of the crystal (0.0166 cm)[17]. Additionally, EerNisse introduced a relation providing the frequency shift due to stress accumulation in the film[18]. This stress-induced frequency shift is given by

$$\Delta f_s = k\Delta S \cdot \frac{f_0}{t_q}, \qquad (3)$$

where k is a constant (-2.75 x 10^{-11} m^2/N for the AT cut crystals used in this work), and ΔS is the surface stress in N/m. The surface stress relates to the average bulk stress, σ_f , by Equation (4),

$$\Delta S = \sigma_f \cdot t_f, \qquad (4)$$

where t_f is the film thickness [13]. The frequency shifts due to stress and mass changes cannot be deconvoluted without an additional independent measurement. Accordingly, many previous studies of hydrogen absorption systems have relied on electrochemical charge measurements to determine the amount of hydrogen absorbed into the metal films, thus allowing for an indirect measure of film stress after subtraction of Δf_m from the total measured frequency change, Δf_{total}. Another method, introduced by EerNisse and demonstrated by several other groups, utilizes a second EQCM measurement with a different quartz crystal cut (e.g. AT & BT) under the same conditions. The different frequency-stress responses of the different crystal resonator cuts allow for the extraction of the stress generated frequency change[14,18-20].

In this study, changes in the Pd{111} thin-film stresses were measured directly by a cantilever curvature technique. This high resolution, real time stress monitoring technique has been previously used in both ultra-high vacuum and electrochemical environments[21-28]. Previously, the palladium hydrogen system has been studied under a variety of conditions using the wafer curvature

techniques[19,29-31]. This stress measurement method monitors the stress induced sample curvature, which is then converted to a stress-thickness product through the Stoney Relation[32,33]

$$\Delta S = \Delta(\sigma_f \cdot t_f) = \frac{E_s t_s^2}{6(1-\nu_s)} \Delta\kappa, \qquad (5)$$

where σ_f and t_f are the stress and thickness of the film, E_s , t_s, and v_s are the elastic modulus, thickness, and Poisson's ratio of the substrate, and κ is the measured curvature. By dividing the surface stress, ΔS, by the film thickness one arrives at the average stress in a film.

For these investigations, the stress and EQCM experiments were performed separately under identical conditions and were subsequently correlated through the electrode potential from the voltammetric data. The top of Figure 1 is a representative cyclic voltammogram of UPA of hydrogen in the H-Pd{111} system. The corresponding gravimetric and stress responses are shown at the bottom of Figure 1.

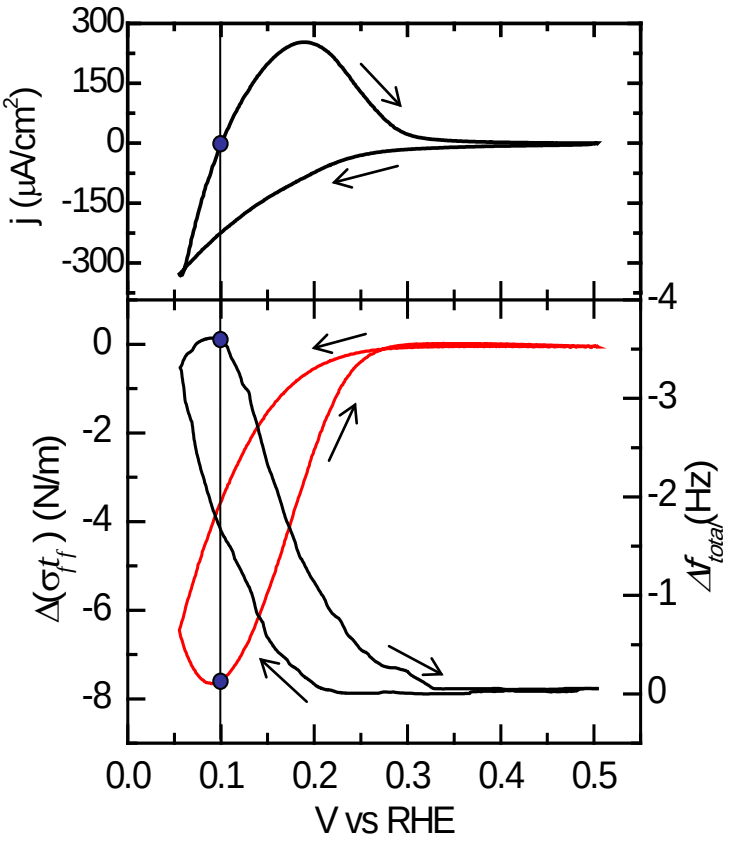

Figure 1: (top) Cyclic voltammetry in 0.1 M H_2SO_4 during UPA of H in a Pd{111} thin film. (bottom) Stress and gravimetric responses during cycling shown in red and black, respectively. The vertical dashed line marks the potential at which the anodic current sweep passes through zero and the blue circles denote the corresponding stress, frequency and current values at the zero current potential. Note that the frequency axis is reversed for clarity. Scan rate of 20 mV/s.

The adsorption and subsequent absorption of hydrogen into the film results in a large compressive stress that increases with increasing reduction charge. Furthermore, the cathodic sweep potential limit of +50 mV vs. RHE does not correspond to the maxima in either the stress or EQCM signals. Rather, both the frequency shift and stress signals continue to increase in magnitude during the anodic scan until the current reaches approximately zero, at ~+100 mV vs RHE. At potentials positive of ~+100mV vs. RHE, the adsorbed hydrogen begins to

oxidize and a chemical potential driving force is established for the diffusion of absorbed hydrogen to the surface, resulting in the egress of the absorbed H[34]. As can be seen in Figure 1, both the gravimetric and stress data exhibit significant hysteresis with respect to electrode potential. With further anodic scanning, the desorption of hydrogen returns the film to the initial stress state and frequency value.

By coupling mass and stress evolution during cyclic voltammetry of increasingly cathodic limiting potentials, we show that it is possible to appropriately account for stress-induced EQCM errors and thereby obtain agreement with accumulated hydrogen concentrations obtained from the corresponding electrochemical charge data. We also demonstrate that the combination of electrochemical and high-resolution stress measurements provides a method for the determination of the partial molar volume of H in Pd. Additionally, direct measurements of the saturation of H in Pd{111} thin films during potentiostatic holds during UPA are presented. An analysis of the mechanical response of the Pd during these saturation experiments yields insight into the origin of the stress as it relates to elastic-plastic transitions within the thin film.

Experimental

Stress Measurements

The *in situ* stress monitoring is carried out via a cantilever curvature based device described previously[35]. The device is unique in that the measurement is made

using a capacitive technique that provides sub-nanometer deflection sensitivity and >1 kHz time base resolution[21-23]. The stress measurement cell has a monolithic design that significantly reduces drift and sample placement error. The cell holds both the capacitance sensor and vertically oriented cantilevered electrode. The sample clamp has integrated gold contact pins for both the electrochemical and capacitance sensing electrodes. Additionally, because the sample holder, cell, and detector are in a single unit, calibration is easily performed by orienting the cell so that the cantilever is normal to +/- Earth's gravitational field. Calibrating the measurement in this way removes the elastic moduli of the cantilever and a squared term in cantilever thickness from the relation between curvature and film stress, both of which are significant sources of error in wafer curvature measurements. As noted earlier, the stress measurements are often reported as a stress-thickness in units of N/m. The choice of unit convention, however, depends on considerations related to the analysis and physical process occurring at the electrode. For the discussion of molar volume and the elastic-plastic response detailed below, it is convenient to consider the average stress in the film during hydrogen absorption in units of MPa. For all other cases, the results are given in stress-thickness units.

Electrochemistry

The electrochemical cell, Pt counter electrode, and all glassware utilized in the experiment were cleaned in heated, concentrated baths of HNO_3 and H_2SO_4 followed by rinsing in 18 MΩ-cm water. In addition, the Pt counter electrode was

hydrogen flame annealed and rinsed again in the 18 MΩ-cm water immediately before being placed in the electrochemical cell. For all experiments, a saturated calomel electrode (SCE) reference electrode (Princeton Applied Research – Model # K0077) was used. The working, reference and counter electrodes were placed in the cell prior to the loading of the electrolyte. For each experiment, the electrolyte was deaerated with high purity nitrogen gas and an overpressure was maintained during the experiments. In all cases either a BASi Epsilon Potentiostat (model # E2-020000) or Princeton Applied Research 263A Potentiostat were used. Gravimetric monitoring was performed with a Maxtek Inc. research quartz crystal microbalance and CHK-100 Kynar crystal holder (sensitivity of 0.4 ng/cm^2). For all experiments, the system consisted of a Pd thin film with a strong {111} texture immersed in deaerated 0.1 M H_2SO_4.

Sample Preparation

The cantilever samples used during stress monitoring experiments consisted of a 160 μm thick, cleaned borosilicate glass substrate and patterned Pd{111} films. The EQCM samples were comprised of a 5MHz, 1 inch, AT cut quartz crystal substrate with an as-received Cr/Au patterned film contact, on which a patterned Pd{111} film was deposited. The Pd film for both stress and EQCM samples were grown simultaneously under identical vacuum deposition conditions. DC magnetron sputtering was used to deposit a 1 nm Cr adhesion layer followed by 75 nm or 45 nm of Pd for the cyclic voltammetry and saturation experiments, respectively. A custom hard-mask was used to pattern all metal films and the

surface areas of the stress monitor and EQCM working electrodes were 2.00 and 1.27 cm^2, respectively.

Results

Experiments in both the stress monitor cell and the EQCM cell were performed under identical conditions. Figure 2a shows the representative cyclic voltammograms of the H-Pd{111} UPA process for cycles of increasingly cathodic potential limits.

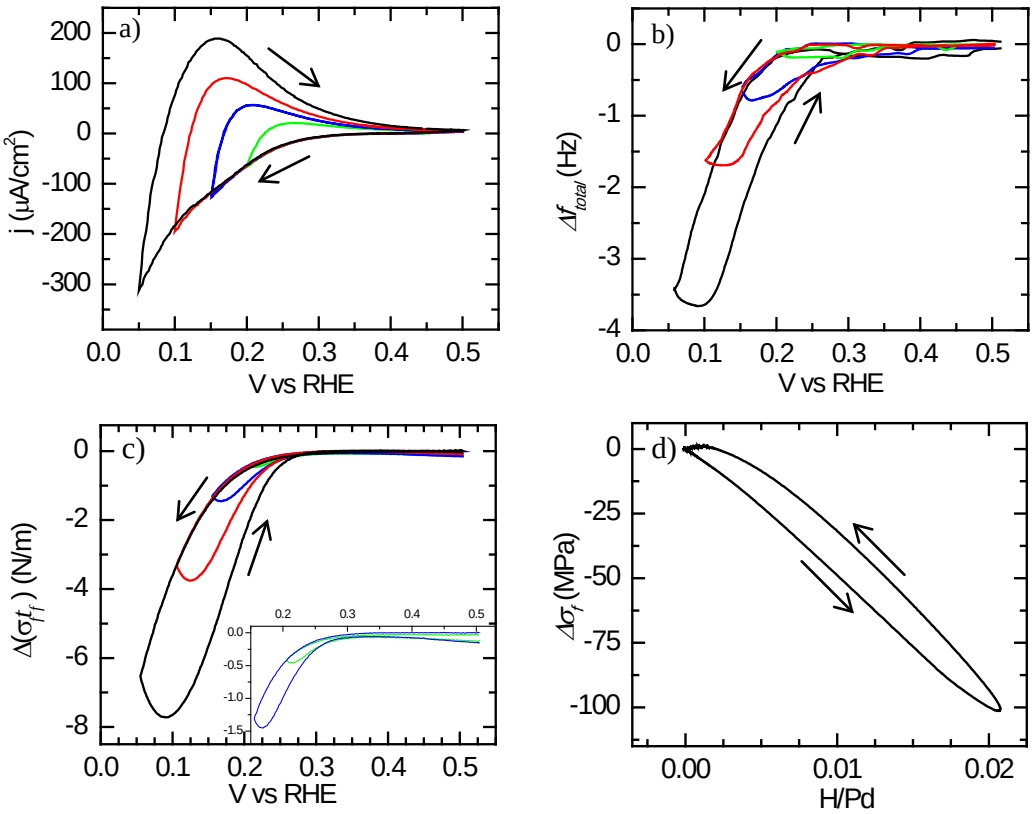

Figure 2: (a) Voltammetry of H-Pd{111} UPA at 20mV/s scan rate. Corresponding results of (b) Δf_{total} from EQCM and (c) Stress-thickness responses to UPA with the colors corresponding to cathodic limit (green: 0.2V, blue: 0.15V, red: 0.1V, and black: 0.05V vs. RHE.) Additionally, (d) the average bulk stress vs. concentration (H/Pd) is shown for the 0.05V cathodic limit cycle.

Figure 2b displays the total frequency response, Δf_{total}, to UPA loading where a negative frequency corresponds to an increase in mass according to Equation (1). Figure 2c is a plot of the stress-thickness response to UPA. As in Fig. 1 it is observed that the maximum stress and minimum frequency in all cases occur during the returning anodic scan when the net current passes through zero. The maximum observed stress-thickness change corresponds to a strain of 0.035%. Figure 2d shows a single stress-thickness curve converted to bulk stress as a function of the concentration of absorbed hydrogen in hydrogen to metal ratio (H/Pd). Note that while there is some hysteresis, both the cathodic and anodic scans have approximately constant and equivalent slopes, allowing for the extraction of the molar volume through a constitutive relation.

Figure 3a is a plot of frequency versus potential from the measured EQCM frequency signal, Δf_{total}, and frequency calculated from the stress signal (Eq. 3), Δf_s.

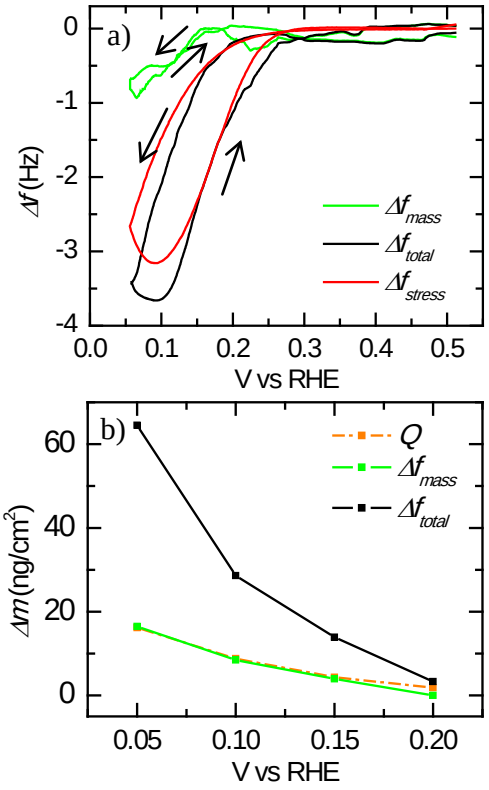

Figure 3: a) Frequency vs. potential for the total frequency, Δf_{total}, from the EQCM (black) the frequency calculated from the stress-thickness, Δf_{stress}, (red) and the mass frequency, Δf_m, calculated from Equation (1) (green). b) Mass calculated from Δf_{total} (black) and Δf_m (green) using the Sauerbrey Equation (Equation (2)) and mass calculated from electrochemical charge, Q (orange).

The EQCM measures changes in frequency that can be contributed to the mass uptake of H in Pd. However, calculating the mass from Δf_{total} alone using Equation (2), yields mass values 3-4 times higher than what is expected by calculating the mass from the electrochemical charge (Figure 3b). By converting the measured stress-thickness values to an expected frequency shift using Equation (3), it is evident that the stress contributes significantly to the total measured frequency change, Δf_{total}. As shown in Figure 3b, correction of the EQCM signal with simultaneous stress measurements via this subtraction method

yields mass values that correspond very well with electrochemical charge calculations.

Experiments to examine the saturation of hydrogen in the UPA regime were performed by holding chronoamperometrically at +20 mV vs RHE. Figure 4a is a plot of both the stress-thickness response and the hydrogen-palladium ratio (H/Pd) as calculated from the electrochemical charge as a function of time.

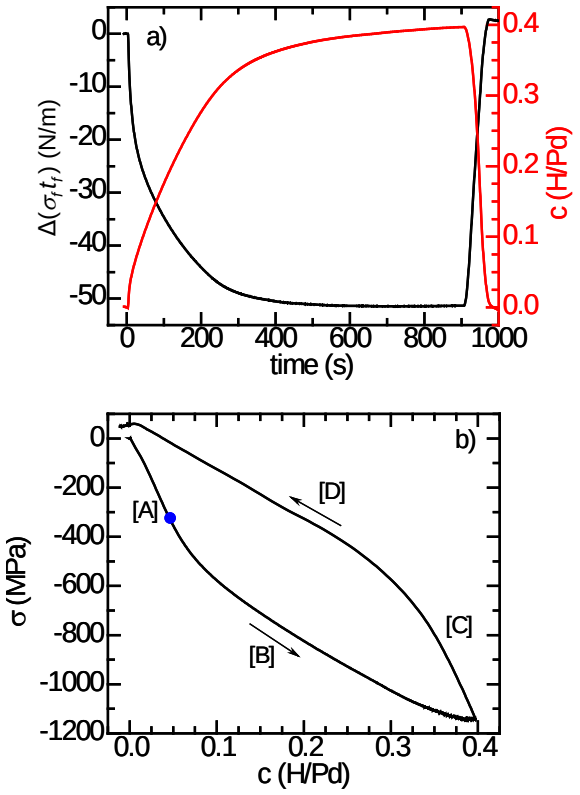

Figure 4: (a) Time evolution of stress-thickness (black) and absorbed H concentration (red) as calculated from the charge in the UPA regime. First, the Pd film was held at +0.5 V vs RHE, followed by a potential step to +0.02 V for 900 s, then the potential was scanned back to +0.5 V at 5mV/s. (b) Stress-thickness converted to bulk stress versus H/Pd from (a) where the blue circle corresponds to the value of σ_c calculated from Eq. (9). The initial regions of loading and unloading [A] and [C] have slopes of -7.8 GPa. After significant loading of H, the slope changes to approximately -2 GPa in regions [B] and [D].

Note that after approximately 400 seconds of loading, both the concentration and stress signals approach constant values. Figure 4b shows the stress-thickness signal converted to bulk stress as a function of H/Pd concentration from Figure 4a. The bulk stress response shows clear hysteretic behavior in the Pd film with respect to loading and unloading of H. Upon initial loading of H in Region A, there is large compressive stress slope of ca. -7.5 GPa until the concentration of H reaches approximately 0.05 H/Pd. At this concentration, there is a transition in slope to a smaller value of -2GPa, which remains constant for the remainder of saturation loading (Region B). Upon saturation of H in the Pd film, the concentration is approximately 0.4 H/Pd. Unloading of H occurs in Region C and Region D, which have slopes that are numerically equivalent and correspond to Regions A and B, respectively.

Discussion

The results represented in Figure 1 and Figure 3 demonstrate the advantage of using coupled electrochemical thin film stress and EQCM measurements. Whereas most of the previous studies have published apparent molar mass or average film stress measurements that have been inferred from electrochemical charge and EQCM experiments, we show that stress-corrected mass measurements agree well with mass increase associated with electrochemical charge [5,12-14]. The agreement of these two measurements confirms the validity of Equation (1) by adequately accounting for the total change in frequency as measured by the EQCM. Similarly, Stafford and Bertocci applied a similar stress-

corrected analysis to potentiodynamic scans of Pd overlayers on Au{111} films using surface stress measurement and both AT- and BT-cut quartz crystal resonators[19]. They found that for even ultrathin Pd films, the EerNisse treatment was in good agreement with the electrochemical charge. An additional advantage associated with real time film stress measurements is the further insight that is provided with respect to the potential dependent responses of the thin films to a variety of physical processes and experimental details, including the partial molar volume of hydrogen and elastic-plastic film stress behavior.

Partial Molar Volume of Hydrogen

The molar volume of an absorbate is an important thermodynamic parameter as it describes the volumetric excess associated with the uptake of the species into the absorbant. Figure 2d shows the bulk stress response as a function of H concentration due to loading in the UPA regime. The change in instantaneous elastic equibiaxial stress during loading is ca. -49 MPa at a change in concentration of approximately c = 0.01 H/Pd. The corresponding strain is calculated using the appropriate equibiaxial modulus for the textured Pd{111} film ($M_{111}^{Pd} = 287.7\,\mathrm{GPa}$) and is $\varepsilon_{x,y}^{\{111\}} = 1.7\times10^{-4}$. The dilatation as a function of concentration normally provides the partial molar volume of the interstitial species, however, in the case of a thin film deformed in the elastic regime on a thick substrate, the film is nominally 'clamped' in the plane. In this sense, $\varepsilon_{x,y}^{\{111\}}$ is comparable to an epitaxial strain and is only observed through the

associated stress. The Pd{111} film is not constrained in the out-of-plane direction and with the boundary condition of $\sigma_z^{\{111\}} = 0$, the strain in the out-of-plane direction can be calculated as

$$\varepsilon_z^{\{111\}} = -\frac{2\left(c_{11} + 2c_{12} - 2c_{44}\right)}{c_{11} + 2c_{12} + 4c_{44}} \varepsilon_{x,y}^{\{111\}}, \quad (6)$$

where c_{ij} are the components of the elastic stiffness tensor of Pd[33]. The ratio of strain in the z to the strain in the x,y directions for Pd is calculated to be $\varepsilon_z^{\{111\}} / \varepsilon_{x,y}^{\{111\}} = 1.006$. The zero-stress dilatation is then $\Delta = 0.00051$. Thus, the effective partial molar volume of H in Pd for this case of a biaxially constrained thin film is

$$\overline{V}_{H-Pd}^{biax} = \overline{V}_{Pd} \frac{\Delta}{c} = 0.44 cm^3 / mol, \quad (7)$$

where $\overline{V}_{Pd}$ is the molar volume of Pd (8.56 cm^3/mol) and c is the atomic concentration (c=0.01 H/Pd) of hydrogen in palladium[33]. The partial molar volume, $\overline{V}_{H-Pd}$, of the unconstrained H-Pd system has been reported in the literature to be 1.7 cm^3/mol, although at greater concentrations of H, e.g. in the β-phase region, a value of 0.4 cm^3/mol was reported [4]. The difference between the number calculated from our data, $\overline{V}_{H-Pd}^{biax}$ = 0.44 cm^3/mol, and the value reported in literature, $\overline{V}_{H-Pd}$ =1.7 cm^3/mol, is related to biaxial clamping of the film to the

substrate. In the case of a constrained film with ideal biaxial clamping, the expected molar volume can be calculated as [33]

$$\overline{V}_{H-Pd}^{biax,theor} = \overline{V}_{Pd}^{2/3}\left(\overline{V}_{Pd} + \overline{V}_{H-Pd}\right)^{1/3}\left(\varepsilon_z^{\{111\}} \Big/ \varepsilon_{x,y}^{\{111\}}\right) - \overline{V}_{Pd} = 0.59 cm^3/mol . \quad (8)$$

Using the literature value for partial molar volume of the unconstrained H-Pd system ($\overline{V}_{H-Pd}$ = 1.7 cm^3/mol) and calculating the strain ratio $\varepsilon_z^{\{111\}} / \varepsilon_{x,y}^{\{111\}}$ from Equation (6) using the known elastic constants, c_{ij}, the theoretical value of the biaxially constrained partial molar volume of H in Pd is $\overline{V}_{H-Pd}^{biax,theor}$ = 0.59 cm^3/mol. The difference between the measured value and this predicted value is due to the nanocrystalline nature of the Pd{111} thin film samples (D_{grain}~45nm). Upon absorption, H can occupy both grain boundaries or the interior region of the grain[36-39]. H stored at grain boundaries exists as atomic hydrogen and induces less deformation than hydrogen in the interior region[36]. Using the measured value of 0.44 cm^3/mol and an average grain size of 45nm, approximately 40% of the absorbed hydrogen is likely stored at the grain boundaries. This is similar to the findings of Weissmuller et. al. for hydrogen stored at the grain boundaries of nanocrystalline Pd of grain size ~10 nm[39].

Hysteresis During Saturation Loading/Unloading

Hysteresis of the type shown in Figure 4b is similar to the stress responses that have been observed during temperature cycling of thin metal films [40-42]. For example, Nix demonstrated this type of behavior for Al and Cu films on Si

substrates. In these investigations, the biaxial film stress is plotted as a function of temperature (σ-T), where thermal expansion mismatch between film and substrate causes a change in thin film stress state. Similarly, the stress associated with H loading and unloading of Pd is also dependant on the dimensional constraints imposed by the substrate as well as the volumetric change associated with H-uptake. In the case of the thermally induced strains, there is a point as the temperature is increased beyond a critical value where the slope of σ-T decreases with increasing temperature, indicating a decrease in the rate of compressive stress generation. This behavior is similar to that observed in transition from Region A to Region B in Figure 4b where the stress-concentration slope changes from -7.8GPa to -2 GPa. Similarly, the unloading of H in Regions C and D results in stress-concentration slopes that are identical to those in Regions A and B, respectively. In the case of films constrained only by the substrate, the dislocations are stored near the interface and at a large enough strain, the onset of plastic flow occurs. The onset is indicated by the point at which the slope changes in the σ-T hysteresis and defines the critical yield stress for the dislocation motion. This is given by

$$\sigma_c = \frac{\sqrt{3}\cdot\mu b}{8\pi\cdot(1-\nu)\cdot t_f}\left[(4-\nu)\log\left(\frac{2h}{b}\right)-\left(\frac{3}{2}\right)\right], \qquad (9)$$

where μ is the elastic modulus, ν is the Poisson's ratio, t_f is the film thickness and b is the Bergers vector[40]. From the data presented in Figure 4b, the value of σ_c was calculated using t_f = 45 nm and assuming the <011>{111} slip system. For the case of H absorption induced stress accumulation, σ_c was found to be

approximately -320 MPa and corresponds to a concentration of c = 0.045 H/Pd (denoted by a blue circle in Figure 4b). As shown in the figure, this stress value coincides with the transition in the slope between Region A and B which occurs at ca. -350 MPa and c = 0.05 H/Pd. Furthermore, this behavior occurs at concentrations of hydrogen that approach the transition from a purely α-phase Pd-H to a mixture of both α- and β-phases of Pd-H. Recently, Shin et al. made similar arguments related to the plastic behavior of a 1 nm thick Pd film, based on observations in the stress response of the film to H saturation[31].

Conclusion

Stress measurements and electrochemical quartz crystal microbalance measurements were performed to study the response in the under-potential deposition and absorption of hydrogen on thin films of Pd {111} (t_f = 45 & 75nm). The total frequency changes during H absorption and desorption are attributed to changes in mass, Δf_m, as well as thin film stress evolution, Δf_s. The value Δf_s was determined directly from a high resolution, real-time cantilever curvature stress monitoring technique in order to correct the total frequency signal measured by EQCM. It was found that this method agrees well with hydrogen uptake as determined from electrochemical charge measurements. Utilizing the hydrogen mass and film stress measurements, a direct measure of the molar volume of hydrogen in Pd, $\overline{V}_{H-Pd}^{biax}$ =0.44 cm^3/mol, was obtained. Finally, the existence of hysteresis and dramatic slope changes in the film stress measurements during saturation of hydrogen in Pd films was correlated to elastic-

plastic transitions in thin films as observed previously during thermal cycling experiments.

References:

1. Graham, T., *Philos. Tras. Royal Soc. London*, **136**, (1866).

2. Zhang, W.-S., Zhang, X.-W. and Zhao, X.-G., *J Electroanal. Chem.*, **458**, 107-112 (1998).

3. Paglieri, S.N. and Way, J.D., *Sep & Purif. Rev.*, **31**, 1-169 (2002).

4. Feenstra, R., Groot, D.G. de and Griessen, R., *J. Phys. F: Met. Phys.*, **16**, 1933-1952 (1986).

5. Yamamoto, N., Ohsaka, T., Terashima, T., and Oyama, N., *J. Electroanal. Chem. and Interfacial Electrochem.*, **296**, 463-471 (1990).

6. Clavilier, J., Faure, R., and Guinet, G., *J. Electroanal. Chem.*, **107**, 205-209 (1980).

7. Jaksic, M., Johansen, B., and Tunold, R. *Int. J. Hydrogen Energy*, **18**, 111-124 (1993).

8. Markovic, N., Lucas, C. A., Rodes, A., Stamenkovic, V., and Ross, P. N., *Surf. Sci.*, **499**, L149-L158, (2002).

9. Baldauf, M., and Kolb, D.M., *Electrochim. Acta*, **38**, 2145-2153 (1993).

10. Gabrielli, C., Grand, P. P., Lasia, A., and Perrot, H., *J. Electrochem. Soc.*, **151**, A1937 (2004).

11. Baranowski, B., Majchrzak, S., and Flanagan, T.B., *J. Phys. F: Met. Phys.*, **1**, 258-261 (1971).

12. Łukaszewski, M., and Czerwiński, A. *J. Electroanal. Chem.*, **589**, 87-95 (2006).

13. Liu, S., Kao, Y.-H., Oliver Su, Y., Perng, T.-P., *J. Alloys and Compd.*, **293-295**, 468-471 (1999).

14. Cheek, G.T. and O'Grady, W.E. *J. Electroanal. Chem. and Interfacial Electrochem.*, **277**, 341-346 (1990).

15. Lukaszewski, M. and Czerwiński, A., *Polish J. Chem.* **81**, 847-864 (2007).

16. Kanazawa, K. and Gordon, J. *Anal. Chimica Acta* **175**, 99-105 (1985).

17. Sauerbrey, G. *Zeitschrift für Physik. A, Hadrons and nuclei*, **155**, 206 (1959).

18. EerNisse, E.P., *J. Appl. Phys.*, **43**, 1330 (1972).

19. Stafford, G.R. and Bertocci, U. *J. Phys. Chem.*, 13249-13256 (2009).

20. Cheek, G.T. and Grady, W.E.O. *Cell*, **368**, 133-138 (1994).

21. Friesen, C. and Thompson, C.V.,*Phys. Rev. Lett.*, **89**, 1-4 (2002).

22. Friesen, C. and Thompson, C., *Phys. Rev. Lett.*, **93**, 1-4 (2004).

23. Friesen, C., Seel, S.C. and Thompson, C.V., *J. Appl. Phys.*, **95**, 1011 (2004).

24. Chason, E., Sheldon, B., Freund, L., Floro, J., and Hearne, S., *Phys. Rev. Lett.*, **88**, 1-4 (2002).

25. Chason, E. and Sheldon, B.W., *Surf. Eng.* **19**, 387-391 (2003).

26. Heaton, T. and Friesen, C., *J. Phys. Chem. C*, **111**, 14433-14439 (2007).

27. Mickelson, L., Heaton, T. and Friesen, C., *J. Phys. Chem. C*, **112**, 1060-1063 (2008).

28. Mickelson, L.L. and Friesen, C. *J. Am. Chem. Soc.*, **131**, 14879-84 (2009).

29. Han, J.-N., Lee, J.-W., Seo, M., and Pyun, S.-I., *J. Electroanal. Chem.*, **506**, 1-10 (2001).

30. Sahu, S., Scarminio, J., and Decker, F. A., *J. Electrochem. Soc.*, **137**, 1150 (1990).

31. Shin, J.W., Bertocci, U., and Stafford, G.R., *J. Electrochem. Soc.*, **158**, F127 (2011).

32. Stoney, G.G., *The Royal Society*, **82**, 172-175 (1909).

33. Freund, L. and Suresh, S. *Thin Film Materials: Stress, Defect Formation and Surface Evolution*, Cambridge University Press, Cambridge, 2003.

34. Lewis, F. A., Tong, X. Q., Kandasamy, K., Bucur, R. V., and Sakamoto, Y., *Thermochim. Acta*, **218**, 57-69 (1993).

35. Heaton, T. and Friesen, C., *J. Phys. Chem. C*, **111**, 14433-14439 (2007).

36. Kirchheim, R. and Mutschele, T., *Scr. Metall.*, **21**, 135-140 (1987).

37. Pundt, A. and Kirchheim, R., *Annu. Rev. Mater. Res.*, **36**, 555-608 (2006).

38. Bartlett, P.N. and Marwan, J., *Phys. Chem. Chem. Phys.*, **6**, 2895 (2004).

39. Lemier, C. and Weissmüller, J., *Acta Mater.* **55**, 1241-1254 (2007).

40. Nix, W. *Scr. Metall.*, **39**, 545-554 (1998).

41. Kobrinsky, M.J. and Thompson, C.V., *Appl. Phys. Lett.*, **73**, 2429 (1998).

42. Baker, S., *Mater. Sci. Eng. A*, **319-321**, 16-23 (2001).